Unione Europea

PON Ricerca e Innovazione 2014- 2020

Ministero dell'Istruzione, dell'Università e della Ricerca

UNIVERSITA' DEGLI STUDI DI NAPOLI

"FEDERICO II"

SCUOLA POLITECNICA E DELLE SCIENZE DI BASE

PhD Thesis in Industrial Products and Process Engineering

XXX CYCLE

Smart design and *in vitro* testing of nanoparticles for microenvironmentally-triggered extracellular drug release

Supervisor

Prof. Dr. P. A. Netti

Coordinator

Prof. Dr. G. Mensitieri

Ph.D. Student

Martina Profeta

2014 - 2017

SMART DESIGN AND *IN VITRO* TESTING OF NANOPARTICLES FOR MICROENVIRONMENTALLY - TRIGGERED EXTRACELLULAR DRUG RELEASE

A THESIS SUBMITTED IN PARTIAL FULFILMENT OF THE REQUIREMENTS FOR THE DEGREE OF DOCTOR OF PHILOSOPHY IN

INDUSTRIAL PRODUCTS AND PROCESS ENGINEERING

AUTHOR

Martina Profeta

SUPERVISOR

Prof. Dr. Paolo A. Netti

COORDINATOR

Prof. Dr. Giuseppe Mensitieri

If science teaches us anything,

it teaches us to accept our failures,

as well as our successes,

with quiet dignity and grace.

Frankenstein Junior.

Table of Contents

Aim of the Work

In the field of nanotechnology, one of the most operative research areas is nanomedicine, which applies nanotechnology to highly specific medical interventions for the prevention, diagnosis and treatment of diseases. Currently, the major issue that nanomedicine needs to face is the smart design and production of nanoparticles (NPs) based drug delivery systems for cancer therapy.

Highly efficient drug delivery based on nanoparticles could potentially reduce the drug dose needed to achieve therapeutic benefit, thus reducing the side effects associated with the systemic delivery of drugs, whit great benefit to the patient. Indeed, a site-specific delivery of the active compound can be obtained manipulating NP surface by attaching ligands, such as peptides, antibodies or aptamers. Moreover, both passive and active targeting of the drug can be easily obtained by manipulating NP size and surface characteristics. NPs can also control and sustain the release of a drug during transport to, or at, the site of localization, altering drug distribution and subsequent clearance.

At present, a new family of nanovectors, defined as *stimuli-responsive* nanocarriers (SRNs), is emerging. The key point in their mechanism of action lay in the fact that a specific cellular or extracellular endogenous *stimulus* of chemical, biochemical, or physical origin can modify NP conformation thus promoting the release of the active agent in a specific biological environment [1] [2]. In particular, a large variety of enzymes, such as proteases, glucuronidase, or carboxylesterases can be used as biochemical triggers. Generally the proteases, that are extracellularly expressed, such as the matrix metalloproteases (MMPs), are up-regulated in tumour microenvironment and are responsible for the proteolysis of the extracellular matrix (ECM) and of the basement membranes along with tissue remodelling and metastasis invasion. Since that, they are commonly identified as biomarkers of malignant tissues [3].

In the light of these considerations, **Chapter.1** points out a smart approach in NPs design that takes benefits from the MMPs over-expression at tumour site, in order to produce a *stimuli-responsive* nanocarrier that allows a site specific drug release.

To this aim, we proposed the use of a novel nanoparticle able to carry safely doxorubicin (Dox) at tumour tissues, and to respond to MMP-2 enzyme. The produced NPs are made up of a biodegradable poly(D,L-lactic-co-glycolic acid) (PLGA) – block – PEG copolymer (namely PELGA), blended with a TAP (Tumour Activated Pro-drug)

composed by a MMP-2-sensitive peptide bound to Dox at the C-terminus and to PLGA molecule at the N-terminus. These NPs are named PELGA-TAP NPs. The presence of the MMP-2 enzyme *in situ*, leads to the destruction of the bond between the peptide and the Dox, with the consequent diffusion and accumulation of the drug in the extracellular environment. This mechanism allows the drug delivery only in presence of an endogenous *stimulus* that comes from the very nature of the tumour tissue itself. Furthermore, the same NPs were prepared without the presence of the peptide sequence, as negative control, and were named PELGA-Dox. Spheroids of U87 (Human Glioma cells) and HDF (Human Dermal Fibroblast) cells were used as *in vitro* models of tumour and healthy tissue, respectively, to demonstrate NPs ability to "sense" the differences in the expression levels of endogenous MMP-2 enzymes [4].

Since the production process and effectiveness of PELGA-TAP and PELGA-Dox NPs was well established and consolidate, in **Chapter.2** we tested them in a new three-dimensional microtissue (3D µTP) model, which is an *in vitro* tissue equivalent proposed by *Brancato et al.* [5]. They fabricate µTPs with the aim to replicate *in vitro* the composition and the functionalities of the tumour microenvironment. In this work they clearly show that µTPs better recapitulate the important differences existing *in vivo* between normal and cancer-activated stroma representing a more suitable system to mimic *in vitro* the tumour microenvironment. In particular, the 3D model was developed using normal fibroblasts (NF) and human epithelial cell lines (MCF10), or cancer-activated fibroblasts (CAF) and human breast adenocarcinoma cells (MCF7), to produce healthy and cancer microtissues, respectively. In this scenario, PELGA-TAP and PELGA-Dox NPs were tested in terms of Dox release on these µTPs in order to further validate their efficacy and selective drug release in a more realistic *in vitro* model, which better resemble tumour microenvironment, closer to the *in vivo* conditions [6].

Moreover, **Chapter.3** shows an upgrade of the PELGA-TAP NP presented above. The approach used for the production of the nanocarrier takes advantages from the layer by layer polymer deposition technique developed and optimized by *Vecchione et al.* [7]. This technique allows the production of a very stable nanocarrier able to load large amounts of hydrophobic drugs and prevents their systemic leakage. The delivery system we proposed is a crosslinked polyelectrolytes nanocapsule (NC) based on an oil-core and a matrix metalloproteases-2-sensitive shell. MMP-2 enzymes catalyse the disassembly of the NC, which is stabilized by a MMP-2-cleavable peptide sequence as cross-linker. Also in this

case, the drug release occurs in a spatially-controlled fashion upon an endogenous *stimulus* coming from the very nature of the tumour itself. The same NC was also produced with a scrambled peptide sequence as negative control. These NCs were tested on a spheroidal *in vitro* model, in order to proof their selective shell destabilization and consequent *stimuli-responsive* drug release in tumour microenvironment. Spheroids of U87 and HDF were used as models of tumour and healthy tissue, respectively. Cell viability was evaluated by means of Alamar Blue Assay. Moreover, the selective disassembly of the NC shell was followed using confocal microscopy and colocalization analyses were also performed.

Finally, in **Chapter.4** preliminary studies aimed to point out the advantages of an extracellular drug delivery are presented.

State of the Art

Cancer: Development and Metastasis Formation

The human body is made up of many types of cells which grow and divide in a controlled fashion. When cells become old or damaged, they are replaced with new ones. Unfortunately, sometimes this orderly process may go wrong and the genetic material (DNA) of a cell can become damaged or changed, producing mutations that affect cell growth and division. When this happens, cells do not die when they should and new cells duplicate in an uncontrolled way. The extra cells may form a mass of tissue called "tumour".

Tumours can be benign or malignant (State of the Art, Figure1.1). Benign tumours are localized and surrounded by a membrane, namely capsule, that separates them from the surrounding tissues. They can often be removed by surgery and, most importantly, do not spread to other parts of the body; since that, benign tumours are defined as non-cancerous. On the other hand, malignant tumours are cancerous. Indeed, in this case cells can invade nearby tissues spreading into other parts of the body. The spreading of cancer cells from one part of the body to another is called metastasis.

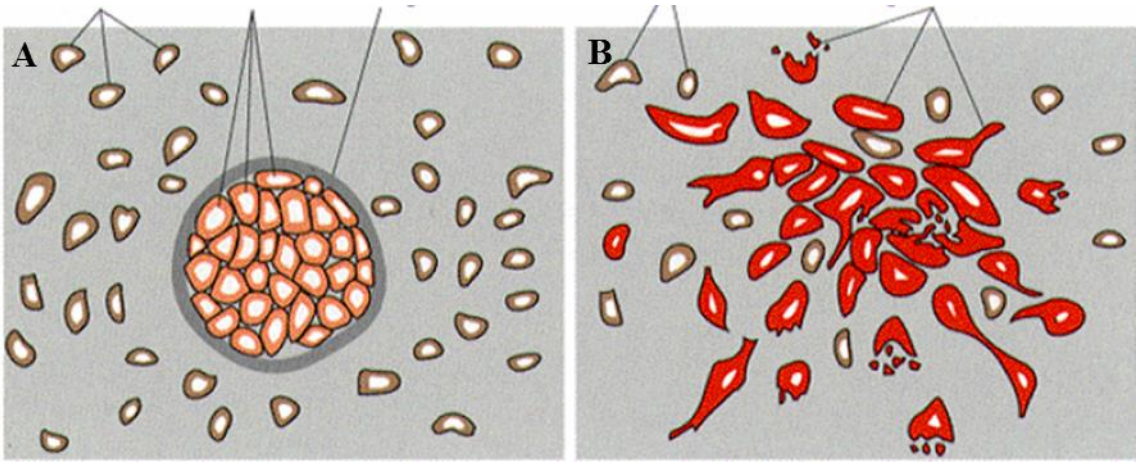

State of the Art, Figure1.1: (A) Benign tumours; (B) Malignant tumours.

The progression from normal cells to cancer cells involves multiple steps known as malignant progression.

The stages of development of a tumour starts with an uncontrolled growth of proliferating cellular clones due to acquisition of self-sufficiency in growth signals,

insensitivity to anti-growth signals, ability to evade apoptosis, and limitless replicative potential. This phase is called hyperplasia. Subsequently, epithelial tissues start to lose their architecture and uniformity leading to a dysplasia and the consequent formation of the primary tumour *in situ*. At this stage, tumour proliferation is limited by the availability of oxygen and nutrients, especially in its inner parts. The tumour mass continues to grow spherically until the formation of a necrotic core that leads the tumour to reshape itself acquiring the characteristic smash form in order to maximize the surface-volume ratio and thus maximise the nutrient diffusion in the tumour itself. The continue tumour growth depends upon recruitment of new blood vessels from nearby vasculature, which is called "angiogenesis". This process is also vital for tumour dissemination, in fact, at a certain point, the *in situ* tumour growth must stop and, in order to survive, it has to reach new sites. So we can see the formation of off-shoots and the consequent detachment of these from the tumour itself. After the alterations in cell–cell and cell–matrix cohesion and the disruption of the surrounding tissue architecture by proteases production, tumour cells invade the adjacent tissues through the basement membrane and spread, *via* blood vessels and lymphatic channels, to distant sites leading to the metastasis formation [8].

Metastasis is often described as a 'cascade' of events, since there are many steps, all of which are interconnected through a series of adhesive interactions and invasive processes, as well as responses to chemotactic *stimuli*. A tumour cell needs to successfully complete the entire cascade to form a secondary-site metastasis. The steps involved in the metastatic cascade are illustrated in State of the Art, Figure 1.2 and can be summarised as follows:

1. The development of a new blood supply to the growing tumour (angiogenesis).
2. The escape of tumour cells from the primary tumour mass.
3. Invasion of, and migration through, the basement membrane (BM) and extracellular matrix (ECM) surrounding the tumour epithelium, and subsequent invasion of the basement membrane supporting the endothelium of local blood vessels (or lymphatics).
4. Intravasation of the tumour cells into the blood vessel (or lymphatic), prior to hematogeneous (lymphagenous) dissemination to distant anatomical sites.
5. Adhesion of the circulating tumour cells to the endothelial cell lining at the capillary bed of the target organ site.
6. Invasion of the tumour cells through the endothelial cell layer and surrounding basement membrane (extravasation) and target organ tissue.
7. Colonozation the secondary target organ site and growth of tumour foci.

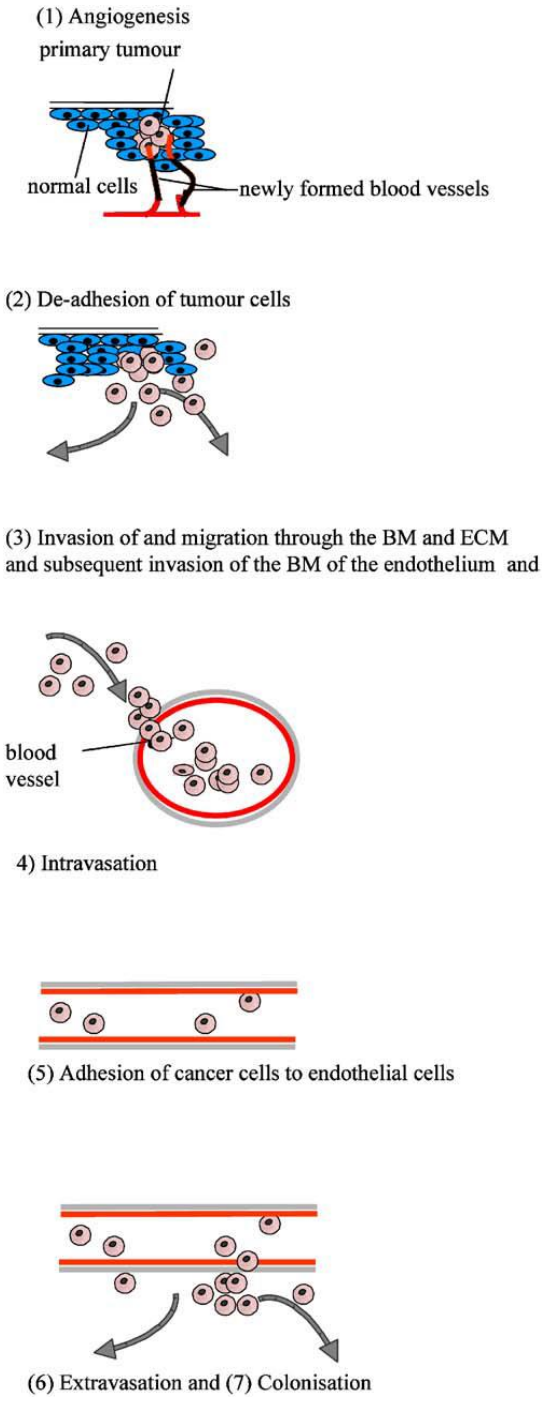

State of the Art, Figure 1.2:
The metastatic cascade. ***Reprinted from [8].***

Stage 3, 4 and 6 of the metastatic cascade, *i.e.* intravasation, extravasation and secondary site extravasation of tumour cells, respectively, requires the degradation of the BM that composes the blood vessels along with the ECM. During the metastatic dissemination of tumour cells, this process is supported by the action of several hydrolytic enzymes, released either by the tumour cells themselves or by cells surrounding the tumour, such as cathepsins and several matrix- metalloproteinases (MMPs) [9]. Since that,

MMPs in tumour tissues are up-regulated leading to their over-expression at tumour site [8].

Finally, once tumour cells reach the secondary site, they may be destroyed, may lie dormant or may proliferate to form secondary tumours [9].

Cancer Therapies and their Limits

From Hippocrates' times to the post-genomics era, humans have undertaken a war against cancer. Over the past one and a half centuries, numerous questions were asked, countless hypotheses were formulated and tested but this war has not been completely won yet. Despite that, a massive scientific activity and research in this field has identified the current options to treat cancer [10].

Since the term "cancer" refers to a class of diseases, it is quite unrealistic to try to identify a single cure for it. Indeed, cancer can be treated by surgery, chemotherapy, radiation therapy and immunotherapy. The choice of treatment depends upon the location, the grade of expansion and the stage of the tumour, as well as the general state of the patient. Complete removal of the cancer without damaging healthy tissues is the final goal of the cure. Sometimes this goal can be accomplished by surgery, but the propensity of cancers to invade adjacent tissue or to spread to distant sites by microscopic metastasis often limits its effectiveness. Another approach to reach this goal is the treatment of cancer with drugs that can destroy cancer cells, namely chemotherapy. Generally, chemotherapeutic agents interfere with cell division in various possible ways, e.g. with the duplication of DNA or the separation of newly formed chromosomes. Most forms of chemotherapeutic agents target all rapidly dividing cells and are not specific to cancer cells, although some degree of specificity may come from the inability of many cancer cells to repair DNA damage, while normal cells generally can. Hence, chemotherapy has the potential to harm healthy tissue, especially those that have a high replacement rate (e.g. intestinal lining) [9].

In the light of these considerations, Paul Ehrlich, a pioneer in the concept of chemotherapy, in 1900 pointed out the need of a site-specific delivery of the drugs, in order to avoid off-site cytotoxicity. Ehrlich introduced the receptor theory, through which drugs were described as "magic bullets" that would go straight to their specific targets in

the body. This new concept paved the way for the idea of cancer targeted medicine which was implemented only few years later [10].

Nanotechnology and Nanomedicine

"Atoms are elementary substances invisible and indivisible; they compose the perceptible matter and are its invisible substance or essence."

This is how Leucippus at the end of the VII century a.C. describes its Atomism theory. This is the proof that the awareness that there are small things in the word that are not visible to the naked eye extends back into human history.

During the first two decades of 1900, the development of the natural science created an interest in the micro- and nano-world, in order to enable a better understanding of the nature and the processes therein. Therefore, the development of new microscopic imaging methods represents certain milestones in the natural science. The consequent extension of the resolution limit of the microscopes led to construction of instruments with the capacity to resolve objects below the wavelength of the light. The field ion microscopes, the electron microscope, and finally the family of scanning probe microscopes give the possibility to image individual molecules and even single atoms.

In this context nanotechnology was born as a branch of applied science and technology that deals with the control of the matter at dimensions typically between 1 and 100 nanometers and the design and production of devices in this scale. It is a new born and heterogeneous discipline, ranging from physics and engineering to biology, that can leads to new perspectives on the development of materials and devices with a wide range of applications such as in medicine, electronics and for the production of innovative biomaterials [11].

In the area of medicine, the field of nanomedicine is defined as the monitoring, repair, construction, and control of human biological systems at the molecular level, using engineered nanodevices and nanostructures. As a parallel off-shoot of nanotechnology, nanomedicine controls matter and events in the nanometres scale range of often less than 100 nm. This allows a superior way to biologically control, at the subcellular level, the treatment and diagnosis of disease progression, detection and intervention. Thanks to its interconnected domains of engineering, chemistry and biology, nanomedicine is continually modifying the current approaches for disease management and diagnosis [12].

Particle-Based Drug Delivery for Cancer Treatment

As previously mentioned, chemotherapy-based cancer treatment has the potential to harm healthy tissues [9]; since that, Richard Feynman, in his talk "There's Plenty of Room at the Bottom" [13], pointed out the streaking need of developing nano-drug delivery devices capable of interacting with the body at the cellular level in order to guide and modulate drug delivery. In this context NPs based drug delivery was born. Indeed, these "nano-devices" are the nanoparticles, which are objects with a size below 100 nm that can be used as drug transporters and behave as a whole unit with the drug itself. Those nano-structured carriers may be fabricated from a practically limitless variety of organic and inorganic materials but the mostly used for biomedical applications are biodegradable and biocompatible polymers which offer almost unlimited possibilities of modifying their characteristics in order to achieve specific needs. These nanodevices provide a versatile platform onto which many functions can be added and addressed. Indeed, a well-designed drug delivery system can potentially combine synergistic effects into a single "magic bullet", such as improving drug solubility, modulate drug release, enhance drug transport in the vasculature and across body barriers, deliver the drug to a specific site, allow a *stimuli-responsive* drug release and in general improve and optimize the performances of the free drug.

The most commonly used nanocarrier systems are liposomes, and polymer-based nanoparticles such as nanospheres, nanocapsules or micelles (State of the Art, Figure 1.3) [14].

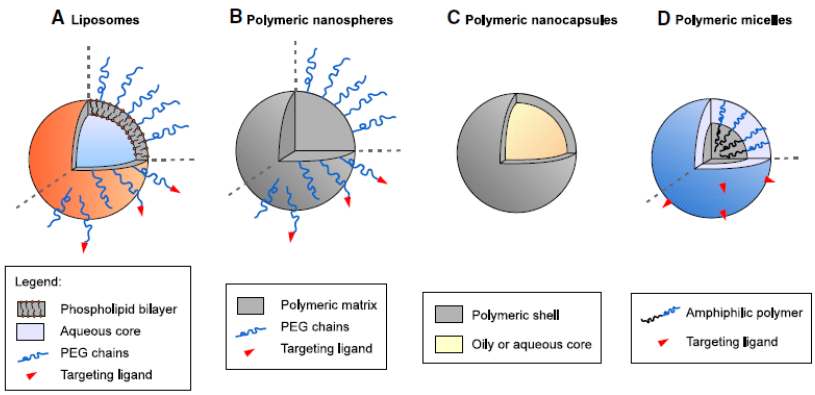

State of the Art, Figure 1.3: Principal types of nanocarriers for drug delivery. ***Reprinted from [14].***

When designing a nanocarrier for drug delivery applications, two basic requirements should be addressed. On one hand, once administrated, the drug should be able to reach the site of interest with minimal activity and volume loss in blood circulation. On the other hand, the drug should only harm tumour cells without damaging healthy tissue. These requirements could be meet taking advantages from two strategies: passive and active targeting (State of the Art, Figure 1.4) of tumour tissues [15].

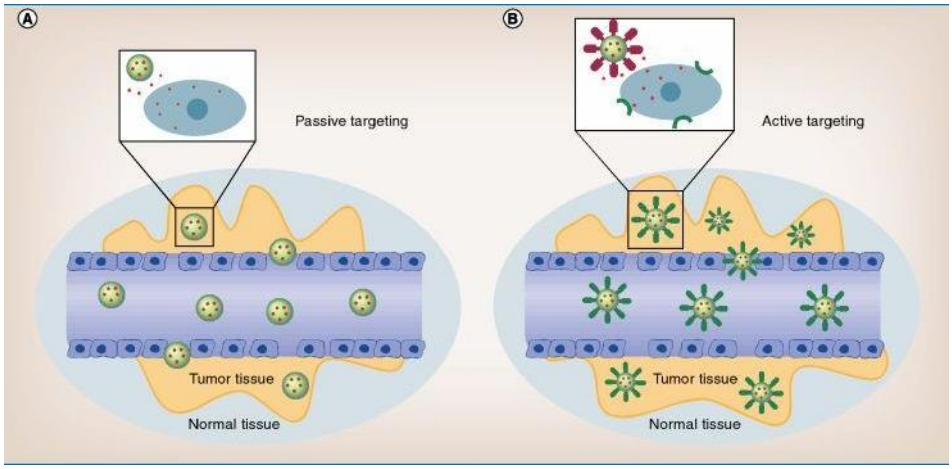

State of the Art, Figure 1.4: NPs targeting strategies. (A) Passive targeting; (B) Active targeting.

Passive targeting takes advantages from the enhanced permeability and retention (EPR) effect, which enables improved circulation of the nanocarrier with the accumulation through the characteristic leaky vasculature of the tumour. This strategy allows for an effective drug administration, simultaneously reducing the dose administered to the patient and increasing the one arrived at tumour site. A key challenge for improving the efficacy of passive drug delivery at tumour sites by a nanocarrier is to limit NPs interaction with the immune system and to maximize the EPR effect. To this aim NPs PEGylation, which is defined as the modification of a protein, peptide or non-peptide molecule by the linking of one or more polyethylene glycol (PEG) chains [16] [2], can be used. This polymer possesses a unique set of properties, including absence of toxicity, immunogenicity and antigenicity, low mass-dependent elimination *via* the kidney, high flexibility and high solubility in water and, last but not least, is FDA approved [17]. However, it is worthy to note that are now emerging new studies questioning the lack of immunogenicity of PEG. In fact, besides very positive clinical experience with PEGylated therapeutic agents, an increasing number of publications report that PEG can be highly immunogenic. Indeed, numerous works state the presence of anti-PEG antibodies in normal donors or patients and animals treated with PEGylated products [18].

On the other and, active targeting takes advantages from the NP functionalization with affinity ligands, such as antibodies, peptides or small molecules that only bind to specific receptors on the cell surface. Nanocarriers will recognize and bind to target cells through a ligand–receptor interaction. In order to achieve high specificity, those receptors should be significantly expressed on tumour cells, but not on normal cells.

In the light of these considerations, a smart approach to enhance drug delivery to solid tumours is the one that takes advantages from both passive and active targeting, combining their actions, as shown in figure State of the Art, Figure 1.5.

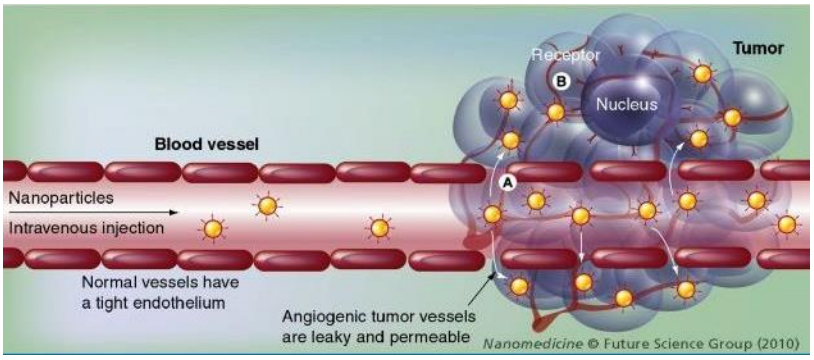

State of the Art, Figure 1.5: Enhanced drug delivery to solid tumours using nanoparticles. (A) Passive targeted delivery. After intravenous injection, nanoparticles accumulate in tumours through leaky and permeable tumour vasculature and impaired lymphatic system (e.g., enhanced permeability and retention effect). (B) Active targeted delivery. Ligand-coated nanoparticles bind to a cancer cell receptor resulting in cell-specific recognition and improved drug delivery to solid tumours.

Stimuli-responsive Drug Delivery

The *stimuli-responsive* nanocarriers (SRNs) are specialized nano-sized active delivery vectors that can modify their structural composition or conformation in response to a specific cellular/extracellular *stimulus* of chemical, biochemical, or physical origin thus promoting drug release to specific biological environment (State of the Art, Figure 1.6). The observed changes are mainly decomposition, isomerization, polymerization and activation of supramolecular aggregation among many others. In contrast to conventional nanocarrier complexes or conjugates, SRNs can undergo relatively large and abrupt physical and chemical changes in sharp response to applied *stimuli* [2] [12].

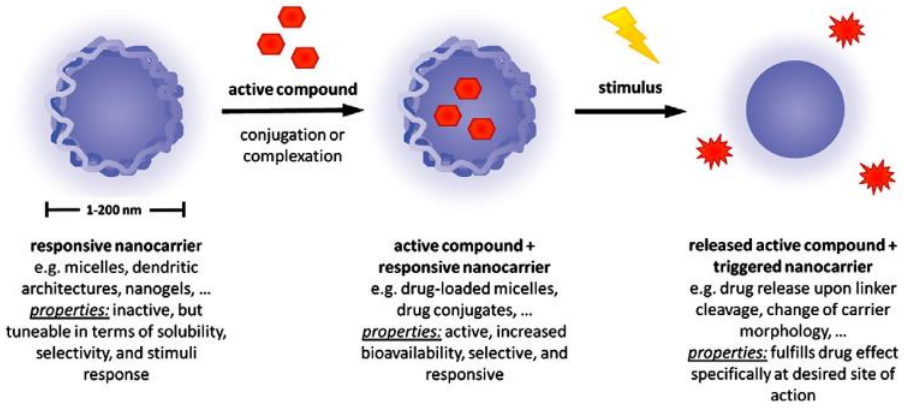

State of the Art, Figure 1.6: General scheme of a *stimuli-responsive* nanocarrier for the transport of active compounds. *Reprinted from [12].*

The general concept of triggered release can be mainly divided into two modalities according to the type of interaction between the drug and the nanocarrier, as shown in State of the Art, Figure 1.7.

In the complexation approach the drug is encapsulated into the nanocarrier and the release is promoted by structural changes within the carrier scaffold (*i.e.* carrier degradation, cleavage of shell, charging of functional groups), while in the nanocarrier-conjugate approach, the release mechanism involves the cleavage of the linker between the carrier and the drug [12].

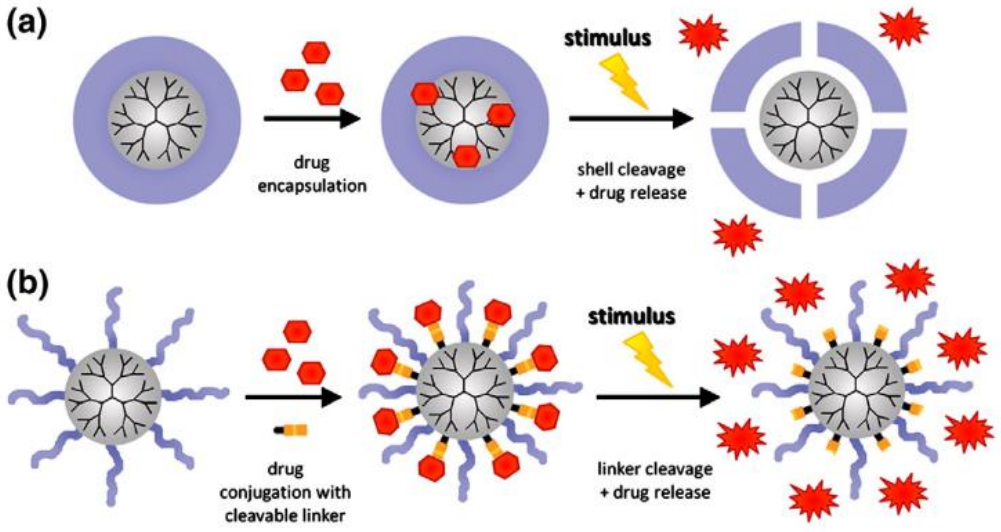

State of the Art, Figure 1.7: Different mechanisms for *stimuli-responsive* release of active agents from nanocarriers: (a) supramolecular complexes core-shell particles with cleavable shell and (b) nanocarriers with attached solubilising/stealth groups using cleavable linkers for the drug conjugation. *Reprinted from [12].*

The external *stimuli* that can induce these changes are numerous and cross-related and, thanks to these characteristics, nanocarriers thus become active participants in the therapeutic landscape, rather than inert carrier molecules.

The benefits of SRN are essentially important when the *stimuli* to which they response are specific biomarkers of malignant tissues (*i.e.* a definite enzyme class, specific protein over-expression, pH, electrolyte status). Such specificity allows the nanocarriers to release their cargo in a temporally or spatially controlled fashion in response to a particular pathological trigger occurring at the diseased tissues, substantially reducing side effects [12].

Numerous are the internal or external *stimuli* that can be exploited for triggering the delivery of chemotherapeutics, genes, or diagnostic agents from the nanocarriers. Though overlapping in many instances, these can be broadly classified with respect to the biological systems as either endogenous (physiological, pathological, and patho-chemical conditions) or exogenous (physical *stimuli*, *i.e.* heat, light, magnetic and electrical fields) (see State of the Art, Figure 1.8) [12].

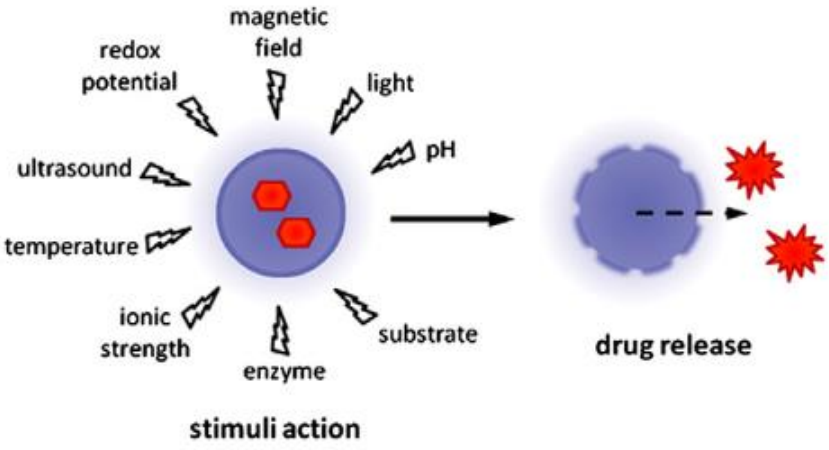

State of the Art, Figure 1.8: General scheme of *stimuli-responsive* release of a drug from a nanocarrier. *Reprinted from [12].*

Internal *stimuli* of chemical and biochemical origin include cellular pH-shift, redox, ionic microenvironment of the specific tissues, enzymes over-expression in certain pathological states, host–guest recognitions, and antigen–antibody interactions.

As an example, in the pathological state, the normal pH-gradient existing between extra and intracellular environment is greatly affected. A well-known fact is that in solid tumours, the extracellular pH can be more acidic (~ 6–7) than systemic pH (7.4) due to poor vasculature and consequent anaerobic conditions dominant in the malignant cells. Besides that, the cellular organelles also exhibit sharp pH differences in different locations,

for instance, in cytosolic, endosomal, and lysosomal compartments. A pH-sensitive polymeric nanocarrier can register such pH-gradients and, as a consequence, can facilitate drug release near the target compartment either by destabilization of the nanocarrier itself or by decomposition of the pH-sensitive linking unit that connects the drug to the carrier [12].

An array of manifold enzymes, such as proteases, glucuronidase, or carboxylesterases, which are expressed differentially and are either intra or extracellularly presented by normal and malignant cells, can be used as well as a biochemical trigger.

Generally, the proteases that are extracellularly expressed, such as the matrix metalloproteases, are specific biomarkers of malignant tissues and are responsible for the proteolysis of the extracellular matrix and basement membranes and are required during tissue remodelling and angiogenesis (see *"Cancer: Development and Metastasis Formation"*). These biochemical features can act as a trigger when spatially-oriented drug release is needed. This can be achieved by introducing specific enzyme substrate sequences, either into the nanocarrier scaffold, or in the linker segment through which the drug is anchored on to the nanocarrier [2] [12] [19].

A sum up of the above mentioned strategies for the use of *stimulus-sensitivity* are reported in State of the Art, Figure 1.9 [19].

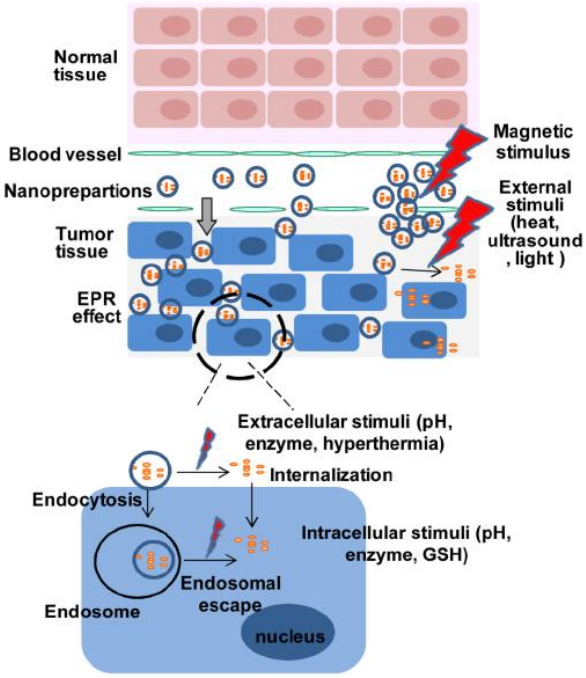

State of the Art, Figure 1.9: *Stimulus-responsive* delivery strategies for tumour targeting. *Reprinted from [19].*

In the light of these considerations, compared to the conventional drug delivery systems, the *stimuli-responsive* nanocarriers may provide a spatially-oriented and time-controlled drug release, responding to local *stimuli* that may come from the very nature of the tumour itself [19].

In Vitro Biological Models for Drug Screening

Along with the development of nanoparticles-based drug delivery, a striking need of preclinical tools for studying tumor behaviour and drug response was born.

In the first place, the two-dimensional (2D) cell cultures were routinely used to test cancer cells response to drug treatment. However, "flat biology" lacks in reproducing important physio- pathological features of the *in vivo* tissues, such as ECM expression. In the body, nearly all tissue cells reside in an extracellular matrix composed by a 3D fibrous meshwork that provides complex biochemical and physical signals. The ECM continuously interacts with the cells in a dynamic way and is of fundamental importance in guiding morphological changes and cellular organization. By contrast, cells cultured on 2D rigid substrates proliferate in an environment which lacks of the unique ECM of each cell type. These drawbacks can alter cells metabolism and reduce their functionality; for these reasons, drug screening conducted on 2D cell culture may lead to altered results [20].

In this scenario, three-dimensional (3D) culture systems have garnered much attention as robust research tools that can bridge the gap between the 2D culture system and the *in vivo* animal studies for both basic research and therapeutic development. Indeed, 3D culture systems resemble several aspects of the pathophysiological conditions in human tumour tissue. Among others, spheroids are one of the most commonly used 3D culture systems and are spherical clusters of cells formed by a self-assembling process. They may recapitulate avascular tumor nodules/micrometastases or intervascular sections of solid tumours with respect to micromilieu and volume growth kinetics. Moreover, they recapitulate morphological, functional and mass transport properties of the corresponding tissue *in vivo*, with tumour cells restoring an *in vivo*-like differentiation pattern due to the appropriate 3D extracellular matrix (ECM) assembly, complex cell–matrix and cell–cell interactions and authentic pathophysiological milieu conditions [21]. Nevertheless, 3D spheroids fail in reproducing tumour stromal microenviroment, which may contribute to tumour drug resistance by preventing the penetration of therapeutic agents. Moreover, the

absence of the stromal component does not allow the recreation of the correct stroma-tumour cross-talk, which is crucial in tumour developments [22]. In the light of these considerations, *Brancato et al.* [5] fabricated 3D microtissues with the aim to replicate *in vitro* the composition and the functionalities of the tumour microenvironment. This novel 3D cancer model better replicate the tumour physiology *in vitro* taking into account of the phenomena related to the tumor stroma remodeling by co-culturing tumor cells and cancer-activated fibroblast into porous gelatin microscaffolds. In this configuration, cells assemble an intricate network of collagen, fibronectin and hyaluronic acid. The results of their work clearly show that microtissues better recapitulate the important differences existing *in vivo* between normal and cancer-activated stroma representing a more valuable platform to mimic *in vitro* the stromal element of the tumour tissues.

Chapter.1 **Tumour Activated Pro-drug (TAP)-conjugated nanoparticles sensing the matrix metalloproteinase-2 for the on-demand release of anticancer drugs in 3D tumour spheroids**

ABSTRACT

The balance between dose-dependent tolerability, effectiveness and toxicity of systemically administered anti-tumour drugs is extremely delicate. This issue highlights the striking need for targeted release of chemotherapeutic drugs within tumours. In this work, a smart strategy of drug targeting to tumours relying upon biodegradable/biocompatible nanoparticles releasing cytotoxic drugs after sensing physiological variations intrinsic to the nature of the tumour tissues is exploited. In particular, the well-known over-expression of matrix metalloproteinase-2 (MMP-2) enzymes in tumours is chosen as a trigger for the release of a cytotoxic drug. Nanoparticles made up of a biodegradable poly (D,L-lactic-co-glycolic acid) (PLGA) – block – polyethylene glycol (PEG) copolymer (namely PELGA), blended with a tumour activated prodrug (TAP) composed by a MMP-2-sensitive peptide bound to doxorubicin (Dox) and to PLGA molecule were produced. The obtained devices are able to release Dox and to elicit cytotoxicity specifically upon MMP-2 cleavage of the TAP. More interestingly, they sense the differences in the expression levels of endogenous MMP-2 protein, thus modulating drug penetration within a three-dimensional (3D) tumour spheroid matrix, accordingly. Therefore, the proposed nanoparticles hold promise as a useful tool for *in vivo* investigations aimed at an improved therapeutic efficacy of the conjugated drug payload*.

*The work described in this Chapter is part of a published manuscript: M. Cantisani, D. Guarnieri, M. Biondi, V. Belli, **M. Profeta**, L. Raiola, *et al.*, "Biocompatible nanoparticles sensing the matrix metallo-proteinase 2 for the on-demand release of anticancer drugs in 3D tumour spheroids", *Colloids and Surfaces B: Biointerfaces*, vol. 135, pp. 707-716, **2015**.

Chapter 1 Tumour *Activated Pro-drug (TAP)-conjugated nanoparticles sensing the matrix metalloproteinase-2 for the on-demand release of anticancer drugs in 3D* tumour *spheroids*

KEYWORDS: Tumour activated prodrug, matrix metalloproteinase, microenvironmentally-triggered drug release, extracellular drug release, biodegradable nanoparticles, 3D tumour spheroids.

1.1 Introduction

The performance of systemic chemotherapy, accomplished with both traditional and innovative drugs, is restricted by a series of biological barriers hindering an effective drug delivery after intravenous administration. Actually, solid tumours have inherently aberrant features, such as a highly fibrous matrix and an abnormal blood flow in their inner regions, and frontier, which limit the delivery of drugs to the target tissue because of arterial-venous shunting and a strong interstitial pressure gradient [23] [24] [25]. Furthermore, only a tiny fraction of chemotherapeutic agent(s) can reach the tumour site because of their non-specific distribution and uptake by the reticuloendothelial system (RES) [26]. Therefore, the administered drug(s) accumulate within target tissues and healthy organs and, owing to their low therapeutic index, often entail severe side effects, such as irreversible cardiotoxicity and nephrotoxicity [27] [28] [29]. These characteristics, together with the susceptibility toward drug resistance, reduce the healing potential of anticancer drugs [30, 31] [32], thus highlighting the striking need for more effective strategies to release chemotherapeutic drugs within tumour sites.

In this context, drug-loaded nanoparticles (NPs) are recognized to be cardinal platforms [33]; indeed, their nanometric size, coupled with superficial poly(ethylene glycol) (PEG) segments, help to circumvent RES and, therefore, to release the drug payload preferentially to tumour tissues, taking advantage of the enhanced permeability and retention (EPR) effect, which results from the leakiness of the immature and non-organized vasculature of solid tumours [34]. Even though EPR effect does actually enable a preferential accumulation of carriers/drugs to tumour sites and some reduction of side effects, the actual benefit is unpredictable because of individual variations in tumour microenvironment [34] [35]. Actually, EPR allows only a few percent of intravenously administered NPs to accumulate at the target site [36] and, during their circulation in the bloodstream, NPs accumulate within the liver and spleen. This reduces the contact time between the NPs and the tumour site and, therefore, therapy effectiveness [37], thus resulting into a heterogeneous NP accumulation in the tumour, and an unsatisfactory increase in overall patient survival [38] [39] [40]. The specificity of chemotherapy action can be increased if NPs are endowed with functional moieties to provide an active targeting, which can in principle improve NP performance in terms of targetability, cellular penetration and sensitivity to specific internal *stimuli*, such as the acidic pH in tumour

microenvironment [41], altered redox potential [42], and up-regulation of specific proteins [43].

In this context, one strategy of drug targeting to tumours relies upon NPs releasing cytotoxic drugs by exploiting physiological variations that are intrinsic to the very nature of the tumour tissues. Indeed, compared to normal tissues, tumours secrete higher amounts of matrix metallo-proteinases (MMPs), which are proteolytic enzymes cleaving the natural extracellular matrix (ECM) of tumours and push tumour progression and metastasis [44] [45]. In particular, MMP-2 (also known as gelatinase A) plays a key role in tumour invasion and angiogenesis by hydrolyzing type IV collagen, which is a major constituent of tumour ECM [46] [47]. Therefore, NPs delivering chemotherapeutic agents in response to MMP-2 action offer the chance to exert their cytotoxic action toward target tumour sites with a high specificity, in order to prevent, or significantly reduce, the insurgence of toxic side effects against non-target tissues and organs.

In a recent study [48], we have synthesized two tumour-activated prodrugs (TAPs), composed by MMP-2-sensitive peptides bound to doxorubicin (Dox) and PEG, tethered to model polystyrene NPs. The resulting TAP-conjugated NPs could trigger Dox release only in the presence of MMP-2, while eliciting no cytotoxicity in the absence of enzyme pre-treatment. Inspired by these encouraging results, here we have translated the TAP production technology to the fabrication of biodegradable systems based on FDA-approved materials. To this aim, here we produced NPs made up of a biodegradable poly(D,L-lactic-co-glycolic acid) (PLGA) – block – PEG copolymer (namely PELGA), blended with a TAP composed by a MMP-2-sensitive peptide bound to doxorubicin (Dox) at the C-terminus and to PLGA molecule at the N-terminus (Figure 1.1). The design of this NP system merges several major drug delivery approaches, such as self-assembly, PEGylation and sensitiveness to endogenous *stimuli*, along with the concept of prodrug. The obtained devices were tested for their Dox release and ability to diffuse within a three-dimensional (3D) tumour matrix model. To test the biological effect of NPs, spheroids of human glioma cell line (U87-MG) and primary human dermal fibroblasts (HDF) were used as *in vitro* models of three-dimensional tumour and healthy tissues, respectively.

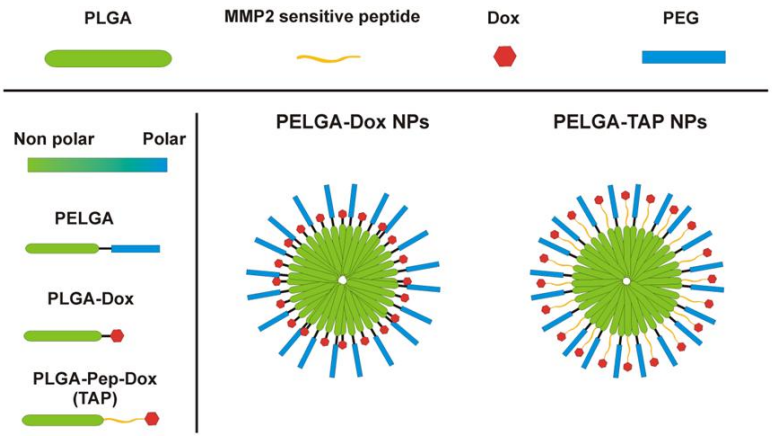

Figure 1.1: Schematic representation of PELGA-TAP and PELGA-Dox NPs formulations. ***Reprinted from [4].***

1.2 Materials and Methods

1.2.1 Materials

Equimolar uncapped poly(D,L-lactide-co-glycolide) (PLGA) (Resomer RG502H, Mw 12, 000 Da) was purchased from Boehringer Ingelheim (Ingelheim, Germany). Doxorubicin hydrochloride (Dox, purity>99%) was purchased from Discovery Fine Chemicals (UK). Polyethylene glycol (PEG, Mw 1500 Da), ethylenediamine, N,N-diisopropylethylamine (DIEA), O-benzotriazole - N,N,N', N' – tetramethyluronium – hexafluoro – phosphate (HBTU), anhydrous N,N – dimethyl-formamide (DMF), N,N' – diisopropylcarbodiimide (DIC), 4-(dimethylamino) pyridine (DMAP), dichloromethane (DCM), sodium dihydrogen phosphate, disodium hydrogen phosphate, 1-ethyl-3-(3-dimethylaminopropyl)- carbodiimide hydrochloride (EDC-HCl) piperidine, trifluoroacetic acid (TFA), 2 – (N-morpholino) – ethanesulfonic acid (MES) sodium salt, *p* – aminophenylmercuric acetate (APMA), *tris* – HCl, acetonitrile (ACN), HPLC – grade water and all buffer solutions were purchased from Sigma-Aldrich (USA). All 9-fluorenyl methoxy carbonyl (Fmoc) – aminoacids were purchased from IRIS Biotech GmbH (Germany). Recombinant Human matrix metalloproteinase – 2 from Peprotech Inc. (USA) was used. Dialysis bags (MWCO 6000-8000 Da) were obtained from Spectrum Laboratories, Inc. (The Netherlands), while distilled and deionized water (18MΩ resistance) were from Millipore (USA).

1.2.2 Synthesis of copolymers and conjugates

PLGA-PEG copolymer (namely PELGA) was synthesized *via* a coupling reaction between PLGA and PEG according to a previously published procedure [49]. Briefly, the carboxyl group of PLGA was functionalized by ethylendiamine (1 eq: 1 eq) in order to react with carboxyl-modified PEG. 1 eq of PLGA-NH2, 4 eq of PEG-COOH and DMAP and 2 eq of N,N'-Dicyclohexylcarbodiimide, (DCC) were dissolved in 20 ml of anhydrous DCM. After the reaction, which was carried out for 2 days at room temperature (RT) under inert atmosphere, the residual DCC was changed into dicyclohexylcarbodiurea (DCU) by

adding 10 µL of bidistilled water and DCU was removed by filtration. The residue was then precipitated in methanol at 4 °C and dried overnight under vacuum.

PLGA-Dox and PLGA-TAP copolymers were synthesized according to the scheme reported in Figure 1.2. Briefly, the MMP-2-sensitive Fmoc – Gly – Pro – Leu – Gly – Ile – Ala – Gly – Gln – COOH peptide was synthesized using standard solid phase Fmoc method [48]. Then, the peptide – Dox conjugates were synthesized by a standard coupling procedure using HBTU as coupling reagent. Peptides (1 eq), HBTU (1 eq), DIEA (2 eq), and Dox (1.5 eq.) were dissolved in anhydrous DMF. The reacting mixture was continuously stirred overnight and the reaction products were verified by analytical RP-HPLC. After the coupling reaction, piperidine was added into the reactor to obtain a 40% v/v solution for the removal of Fmoc group from the peptide – Dox conjugates. The reaction mixture was precipitated from DMF solution with cold ethyl ether and the residue was dissolved in a 30/70 (v/v) acetonitrile (ACN)/water solution containing 0.1% v/v TFA and purified by RP-HPLC. Finally, the PLGA-peptide-Dox (TAP) conjugate was synthesized by a standard HBTU coupling procedure, as described above. Briefly, PLGA (1 eq), HBTU (1 eq), DIEA (2 eq), and peptide-Dox conjugates (1.5 eq.) were dissolved in anhydrous DMSO. Subsequently, the copolymer was purified by removing the unreacted reagents using dialysis bags (MWCO 6000 – 8000 Da) and lyophilized. Furthermore, as a negative control, to evaluate specific MMP-2 enzyme cleavage on nanoparticles, a PLGA-Dox conjugate without the MMP-sensitive peptide was synthesized and purified as reported above. In particular, PLGA (1 eq), HBTU (1 eq), DIEA (2 eq) and Dox (1.5 eq) were used.

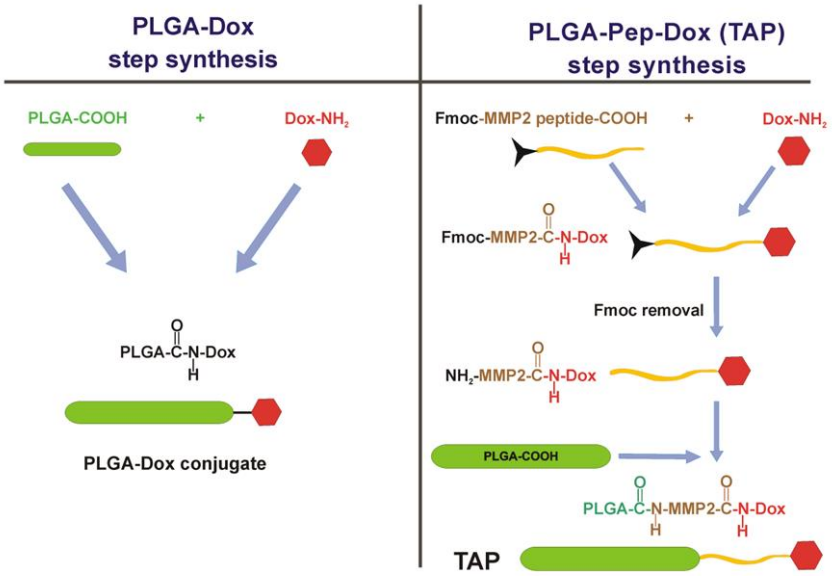

Figure 1.2: Step synthesis of PLGA-Dox and PLGA-TAP copolymers. ***Reprinted from [4].***

Nuclear Magnetic Resonance (NMR) spectra were recorded using an Agilent 600MHz (14 T) spectrometer equipped with a DD2 console and an OneNMR HX probe. PLGA-Dox and PLGA-Peptide-Dox samples (1 mg) were dissolved in 600 µl of 99.9% deuterated DMSO (Sigma Aldrich). ^{1}H 1D spectra were recorded at 300 K using 1024 scans to obtain a good signal to noise ratio for peptide and Dox components. A double saturation PRESAT pulse sequence was used to reduce residual peaks of DMSO and water at 2.5 and 3.3 ppm respectively. Spectra were transformed and analyzed using VNMRJ 4 software. Chemical shift scale was referenced on the solvent residual peak signal.

1.2.3 NP preparation

PELGA-TAP NPs were prepared according to the nanoprecipitation method. Briefly, 1 mg of PELGA and 1 mg of TAP were dissolved in 500 µl of acetone and the obtained solutions mixed. Afterwards, the solution was added dropwise (6 ml/h) with a syringe pump into 12.5 ml of distilled water under magnetic stirring (600 rpm). The organic solvent was then evaporated for 3 h in continuous stirring and the obtained NPs dispersion sterilized with 0.22 µm membrane filter. Finally, the volume of the solution was reduced to 1 ml by centrifugation using Amicon Ultra-4 10 kDa centrifuge tube (Millipore), to have a final NPs concentration of 2 mg/ml. The control NPs (without the MMP-sensitive linker) were prepared with the same technique using 1 mg of PLGA-Dox and 1 mg of PELGA.

1.2.4 NP size, stability and morphology

NP mean size, size distribution and ζ-potential were determined by dynamic light scattering technique (ZetaSizer Nano ZS, Malvern Instruments, Malvern, UK) on a 0.1 mg/ml suspension of NPs in water (12 runs each sample). To assess NPs stability over the time, mean size and size distribution measurements were carried out also 1, 7 and 14 days after their preparation and stored at 4 °C in the meantime. Results were averaged on at least five measurements.

PELGA NPs morphology was analysed by scanning electron microscopy (SEM) and cryogenic transmission electron microscopy (Cryo-TEM). SEM samples were prepared depositing 50 µl of NPs suspension on a cover slip mounted on a standard SEM pin stub. The samples were gold-sputtered (3 nm thickness) with a HR208 Cressington sputter coater and analysed by FESEM ULTRAPLUS (Zeiss) at 20 kV with the SE2 detector and 15.9 mm working distance. Cryo-TEM samples were vetrified with FEI Vitrobot Mk IV in a saturated water vapour environment. Sample volumes of 3 µl were placed on 200 mesh Quantifoil grids and the excess sample was blotted away with filter paper. Blot time and drain time were both 1 s. After blotting, the grids were plunged into liquid propane that was cooled with liquid nitrogen surrounding the propane vessel. Imaging was performed with TEM TECNAI G^2 equipment operating at 200 kV in low dose mode and acquired by Eagle 2HS camera.

1.2.5 In vitro kinetics release of Dox

Dox release kinetics were evaluated *in vitro* by MMP-2 cleavage assay, performed in MMP-2 buffer solution according to a previously reported procedure [48]. Prior to release experiments, MMP-2 solution was activated with 100 µM APMA solution for 3 h at 37 °C to a final 20 nM enzyme concentration. For release tests, 500 µl of NPs suspension, in presence or absence of 20 nM activated MMP-2 enzyme, were poured in a dialysis tube (MWCO 6000 – 8000 Da), which was placed in 12.5 ml of buffer solution (50 mM HEPES, 200 mM NaCl, 10 mM $CaCl_2$, 1 mM $ZnCl_2$, pH 7.4) at 37 °C under stirring (100 rpm). At scheduled time points, 120 µl of released medium were withdrawn and the released drug quantified by spectrofluorimetric assay interpolating the experimental data with a calibration curve. Dox wavelength of excitation and emission were determined

acquiring its adsorption and emission spectrum (Figure 1.3). Dox adsorption wavelength is 483 nm, in the light blue, while its wavelength of emission is between 560 and 620 nm, emitting both in the red and in the green. Since that, the parameters chosen for our acquisitions were: λ_{ex} = 485 nm and λ_{em} = 595 nm.

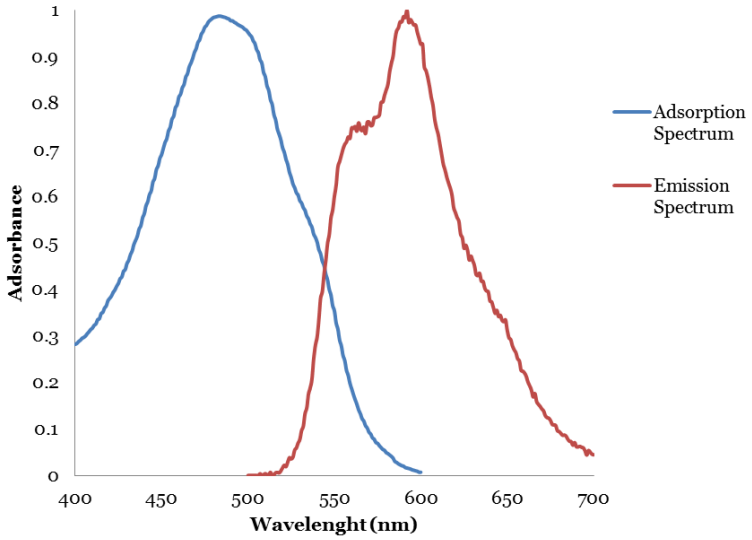

Figure 1.3: Dox excitation and emission spectra.

Finally, to evaluate the specific recognition of the MMP-2 sensitive peptide sequence, the same experiment was performed on PELGA-Dox NPs, without the MMP-sensitive linker, as negative control.

1.2.6 Cell culture

To test the biological effect of NPs, human glioma cell line (U87-MG) and primary human dermal fibroblasts (HDF) were used as models of tumour and healthy tissues, respectively. The latter were purchased by ECACC and cultured in Eagle's minimal essential medium (EMEM) supplemented with 20 % fetal bovine serum (FBS, Gibco), 100 U/ml penicillin, 100 mg/ml streptomycin and 2X non-essential amino-acids. U87-MG (ATCC) cells were cultured with complete medium, composed of EMEM supplemented with 10 % FBS, 100 U/ml penicillin, 100 mg/ml streptomycin. Cells were incubated in a humidified controlled atmosphere with 95:5 volume ratio of air/CO_2, at 37 °C. The medium was changed every 2-3 days.

1.2.7 Indirect immunofluorescence of MMP-2 protein

For indirect immunofluorescence, 3 x 10^4 cells were seeded in 1 ml of medium on fluorodish – 35 mm (World Precision Instruments, Inc). Briefly, the cells were rinsed twice with PBS and fixed with 4 % paraformaldehyde for 20 min. Then, cells were incubated with Triton X 100 0.1 % in PBS for 10 min and with PBS-BSA 0.5 % for 15 min at room temperature (RT). MMP-2 expression was detected by incubating each sample with rabbit anti-MMP-2 (Abcam) primary antibodies. After primary antibody incubation, Alexa Fluor 488 goat anti-rabbit secondary antibodies (Molecular Probes, Invitrogen) were used. Afterwards, the samples were rinsed three times with PBS-BSA 0.5 %. The cell nuclei were stained with DAPI. Immunofluorescence analyses were performed by a confocal and multiphoton microscope system (Leica TCS SP5 MP). Images were acquired with a resolution of 1024 x 1024 pixels by an oil-immersion 63× objective.

1.2.8 Gelatin zymography

MMP-2 enzymatic activity in cellular extract of U87-MG and HDF cell types was determined by SDS-PAGE gelatin zymography. Gelatinases present in the extracts are able to degrade the gelatin matrix, leaving a clear band after staining the gel protein [50] [51]. Briefly, an equal amount of protein for each sample was loaded on the 10 % SDS-PAGE gel containing 2 % of gelatin. The gel was equilibrated in the zymogram renaturation buffer (Bio-rad) for 30 min at RT with gentle agitation, before being incubated in zymogram development buffer (Bio-rad) at 37 °C overnight. Afterwards, the gel was stained with Coomassie Blue dye (Invitrogen) and photographed after bleaching in destaining solution.

1.2.9 Spheroids formation

To verify the penetration of Dox within tumour matrix as a function of MMP-2 triggered release, tumour spheroids were used as *in vitro* drug screening platform. Tumour spheroids were prepared by optimizing the procedure described by *Guarnieri et al*. [52]. Briefly, a confluent monolayer of cells was trypsinized and about 2500 U87-MG and 3000 HDF cells per spheroid were suspended in the culture medium containing 0.25 % (w/v)

carboxymethylcellulose, seeded onto non-adherent round-bottomed 96-well plates (Greiner, Frickenhausen, Germany), and cultured at 37 °C, 5 % CO_2, 100 % relative humidity. These spheroids were harvested within 24 h, centrifuged for 5 min at 1000 rpm, and suspended in cell culture media in low-attachment 6-well plates. Approximately 6-10 spheroids were suspended in each well with cell culture medium, containing free Dox (4 µg/ml), PELGA-Dox NPs and PELGA-TAP NPs, and incubated at 37 °C. Positive control samples were treated with cell culture medium only. After 24 and 48 h, spheroids were fixed with 4 % paraformaldehyde and observed by confocal multiphoton microscope with a 10× objective. Z-sectioning images were acquired with a resolution of 1024×1024 pixels and a z- slice thickness of about 20 µm. The fluorescence intensity profile of Dox diffused into the spheroid matrix was measured by LAS-AF software (Leica). Data were reported as the distribution of normalized pixel counts as a function of gray scale value of each pixel ranging from 0 to 255.

1.2.10 Statistical analyses

Quantitative data are reported as mean value ± standard deviation (SD). The statistical significance of the results was assessed by one-way analysis of variance ANOVA. A p value <0.05 was considered to identify statistically different groups.

1.3 Results

1.3.1 Synthesis of copolymers and conjugates

PLGA-Dox and PLGA-TAP copolymer were synthesis following the scheme reported in Figure 1.2. MMP-2 sensitive peptide was obtained with a good yield; crude peptides were purified to homogeneity (> 95%) on preparative High Performance Liquid Chromatography (HPLC) and their presence was confirmed by ESI-LC-MS analysis (Figure 1.4 A and B) [48]. As for PLGA-peptide-Dox (TAP) synthesis, pure Fmoc-peptides, with free carboxylic C-terminus, were conjugated to Dox by amide bond formation and purified with HPLC. The presence of the conjugate was confirmed by HPLC (Figure 1.4 C and D), by simultaneously measuring Fmoc and Dox spectra. Afterwards, the Fmoc group on N-terminus was removed by piperidine treatment and purified by HPLC (Figure 1.4 E and F). Peptide-Dox conjugates were linked to PLGA by amide bond formation and the reaction product was dialyzed against DMSO and water to remove excess reagents.

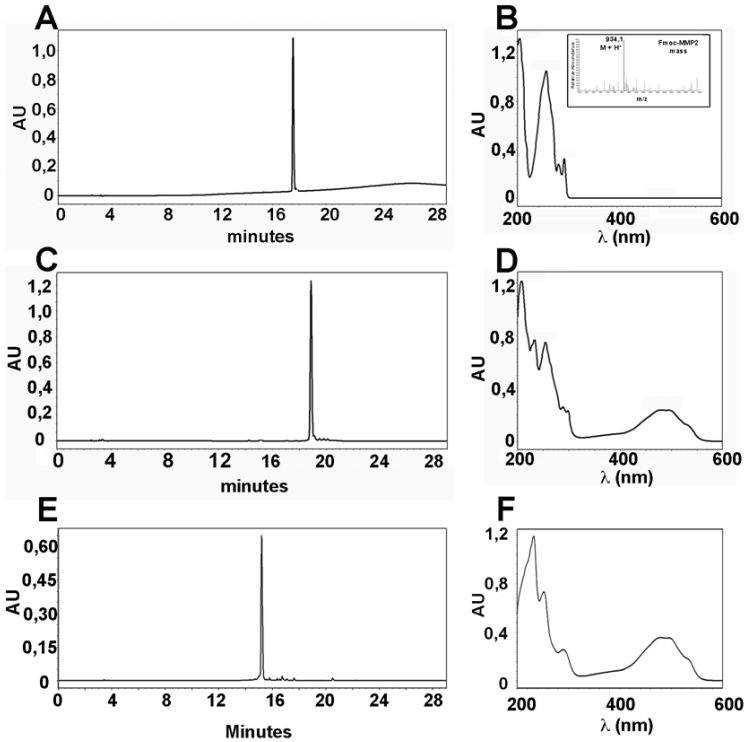

Figure 1.4: HPLC, absorbance and mass spectroscopy analysis of the MMP-2 sensitive peptide-Dox conjugate. HPLC traces and absorbance spectra of: MMP-2 sensitive peptide (A and B), Fmoc-peptide-Dox conjugate (C and D) and de-protected peptide-Dox adduct (E and F); mass spectroscopy profile of the MMP-2 sensitive peptide (B, inset). ***Reprinted from [4].***

PLGA-Dox and PLGA-Peptide-Dox synthesis was verified using NMR spectroscopy. Comparing ^{1}H 1D spectra of pure PLGA and Dox compounds in DMSO with PLGA-Dox spectrum we confirmed that the PLGA-Dox product was effectively formed using our procedure (Figure 1.5). Chemical structures of PLGA and Dox are associated to their NMR spectra. In the PLGA spectrum, peaks A and B at 5.18 and 1.41 ppm correspond respectively to CH and CH_3 protons of PLGA lactic acid part where peak C at 4.85 ppm corresponds to CH_2 protons of PLGA glycolic acid part. In the Dox spectrum, very important signals are peaks 1, 2 and 3 in the 8.0-7.5 ppm region corresponding to aromatic protons, peak 4 at 3.97 ppm corresponding to ether OCH_3 protons and peak 5 at 1.14 ppm corresponding to aliphatic CH_3 protons. In the PLGA-Dox spectrum, characteristic peaks of both PLGA and Dox are distinguishable confirming the formation of the PLGA-Dox molecule. Peak at 2.47 ppm is the DMSO residual signal.

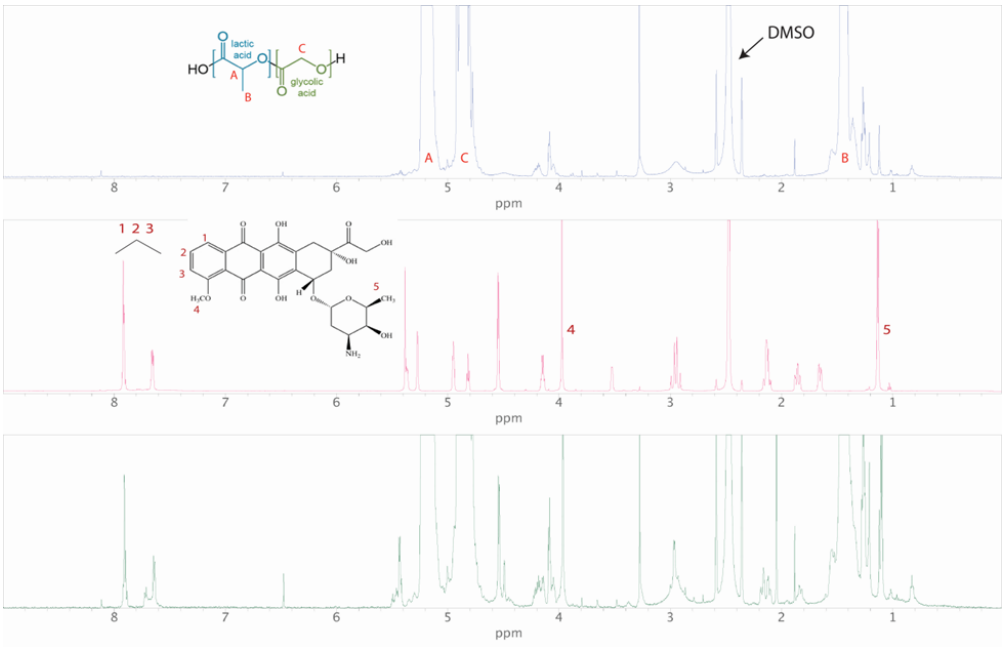

Figure 1.5: 1H 1D NMR spectra of PLGA (blue), Dox (pink) and PLGA-Dox molecule (green) in DMSO. ***Reprinted from [4].***

^{1}H 1D NMR spectra of PELGA-Dox and PLGA-Peptide-Dox samples are shown in Figure 1.6. PLGA-Peptide-Dox spectrum contains several peaks not present in PLGA-Dox spectrum. In particular, we focus our attention on the spectral region between 9 and 7 ppm and in the region between 1 and 0 ppm. Peaks with chemical shift values lower than 1 ppm are typically associated with methyl groups of Leu, Ile or Val residues. In the regions between 9 and 7 ppm, furthermore, we find amide protons of backbone peptidic bounds. Figure 1.6 B shows a zoom of the region between 8.5 and 7 ppm where, in PLGA-Peptide-

Dox spectrum, doublets at 7.86 and 7.82 ppm, triplet at 7.39 ppm and partially superimposed triplets at 7.33 and 7.32 ppm are typical signals of peptide backbone NH.

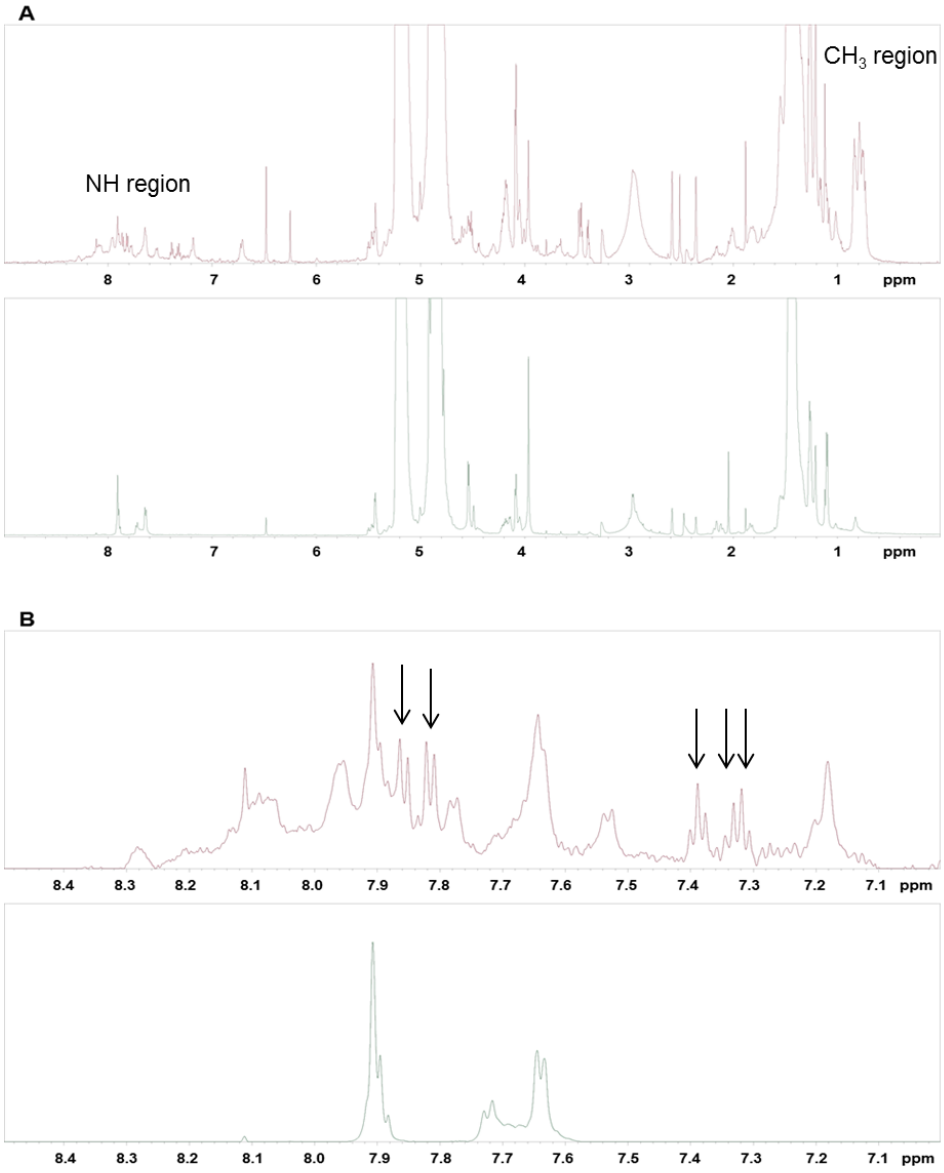

Figure 1.6: ^{1}H 1D NMR full spectra (A) and a zoom of 8.5-7.0 ppm region (B) of PLGA-Peptide-Dox (red) and PLGA-Dox (green) molecules in DMSO. *Reprinted from [4].*

In Figure 1.6 panel A, CH_3 aliphatic region and NH amide backbone region are underlined in the PLGA-Peptide-Dox spectrum. In panel B, arrows show peptide backbone NH signals in PLGA-Peptide-Dox spectrum.

1.3.2 NPs mean size, ξ-potential and stability

PLGA-TAP and PLGA-Dox were mixed with PELGA copolymer [53] in acetone for NPs production, according to the procedure described above. The produced NPs were characterized in terms of size, ζ-potential and stability and morphology. DLS measurements show that NPs diameter is below 100 nm with a polydispersity index (PDI) less than 0.2 with and without TAP. The surface charge is negative, with very slight differences among the NPs (Table 1.1).

Sample	Dox/NP [μg/ml]	Mean size [nm ± SD]	PDI	ζ-potential [mV ± SD]
PELGA-TAP	~ 20	75.1 ± 0.5	0.186	- 29.5±4.8
PELGA-Dox	~ 21.5	62.0 ± 0.9	0.167	-23.6±12.8

Table 1.1: Formulation, size, polydispersity index (PDI) and ζ-potential of PELGA-TAP and PELGA-Dox NPs. Data are reported as mean ± SD. $p < 0.05$ was considered statistically significant. *Reprinted from [4].*

In particular, PELGA-TAP NP show a slightly enhanced size probably because of the peptide interaction with water since DLS analysis give us indirect information concerning the hydrodynamic diameter, which is always higher if compared to the NP diameter shown in morphological analysis. These observations are in agreement with previous works. In fact, Danhier et al. [54] prepared PLGA nanoparticles blended with PLGA-b-PEG with and without the presence of the RGD peptide sequence, according to the nanoprecipitation method. DLS measurements performed on both kind of NP show that the presence of the RGD peptide, which is composed by only 3 aa, entails an increase of about 24 nm in nanoparticle size. Moreover, Li et al. [55] covalently conjugated a 12-aminoacid-peptide onto the surface of PEG-PLGA based NPs prepared according to the emulsion/solvent evaporation method. In particular, they prepared blank NPs without the presence of the peptide and two types of functionalized NPs with a peptide/maleimide-polymer ratio of 1:3 and 1:1, namely TGN-NPs (1:3) and TGN-NPs (1:1) respectively. DLS data showed a 5 nm difference in size between blank and TGN-NPs (1:3); this difference increased in the case of TGN-NPs (1:1) to 15 nm. In these articles, NPs were prepared with two different methods and the peptide sequences involved in the NP functionalization process were

different in composition and length. Nevertheless, in both cases was observed an increase in NP hydrodynamic radius in presence of a peptide sequence when compared to the blank NP.

DLS measurements were performed also at 1, 7 and 14 in water. Data show a very slow increase in NPs size over time and a good colloidal stability up to 14 days, as can be seen in Figure 1.7.

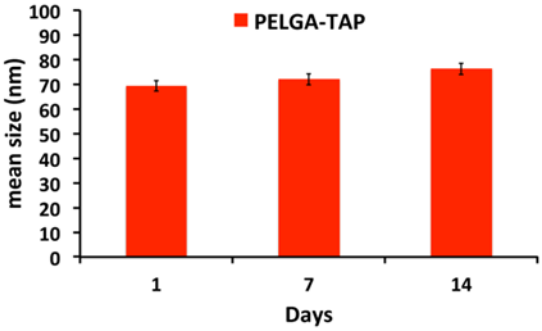

Figure 1.7: Time evolution of the hydrodynamic diameter of PELGA-TAP NPs in aqueous suspension obtained by DLS measurements. PDI was < 0.2 in all cases. *Reprinted from [4].*

1.3.3 NPs morphological characterization

SEM and Cryo-TEM images of PELGA NPs are displayed in Figure 1.8, panel A and B respectively. Images show that NPs are spherical and with a regular shape.

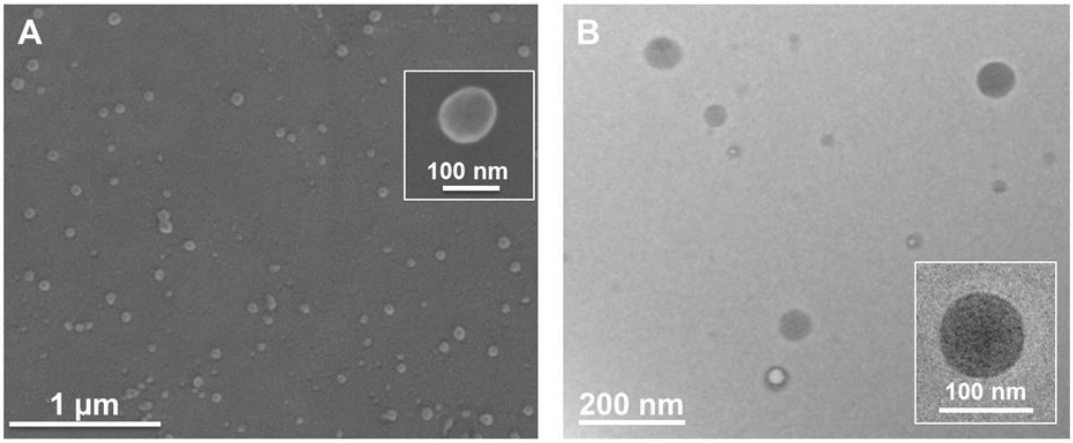

Figure 1.8: SEM of PELGA-TAP NPs (A) and Cryo-TEM of PELGA-Dox NPs (B). Insets A and B show images at higher magnification. *Reprinted from [4].*

1.3.4 Doxorubicin in vitro release kinetics from PELGA-TAP nanoparticles

The produced PELGA-TAP NPs were tested for their ability to release Dox *in vitro* upon exposure to free MMP-2 enzyme. To this aim, the cleavage assay was performed by incubating the particles with or without 20 nM MMP-2 at 37°C for 48 h. The *in vitro* release profiles of Dox from PELGA-TAP NPs in presence or absence of the enzyme are plotted in Figure 1.9 A. It can be seen that, in absence of MMP-2 enzyme, 25% of Dox was released within 24 h while, in presence of the enzyme, ~ 40% of Dox release was observed in the same time frame. For longer release times, the effect of MMP-2 is more evident and, after 36-48 h, Dox release percentage was roughly two-fold higher in presence of the enzyme. More interestingly, after 48 h, the Dox release from PELGA-Dox NPs was the same with and without enzyme treatment and, in particular, the percentage of released Dox in these conditions is comparable to the percentage of drug released from the untreated PELGA-TAP NP in the same time frame (Figure 1.9 B).

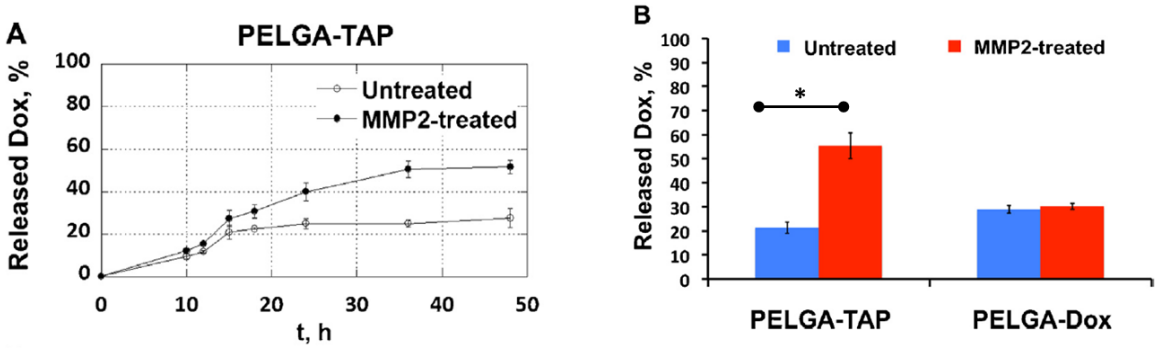

Figure 1.9: ***In vitro*** **Dox release profile from PELGA-TAP NPs at 37°C in presence (black circles) and absence (white circles) of 20 nM MMP-2 enzyme (A); Dox release percentage from PELGA-TAP and PELGA-Dox NPs after 48h incubation with and without MMP-2 enzyme treatment at 37°C (B). Data are reported as mean ± standard de*via*tion (SD).** ***p*** **< 0.05 was considered statistically significant.** ***Reprinted from [4].***

1.3.5 Penetration of Dox within tumour *spheroid matrix upon endogenous MMP-2 cleavage of PELGA-TAP NPs*

In this work, the expression and the enzymatic activity of endogenous MMP-2 secreted by U87-MG and HDF cells were verified. As shown by the results of indirect immunofluorescence analysis presented in Figure 1.10 (A and B), tumour cells express greater levels of MMP-2 protein than healthy cells. Moreover, zymography results

demonstrate that, for U87-MG cell line, a higher amount of secreted MMP-2 enzyme in its activated form was found in cell culture medium (Figure 1.10 C), since MMP-2 are extracellularly-released enzymes [56] [57] [58]. Conversely, the lowest level of secreted MMP-2 was found for HDF cells. In particular, MMP-2 for U87-MG was 8.4 fold higher than HDF cells.

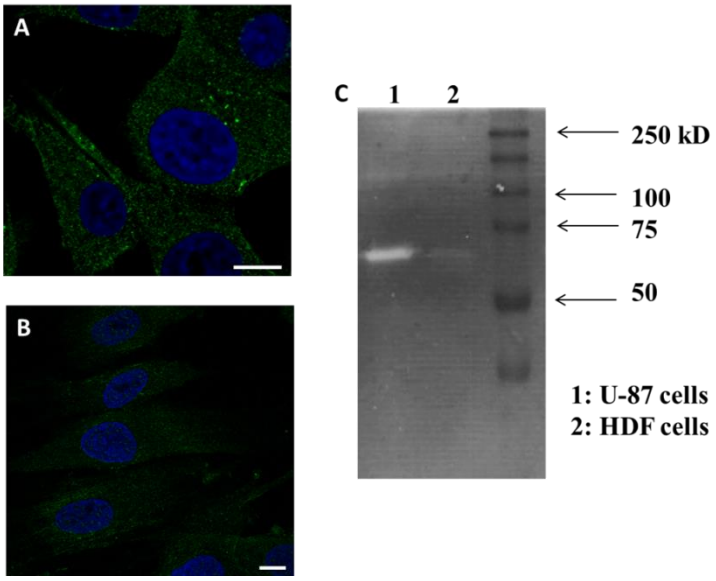

Figure 1.10: MMP-2 expression levels in U87-MG and HDF cells. Indirect immunofluorescence of MMP-2 protein (green) in U87-MG (A) and HDF (B). Blue: DAPI staining of nuclei. Scale bar 10 µm. Gelatin zymography showing the MM2 activity of the two cell types used in this work (C) ***Reprinted from [4].***

Based on these findings, in order to demonstrate the ability of PELGA-TAP NPs to sense the differences in expression levels of endogenous MMP-2 enzyme and, hence, induce Dox release upon specific enzymatic cleavage, U87-MG and HDF cell spheroids were used as *in vitro* models of a tumour and a healthy tissue, respectively. Tumour spheroids were incubated with PELGA-TAP for 24 and 48 h at 37 °C. To further verify the specificity of action of PELGA-TAP NPs, PELGA-Dox NPs (*i.e.*, without the enzyme-sensitive linker) were used as a negative control. At first, the diffusion of free Dox through the spheroid matrix was evaluated by confocal microscopy analysis.

Z-sectioning projection images show the presence of a fluorescence signal within U87-MG tumour spheroids after 24 h exposure to PELGA-TAP NPs (Figure 1.11 A and C). Moreover, spheroid fluorescence was found to be rapidly increasing over time, therefore indicating Dox accumulation within the spheroid bulk and, as a consequence, spheroids tend to disaggregate after 48h of incubation with PELGA-TAP NPs (Figure 1.11 B). On the other hand, a very low fluorescence signal was observed in the case of U87-MG spheroids treated with PELGA-Dox both for 24 and 48 h incubation.

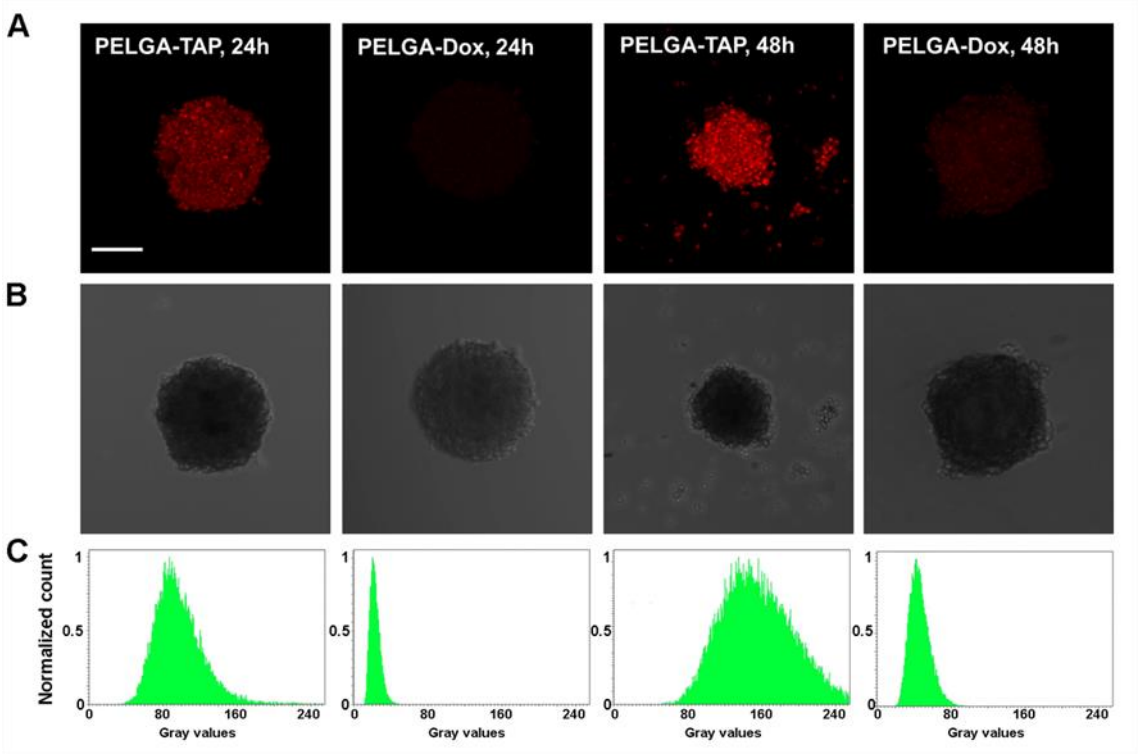

Figure 1.11: Distribution of Dox within U87-MG spheroid matrix upon 24 and 48 h incubation with PELGA-TAP NPs and PELGA-Dox NPs. Maximum projection of z-sectioning confocal images of Dox (red) in U87-MG spheroids (A). Transmitted light images of U87-MG spheroids (B). Fluorescence intensity distribution of Dox diffused into the spheroid matrix (C). The y axis represents normalized pixel counts and the x axis represents the pixel fluorescence intensity expressed as grey scale values (scale range 0–255). Scale bar: 200 µm. *Reprinted from [4].*

More interestingly, HDF spheroids show a lower fluorescence signal than U87-MG spheroids, with a less significant difference in fluorescence intensity between PELGA-TAP and PELGA-Dox NPs treatment (Figure 1.12 A and C) than U87-MG spheroids. Finally, in this case, spheroids do not disaggregate and tend to keep their consistency and shape in time.

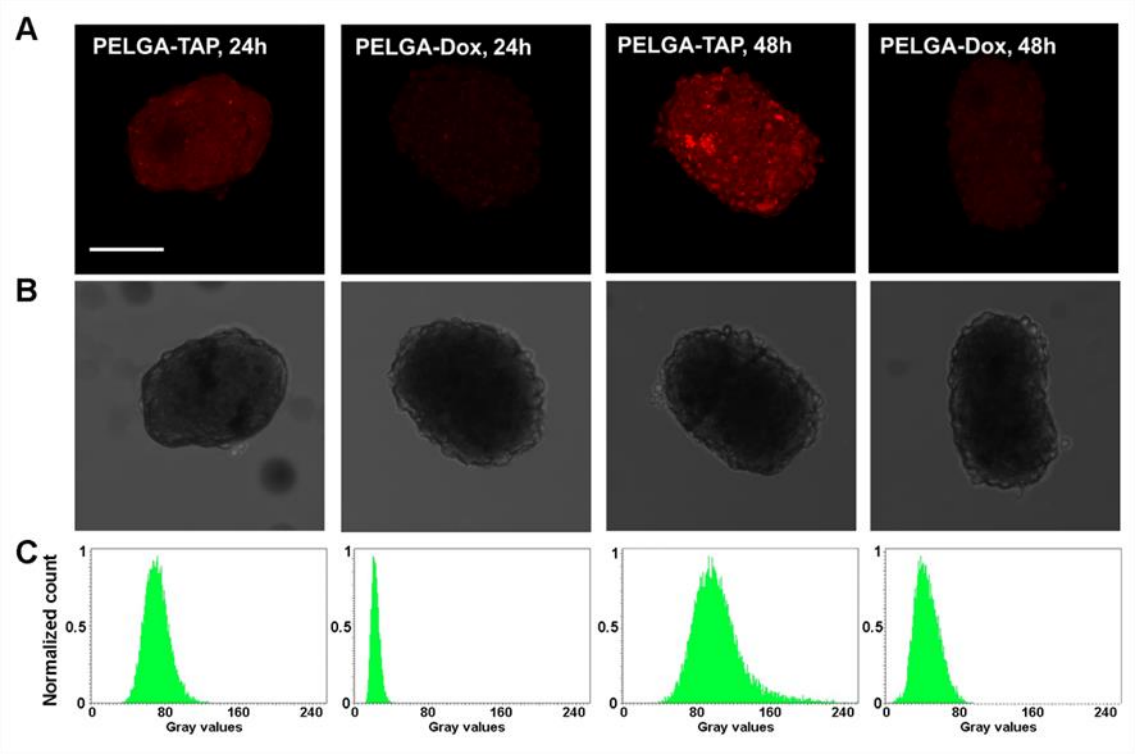

Figure 1.12: Distribution of Dox within HDF spheroid matrix upon 24 and 48 h incubation with PELGA-TAP NPs and PELGA-Dox NPs. Maximum projection of z-sectioning confocal images of Dox (red) in HDF spheroids (A). Transmitted light images of HDF spheroids (B). Fluorescence intensity distribution of Dox diffused into the spheroid matrix (C). The y axis represents normalized pixel counts and the x axis represents the pixel fluorescence intensity expressed as gray scale values (scale range 0 – 255). Scale bar: 200 µm. *Reprinted from [4].*

1.4 Discussions

In this work, we translated the TAP production technology previously published [48] to the fabrication of a biodegradable nanocarrier, based on PELGA copolymer, which consists of two FDA-approved materials, namely PLGA and PEG. The main advantage of this system is the integration of some major drug delivery approaches, such as self-assembly, nanodevice PEGylation, the concept of prodrug and the sensitiveness to endogenous *stimuli*. These characteristics make the produced nanoparticles potentially suitable for anticancer drug delivery driven by a tumour-specific, micro-environmentally induced release mechanism.

The produced PELGA-TAP NPs have a size less than 100 nm, and are basically stable in aqueous media up to two weeks; furthermore, the theoretical drug loading efficiency is of ~20 μg/mg and is significantly higher if compared to emulsion-based NPs which were previously produced by our group [53]. Moreover, the differences between the Dox release profiles in the presence or absence of MMP-2 enzyme clearly indicate the specificity of PELGA-TAP NPs for the enzyme. Indeed, in the absence of the MMP-2 – sensitive peptide linker, the release of Dox is not affected by the presence/absence of enzyme treatment and, furthermore, it is comparable to the released drug fraction from untreated PELGA-TAP NPs. In particular, in the previously mentioned work of our group [48], Dox was tethered to the surface of non-biodegradable polystyrene model NPs and, in that case, drug release was governed solely by the enzymatic cleavage of the prodrug. In another work of our group, the delivery of Dox from PELGA NPs was driven predominantly by the diffusion of the encapsulated drug through the NPs during the hydrolytic degradation of PELGA [53]. The NPs prepared in this study combine both these release mechanisms. Indeed, in the absence of MMP-2 enzyme treatment, the linker between Dox and PELGA is not expected to be cleaved and, therefore, drug release is controlled by the combination of drug diffusion/dissolution and random chain scission at the hydrolytic ester bond of the copolymer [59]. Therefore, it is reasonable to assume that, in the absence of MMP-2-sensitive peptide, the released Dox is predominantly attached to soluble PELGA oligomers. On the contrary, in the presence of the MMP-2-sensitive peptide, the described mechanism is coupled to the enzymatic cleavage. In fact, it is possible to assume that all the Dox is initially complexed to PLGA *via* the MMP-2 – sensitive peptide, while the fraction of unbound drug can be neglected. Therefore, when MMP-2 is present in the

release medium, Dox release is triggered by the enzymatic cleavage of the peptide linker. When MMP-2 initially diffuse toward and into the NPs, it breaks the peptide drug-polymer bond, and contributes to the delivery of the conjugated Dox. Thus, it is possible to conclude that drug release from PELGA-TAP NPs is governed by the complex interplay among the diffusion of MMP-2 and Dox, the kinetics of peptide bond cleavage and the rate of hydrolytic degradation of PELGA.

Based on these findings, in order to demonstrate the ability of PELGA-TAP NPs to sense the differences in expression levels of endogenous MMP-2 enzyme and, hence, to induce Dox release upon specific enzymatic cleavage, U87-MG and HDF cell spheroids were used as 3D *in vitro* models of a tumour and a healthy tissue, respectively. In fact, tumour spheroids represent a relevant *in vitro* model that better resembles the three-dimensional architecture and functionality of the original tissues [60].

Our results demonstrate the specificity of PELGA-TAP NPs action, compared to PELGA-Dox NPs used as a control. Such specificity is elicited by the release of Dox, which is in turn triggered by the enzymatic *stimulus*, as well as by the capability to promote the penetration of the drug within tumour matrix selectively. More interestingly, in agreement with gelatin zymography data, PELGA-TAP NPs are able to 'sense' the differences in the expression levels of endogenous MMP-2 enzyme, therefore contributing to modulate drug penetration within tumour spheroid matrix, accordingly. In particular, fluorescence intensity analysis shows a 40 % increase of Dox accumulation within U87-MG compared to HDF spheroids upon 24 h incubation with PELGA-TAP NPs; after 48 h incubation, this increase is 80 %. Conversely, for PELGA-Dox NPs, the increase of Dox accumulation into U87-MG spheroids is only 25 % compared to HDF and remains constant over time. These results also indicate that PELGA-TAP NPs can promote a prolonged cytotoxic effect taking advantage of the presence of endogenous MMP-2, which is overexpressed in the tumour sites, therefore allowing the massive release of the loaded Dox.

1.5 Conclusions

In this work, a novel formulation of biodegradable PELGA-based NPs for targeted delivery of cytotoxic drugs to tumour tissues, integrating the concepts of prodrug, NPs self–assembly/PEGylation and endogenous *stimuli-responsive* drug release and extracellular drug release was developed. The produced NPs are endowed with a tumour activated prodrug presenting a MMP-2-sensitive peptide sequence as a cleavable domain for the on-demand delivery of Dox in the extracellular environment, taking advantage of physiological changes naturally occurring within tumours. The results presented in this work suggest that the PELGA-TAP NPs can deliver Dox specifically upon enzymatic cleavage and promote drug penetration within 3D tumour spheroids. Moreover, since *in vivo* MMP-2 are extracellularly secreted from the cells [58], Dox release occurs prevalently in the extracellular environment, so drug is mostly presented to the cells in his free form. In this way we combined the advantages of an extracellular drug delivery in proximity of the tumour mass, deriving from the better diffusion properties of the drug itself when compared to the nanoparticles [24], with the need to carry the drug safely in the body and allow its release only in the site of interest, in order to avoid, or at least reduce, the side effects related to the systemic delivery of the drugs.

Therefore, the proposed PELGA-TAP NPs are able to merge the biodegradability/biocompatibility of PELGA with active mechanisms of Dox release and tumour penetration. The clear comprehension of how PELGA-TAP NPs may translate into actual therapeutic effects is still unknown and deserves further investigation. Nevertheless, since the presented NPs are able to release their cargo in presence of endogenous *stimuli* that come from the very nature of the tumour microenvironment, these could be tested on more complex *in vitro* tissue equivalents that better recapitulate tumour architecture, to further assess their efficacy as drug delivery systems. In the light of these considerations, the produced NPs hold promise as a useful tool to improve therapeutic efficacy of the conjugated drug payload.

Acknowledgments

The authors thank Dr. Manlio Colella and Dr. Valentina Mollo for their technical assistance in SEM and Cryo-TEM analyses and Dr. Vincenzo Lettera for his helpful suggestions on zymography analysis.

Chapter.2 **3D tumour microtissues as *in vitro* testing platform for MMP-2-responsive nanoparticles**

ABSTRACT

Therapeutic approaches based on nanomedicine garnered great attention in cancer research and increased the need of *in vitro* biological models that better mimic the *in vivo* conditions in order to more accurately predict the therapeutic efficacy of these nanocarriers. In this work, a new 3D breast cancer model is presented, based on the microtissue approach developed by *Brancato et al.* [5]. This 3D model recapitulate the complexity of the tumour microenvironment along with tumour architecture and was used as drug screening platform to further validate a recent formulation of endogenous metallo-proteinases 2 (MMP-2) responsive nanoparticles (NPs) proposed by *Cantisani et al*. [4]. The 3D cancer model was developed using human breast adenocarcinoma cells and cancer-associated fibroblasts embedded in their own ECM, thus showing several features of an *in vivo* tumour, such as the MMP-2 overexpression. The results of cell viability test show that drug release only occurs in tumour microtissues, when treated with the MMP-2 responsive NPs*.

KEYWORDS: MMP-2 responsive drug delivery, nanoparticles (NPs), microtissues (μTPs), tumour breast.

*The work described in this Chapter is part of a published manuscript: V. Brancato[§], F. Gioiella[§], **M. Profeta**, G. Imparato, D. Guarnieri, F. Urciuolo, et al., "3D tumour microtissues as an *in vitro* testing platform for microenvironmentally-triggered drug delivery systems", *Acta Biomaterialia*, **2017**.

([§]) These authors equally contributed to the work.

2.1 Introduction

The controlled-delivery of chemotherapeutics using NPs is the most promising tools that nanomedicine has in the war against cancer, since drugs are activated or released specifically in tumour tissue, maximizing their effectiveness as well as minimizing their side effects [61] [62] [63]. Tumour microenvironment (TME) has a crucial role in cancer progression and is characterized by several abnormalities such as acidic pH, altered redox potential and up-regulated proteins, which can be exploited as targets to design appropriate *stimuli-responsive* nanoparticles [63] [64] [65] [66]. The *stimuli-responsive* nanocarriers (SRNs) are specialized nano-sized active delivery vehicles that evolve with an external signal and are equipped with "load-and-release" modalities within their constituting units [1]. An array of manifold enzymes, such as proteases, which are expressed differentially and are either intra or extracellular presented by normal and malignant cells, can be used, among others, as biochemical triggers.

In the light of these considerations, a smart approach in NPs design may be the one that benefits from the MMPs over-expression in tumour sites, in order to produce a *stimuli-responsive* nanocarrier, allowing a site specific drug release.

To this aim, *Cantisani et al*. [4] proposed the use of a novel nanocarrier able to carry safely doxorubicin in tumour tissues, and to respond to MMP-2 enzyme. The produced NPs are made up of a biodegradable poly(D,L-lactic-co-glycolic acid) (PLGA) – block – PEG copolymer (namely PELGA), blended with a TAP composed by a MMP-2-sensitive peptide bound to doxorubicin (Dox) at the C-terminus and to PLGA molecule at the N-terminus. These NPs are named PELGA-TAP NPs. The presence of the MMP-2 enzyme *in situ*, leads to the disruption of the bond between the peptide and the Dox, with the consequent diffusion of the drug; this mechanism allows drug delivery only in presence of endogenous *stimuli* that comes from the very nature of the tumour tissue itself. Furthermore, the same NPs were prepared without the presence of the peptide sequence, as negative control and are named PELGA-Dox (Figure 2.1).

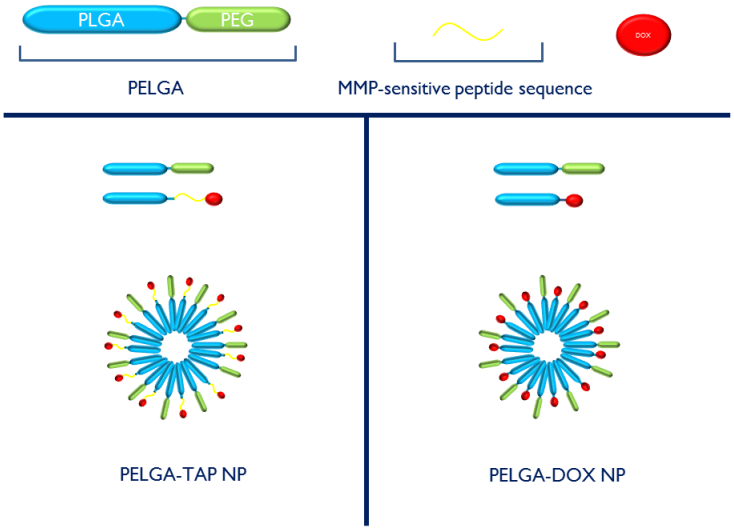

Figure 2.1: Schematic representation of PELGA-TAP and PELGA-Dox NP production. Figure not in scale. ***Reprinted from [6].***

It is well recognized that TME is populated by different kinds of cells (*i.e.* epithelial cells, normal and cancer-activated fibroblasts, endothelial cells) [67] that are embedded in the extracellular matrix (ECM) and nourished by the vascular network [68]. However the efficiency and selectivity of new drugs are often tested in 2D systems, in which cancer cells seeded on Petri dish do not experience the real microenvironment they find *in vivo*, where the stromal and cancer cells interact impairing the drug delivery or its functionality. This is extremely costly and time-consuming during preclinical studies. Since tumour stroma affects the sensitivity of tumour cells to drug treatment [69], it is crucial to have *in vitro* models that faithfully replicate the features of cancer microenvironment *in vivo* and, at the same time, are highly reproducible, robust, easy to use and suitable for high-throughput screening [70] [71] [72] [73]. 3D spheroid models [74] partially resemble some features of *in vivo* tumours, such as three-dimensional architecture, cell-cell interaction and hypoxia; they are currently used as tumour tissue-like *in vitro* models for testing anticancer therapeutics. However, they fail in faithfully reproducing the TME mainly because of the lack of an organized ECM capable to replicate both structural and morphological changes occurring during pathologic events [5]. Recently, *Brancato et al.* [5] proposed a new model of *in vitro* stroma microtissue characterized by a cell instructive microenvironment able to recapitulate the *in vivo* characteristics of healthy and tumour stroma tissues [75]. Here we produce and characterize, for the first time, a model of breast cancer by co-culturing epithelial breast cancer cells (MCF7) and cancer-associated fibroblasts (CAF) on gelatin microscaffolds, in spinner flask bioreactors. The resulting 3D breast tumour microtissue, in

contrast to the spheroid models, present a heterotypic cell population embedded in its own ECM. We used this model to test the above mentioned nanoparticles.

The NPs were also tested on a 3D healthy tissue composed of normal fibroblasts (NF) and epithelial breast cell lines (MCF10) to demonstrate their significant selectivity against tumour target.

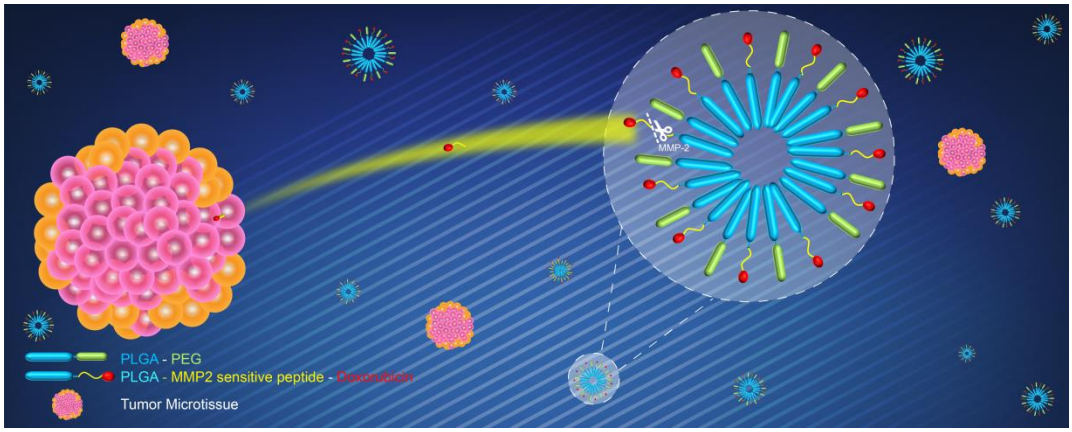

Figure 2.2: Graphical summary of the work. ***Reprinted from [6].***

2.2 Materials and Methods

2.2.1 Materials

Equimolar uncapped poly(D,L-lactide-co-glycolide) (PLGA) (Resomer RG502H, Mw 12000 Da) was purchased from Boehringer Ingelheim (Ingelheim, Germany). Doxorubicin hydrochloride (Dox, purity > 99%) was purchased from Discovery Fine Chemicals (UK). Polyethylene Glycol (PEG, Mw 1500 Da), N,N-diisopropylethylamine (DIPEA), O-benzotriazole-N,N,N', N'–tetramethyluronium–hexafluoro–phosphate (HBTU), Ethyl cyano(hydroxyimino)acetate (Oxyma Pure), anhydrous N,N–dimethyl-formamide (DMF), N,N'–diisopropylcarbodiimide (DIC), N,N'-Dicyclohexylcarbodiimide (DCC), 4-(dimethylamino) pyridine (DMAP), dichloromethane (DCM), piperidine, trifluoroacetic acid (TFA), acetonitrile (ACN), Diethyl ether, HPLC– grade water and all buffer solutions were purchased from Sigma-Aldrich (USA). All 9-fluorenyl methoxy carbonyl (Fmoc)–aminoacids were purchased from IRIS Biotech GmbH (Germany). Dialysis bags (MWCO 6-8 kDa) were obtained from Spectrum Laboratories, Inc. (The Netherlands), while distilled and deionized water (18MΩ resistance) were from Millipore (USA).

2.2.2 Synthesis of copolymers and conjugates

PLGA-PEG copolymer (namely PELGA) was synthesized *via* a coupling reaction between PLGA and PEG, optimizing a previously reported procedure [4]. Briefly, 1 eq of PLGA, 4 eq of PEG, 0.4 eq DMAP and 2 eq of DCC were dissolved in 10 mL of anhydrous DCM. After the reaction, the residual DCC was changed into dicyclohexylcarbodiurea (DCU) by adding bidistilled water. Then DCM was evaporated and the mixture was dissolved in 10 mL of DMSO, filtrated and dialyzed (MWCO 6-8 kDa) for 1 day against ACN and for 2 days against water. Pure product was recovered after lyophilization and analyzed by Nuclear Magnetic Resonance (NMR) spectroscopy. PLGA-Dox and PLGA-TAP copolymers were synthesized according to a previously reported method with slight modifications [4]. Briefly, the MMP-2-sensitive Fmoc–Gly–Pro–Leu–Gly–Ile–Ala–Gly–Gln–COOH peptide was synthesized using standard solid phase Fmoc method [48] and verified by analytical LC-MS. Then, the peptide–Dox conjugates were synthesized by a standard coupling procedure, using HBTU as coupling reagent. Peptides

(1 eq), HBTU (1 eq), Oxyma Pure (1 eq), DIPEA (2 eq), and Dox (1.5 eq) were dissolved in anhydrous DMF. The reacting mixture was continuously stirred overnight and the reaction products were verified by analytical LC-MS. After the coupling reaction, the mixture was precipitated in cold diethyl ether to remove undesired reaction products and the excess of unreacted doxorubicin. In order to remove the Fmoc group, Fmoc-MMP-2-Dox was dissolved in 1% piperidine/DMF solution for 5 min and then precipitated again in cold diethyl ether. The purity of the reaction product was asserted by LC-MS and the residue was dissolved in a 30/70 (v/v) acetonitrile (ACN)/water solution containing 0.1 % (v/v) TFA and purified by RP-HPLC. Finally, the PLGA-peptide-Dox (TAP) conjugate was synthesized using a standard HBTU coupling procedure. Briefly, PLGA (1 eq), HBTU (5 eq), Oxyma Pure (5 eq), DIPEA (10 eq), and peptide-Dox conjugates (1.2 eq) were dissolved in anhydrous DMSO and led to react overnight. The copolymer was purified removing the unreacted reagents using dialysis bags (MWCO 6–8 kDa) and lyophilized. Furthermore, as a negative control, to evaluate specific MMP-2 enzyme cleavage of the pro-drug, a PLGA-Dox conjugate without the MMP-sensitive peptide was synthesized and purified as reported above. In particular, PLGA (1 eq), HBTU (1 eq), DIPEA (2 eq) and Dox (1.5 eq) were used. Final products were analyzed by ^{1}H-NMR spectroscopy using a combination of 1D PROTON and DOSY experiments. NMR spectra were recorded using an Agilent 600MHz (14 Tesla) spectrometer equipped with a DD2 console and an OneNMR HX probe. PLGA-PEG, PLGA-Dox and PLGA-Peptide-Dox samples (1 mg) were dissolved in 600 µl of 99.9% deuterated DMSO (Sigma–Aldrich).^{1}H 1D spectra were recorded at 300 K using 4, 1024 and 2048 scans respectively to obtain a good signal-to-noise ratio for each sample. A double saturation PRESAT pulse sequence was used to reduce residual peaks of DMSO and water at 2.5 and 3.3 ppm, respectively. Spectra were transformed and analyzed using VNMRJ4 software. Chemical shift scale was referenced to the solvent residual peak signal.

2.2.3 NP preparation

PELGA-TAP NP were produced starting from a well-established procedure [4]. Briefly, 1 mg of PELGA and 1 mg of TAP were dissolved in 500 µl of acetone. Afterwards, the solution was added dropwise with a syringe pump into 12.5 ml of distilled water under magnetic stirring. The organic solvent was then evaporated for 3 h and the obtained NP

dispersion sterilized with a 0.22 μm membrane filter. Finally, the volume of the solution was reduced to 1 ml by using Amicon Ultra-4 10 kDa centrifuge tube (Millipore), to have a final NP concentration of 2 mg/ml. Control NP (*i.e.* without the MMP-sensitive linker) were prepared with the same technique using 1 mg of PLGA-Dox and 1 mg of PELGA.

2.2.4 NP size and morphology

The NP mean size, size distribution and Polydispersity Index (PDI) were determined by Dynamic Light Scattering (DLS) (ZetaSizer Nano ZS, Malvern Instruments, Malvern, UK) on a 0.1 mg/ml suspension of NP in water. Results were averaged on all NP batches used in this work.

NP morphology was analysed by Cryogenic Transmission Electron Microscopy (Cryo-TEM). Cryo-TEM samples were vitrified with FEI Vitrobot Mk IV in a saturated water vapour environment. Sample volumes of 3 μl were placed on 200 mesh Quantifoil grids and the excess sample was blotted away with filter paper. Blot time and drain time were both 1 s. After blotting, the grids were plunged into liquid propane that was cooled with liquid nitrogen surrounding the propane vessel. Imaging was performed with TEM TECNAI G2 equipment operating at 200 kV in low dose mode and acquired with an Eagle 2HS camera.

2.2.5 Cell culture

Normal human mammary fibroblasts (NF) and cancer associated fibroblasts (CAF) were provided by the group of prof. Bussolino (IRCCS Institute of Candiolo, Turin, Italy) following the procedures previously described [76] and stable transfected with pLVX-DsRed-express2-N1 (λex 554nm, λem 591nm) viral vector (Clontech, USA). Cells were sub-cultured onto 150 mm Petri dishes in DMEM-HG (Dulbecco's Modified Eagle Medium-High Glucose), supplemented with 10b% fetal bovine serum, 100 μg/ml L-glutamine and 100 U/ml penicillin / streptomycin.

Human epithelial cell lines (MCF10) from ATCC and human breast adenocarcinoma cells (MCF7) kindly donated by Daidone's group, were sub-cultured onto 150 mm Petri dishes in MEBM (Mammary Epithelial basal medium, Lonza) and RPMI-1640 (Roswell Park Memorial Institute) supplemented with 10b% fetal bovine serum, 100 μg/ml L-

glutamine and 100 U/ml penicillin / streptomycin, respectively. Cells were maintained at 37 °C in humidified atmosphere containing 5 % CO2.

2.2.6 Microbeads production

Gelatin porous microbeads (GPMs) were prepared according to a modified double emulsion protocol (O/W/O) previously developed by our group. For further detail see ref. [77].

2.2.7 Microtissue dynamic culture

Before using, dry GPMs were sterilized in absolute ethanol 24 h on a rotating plate. Then, GPMs were washed twice in sterile phosphate-buffered saline (PBS) without calcium and magnesium solution. Finally, before cell seeding, PBS was replaced by fresh culture medium. For all experiments 100 ml siliconized spinner flask (Integra) were used. The 3D healthy and tumour microtissue named NF/MCF10- and CAF/MCF7-μTP, respectively, were produced as follows. Firstly, we performed a homotypic culture by seeding fibroblast cells (NF or CAF) on GPMs and after six days epithelial cells (MCF10 or MCF7) were added on fibroblast-seeded GPMs. In particular, homotypic cultures were performed by using 50 mg of GPMs and 7.5 x 105 healthy (NF) or activated fibroblasts (CAF), in a ratio of 30 cells for GMP. A stirring regime (30 min at 0 rpm, 5 min at 30 rpm) for 6 h was used, while continuous intermittent stirring at 30 rpm was used until the end of the culture (12 days). Then, at day 6 of fibroblast culture, healthy (MCF10) and tumour epithelial cells (MCF7) were added into spinner flasks with NF and CAF, respectively, at a ratio 1:3. The ratio was calculated considering the number of fibroblast for GMP at day 6. Medium was changed on the first day and every 3 days until the end of the experiments. To stimulate the production of collagen, 50 μg/ml of ascorbic acid were added, from day 2 of the dynamic culture [78].

2.2.8 μTPs characterization

Cell growth on the GPMs was monitored at day 1, 6, 7 and 12 of culture, collecting about 1 ml of the NF/MCF10- and the CAF/MCF7-μTP suspension from the spinner flask.

Masson's trichrome (Sigma Aldrich) staining was performed, according to standard protocol, to observe the morphological features of the μTP. Images were acquired using a light microscope (Olympus, BX53).

Confocal and Second Harmonic Generation (SHG) images were acquired to morphologically characterize the μTPs. NF/MCF10- and the CAF/MCF7-μTP were fixed with 4% paraformaldehyde for 20 min and washed three times with PBS. After that, cell nuclei were stained using DAPI, (Sigma-Aldrich λex = 700 nm and λem = 425 ± 25 nm). NF and CAF cells were imaged using the following parameters: λex = 543 nm and λem = 590 ± 60 nm. A 40X water objective was used. Moreover, two-photon excited fluorescence was used to induce SHG and obtain high-resolution images of unstained collagen structures in μTP's ECM (λex = 840 nm, λem = 420 ± 5 nm).

To quantitatively assess the collagen-related changes in the architecture, Grey-Level Co-occurrence Matrix (GLCM) texture analysis was performed [5] [75].

Further details concerning this section can be found in ref. [6].

2.2.9 MMP-2-expression in tumour and healthy 3D-μTP

In order to quantitatively and qualitatively verify MMP-2 expression in tumour and healthy μTPs, a set of analysis were performed.

First of all, total RNA extraction of homogenized μTP was quantitatively obtained by means of real time PCR. RNA was extracted using High pure RNA isolation kit (Roche Diagnostics; Milan, Italy). An RNA quality check, including concentration and purity, was performed with a Bio photometer DNA RNA UV spectrophotometer (Eppendorf). All experiments were performed in triplicate.

Indirect immunofluorescence of the MMP-2 enzyme was also performed. In this case, formalin-fixed and paraffin embedded NF/MCF10- and CAF/MCF7-μTP were unmasked by heat antigen retrieval protocol; washed with PBS containing 0.2 % Triton X-100, blocked with FBS and 5 % BSA solution and incubated with primary antibody MMP-2 (1:200, Abcam UK). Before closing the slices with glycerol solution, secondary antibody incubation and DAPI staining were performed. Fluorescent images were acquired by using a multichanneled Leica TCS SP5 II, and then were analysed for semi-quantitative evaluation with ImageJ. In more detail, the amount of signal was divided by the total number of cells (previously obtained by counting their nuclei) in each image [79] [80].

Finally, gelatin zymography was performed for both the NF/MCF10- and the CAF/MCF7-μTP culture surnatants as follows: gel (SDS–PAGE, 10 %) was co-polymerized with gelatin (0.1 %) (Sigma-Aldrich). Electrophoresis was carried out using the minigel lab apparatus Mini Protean 3 (Biorad) at a constant voltage of 150 V until the dye reached the bottom of the gel. Following electrophoresis, the gel was washed in renaturation buffer (2.5 % Triton X-100 in 50 mm Tris–HCl, pH 7.5) for 1 h in an orbital shaker. Then it was incubated for 18 h at 37 °C in incubation buffer (0.15 m NaCl, 10 mm CaCl2, 0.02 % NaN_3 in 50 mm Tris–HCl pH 7.5). The gel was then stained with Coomassie blue and destained with 30% methanol and 10 % acetic acid. Areas of enzymatic activity appeared as clear bands over the dark background. Finally, the degree of gelatin digestion was quantified using Image J software and the image was digitally inverted, so that the integration of bands was reported as positive values. We reported the pixel intensity of the area of each gelatin-digested band.

Further details concerning this section can be found in ref. [6].

2.2.10 μTPs NPs treatment

In order to have the same cell density, the NF/MCF10- and the CAF/MCF7-μTP were transferred into ultra-low attachment 96-well round-bottomed plates (Corning, USA). Both μTP were treated with medium only, as positive control, with PELGA-TAP and with PELGA-Dox NPs at a final Dox concentration of 4 and 8 μg/ml of Dox for 48 and 72 h at 37 °C in humidified atmosphere containing 5% CO2. After treatment, NF/MCF10 and the CAF/MCF7-μTP were washed three times with PBS.

2.2.11 μTPs confocal imaging

After treatment, all types of μTP used in the experiment were fixed in 4 % paraformaldehyde in PBS for 20 min. Cell nuclei were stained with 1 μg/ml of DAPI (Sigma-Aldrich, λex = 700 nm and λem = 425 ± 25 nm). Dox fluorescence was observed under a confocal microscope (Leica) with excitation at 488 nm and emission 515 ± 15 nm, using a 40X/1.10 water objective.

2.2.12 Cytotoxicity assay

After treatment, MMT assay was performed to detect cell viability according to manufacturer's instructions. Briefly, 20 μL of 3-(4,5-dimethylthiazol-2-yl) - 2,5 - diphenyltetrazolium bromide (MTT) solution (5 mg/ml) were added to each well, and the plates were incubated for another 4 h, allowing the viable cells to reduce the yellow MTT into dark-blue formazan crystals, which were dissolved into 100 μL of dimethyl sulfoxide (DMSO). The absorbance of individual wells was measured at 470 nm using a microplate reader (Enspire Multimode Plate Reader PerkinElmer). All experiments were performed in triplicates.

2.2.13 Statistical analysis

Differences between two or more groups were evaluated (p-value < 0.05) using one-way analysis of variance (ANOVA).

2.3 Results

2.3.1 Synthesis of copolymers and conjugates

NPs precursors were prepared through ester or amide linkage to the carboxylic group of PLGA, optimizing a previously reported synthesis [49]. In particular, Oxima Pure® was used as additive instead of 1-hydroxybenzotriazole (HOBt), both in peptide synthesis and in conjugation coupling reactions, since Oxima Pure is reported to be superior in terms of suppression of racemization, coupling efficiency and safety, when compared to HOBt [81] [82].

A detailed chemical characterization of PELGA, PLGA-Dox, PLGA-TAP and its precursors by means of LC-MS and ^{1}H-NMR spectroscopy analysis is reported below. In particular, ^{1}H-1D NMR and DOSY spectra confirm structure of all the conjugates and show that it was not found a significant amount of unreacted reagents for all the samples.

PELGA Copolymer

^{1}H-1D-NMR spectrum of PELGA copolymer is reported in Figure 2.3 A. Characteristic peaks of PEG and PLGA can be identified: PLA peaks in the region between 5.28 and 5.14 ppm and at 1.59 ppm; PGA peaks in the region between 4.96 and 4.84 ppm; PEG peak at 3.49 ppm; DMSO solvent peak at 2.50 ppm and water residual peak at 3.33 ppm.

Figure 2.3 B shows DOSY spectrum of PELGA. From this picture is possible to see that PLGA and PEG peaks have very similar diffusion coefficient (*see red line*) proofing that they are covalently bounded, since they diffuse as a single blocks with the same diffusion coefficient.

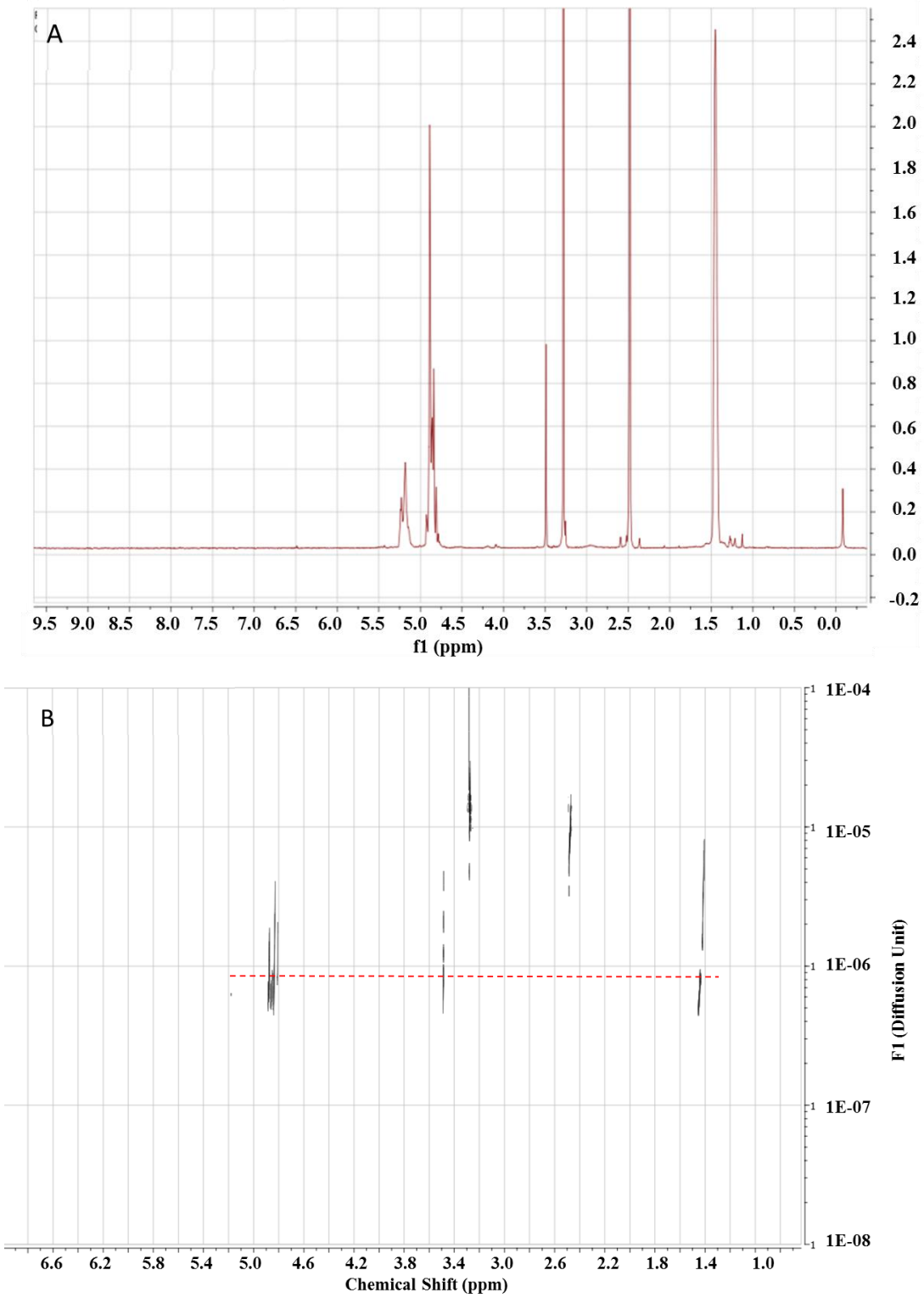

Figure 2.3: 1H-1D-NMR (A) and DOSY (B) spectra of PELGA in DMSO. *Reprinted from [6].*

PLGA-conjugates

Figure 2.4 show mass spectra of Peptide-Dox synthesis steps.

MMP-2-sensitive peptide was obtained with a good yield. The presence of the crude peptides was verified by analytical LC-MS (Figure 2.4 A).

Regarding peptide-Dox synthesis, pure Fmoc-peptides, with free carboxylic C-terminus, were conjugated to Dox by amide bond formation (Figure 2.4 B) and purified with HPLC after Fmoc deprotection (Figure 2.4 C). The presence of the conjugates was confirmed by analytical LC-MS.

In more detail, Figure 2.4 A represent MS for Fmoc-Peptide and the peaks of interest are $[M+H]^+$: 934 m/z and $[M+2H]^{2+}$: 467 m/z;

Figure 2.4 B show MS for Fmoc-Peptide-Dox and the peaks of interest are $[M+H]^+$: 1459 m/z, $[M+Na]^+$: 1481 m/z and 1045 and 397 which are the first and the second fragmentation of the conjugate, respectively.

Finally, Figure 2.4 C depicts MS for Peptide-Dox and the peaks of interests are $[M+H]^+$: 1237 m/z and 823 and 397 which are the first and the second fragmentation of the conjugate, respectively.

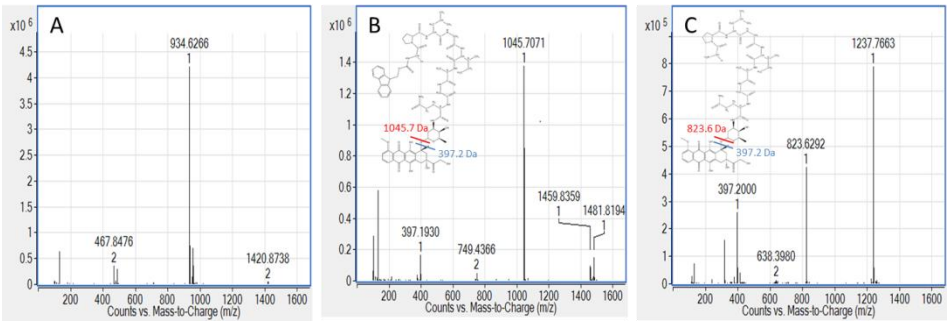

Figure 2.4: Mass spectra of TAP synthesis steps. Inset (A) shows Fmoc–Peptide mass spectra [M+H]+: 934.6 Da; Inset (B) shows Fmoc-Peptide-Dox mass spectra [M+H]+: 1459.8 Da, [M+Na]+: 1481.8 Da; Inset (C) shows Peptide-Dox mass spectra [M+H]+: 1237.8 Da. *Reprinted from [6].*

Peptide-Dox conjugates or free Dox were linked to PLGA by amide bond formation, leading to the formation of PLGA-Peptide-Dox (namely PLGA-TAP) and PLGA-Dox, respectively. The reaction products were dialyzed against DMSO and water to remove excess of reagents. PLGA-Dox and PLGA-Peptide-Dox synthesis were verified using ^{1}H-NMR spectroscopy and DOSY experiments. In Figure 2.5, ^{1}H-1D NMR spectra of PLGA-Dox (A) and PLGA-Peptide-Dox (B) in DMSO are reported. Assignments of PELGA-Dox and PLGA-TAP peaks are summarized below.

PLGA-Dox ^{1}H-NMR (600 MHz, DMSO): δ (ppm) 8.40-7.60 (doxorubicin aromatic protons); 5.28-5.14 (CH, PLGA); 4.96-4.84 (CH_2, PLGA)

PLGA-TAP ^{1}H-NMR (600 MHz, DMSO): δ (ppm) 8.50-6.00 (peptide amide backbone); 5.28-5.14 (CH, PLGA); 4.96-4.84 (CH_2, PLGA)

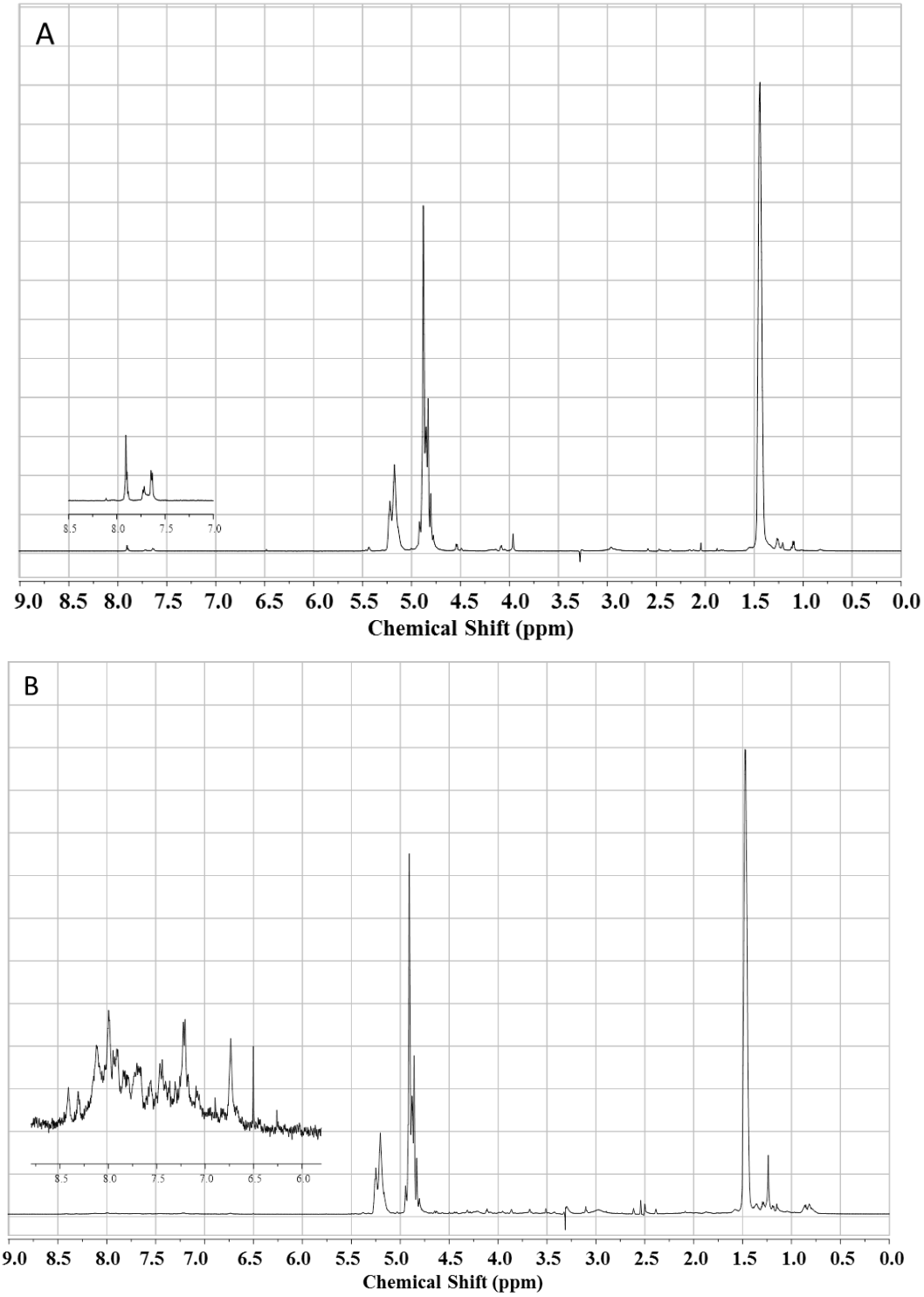

Figure 2.5: 1H-1D-NMR spectrum of PLGA-Dox (A) and PLGA-Peptide-Dox (B) in DMSO. PLGA: δ=1.45 ppm, s (CH3); δ=4.85 ppm, m (CH2); δ=5.17 ppm and δ=5.22 ppm, m (CH). Expansions show aromatic protons of doxorubicin (A) and peptide bonds signals (B), respectively. *Reprinted from [6].*

The theoretical amount of drug loaded by the NP for mg of polymer was roughly ~20 µg/mg. It was calculated considering the initial mass of co-polymers (PLGA-Dox or PLGA-TAP) used during nanoparticle preparation. This data was confirmed by the integration of doxorubicin aromatic proton and PLGA peaks which indicates a polymer/drug ratio of 1:1. Moreover, DOSY spectra of PLGA-Dox (Figure 2.6 A) and PLGA-TAP (Figure 2.6 B) did not show the presence of significant amounts of free TAP or doxorubicin.

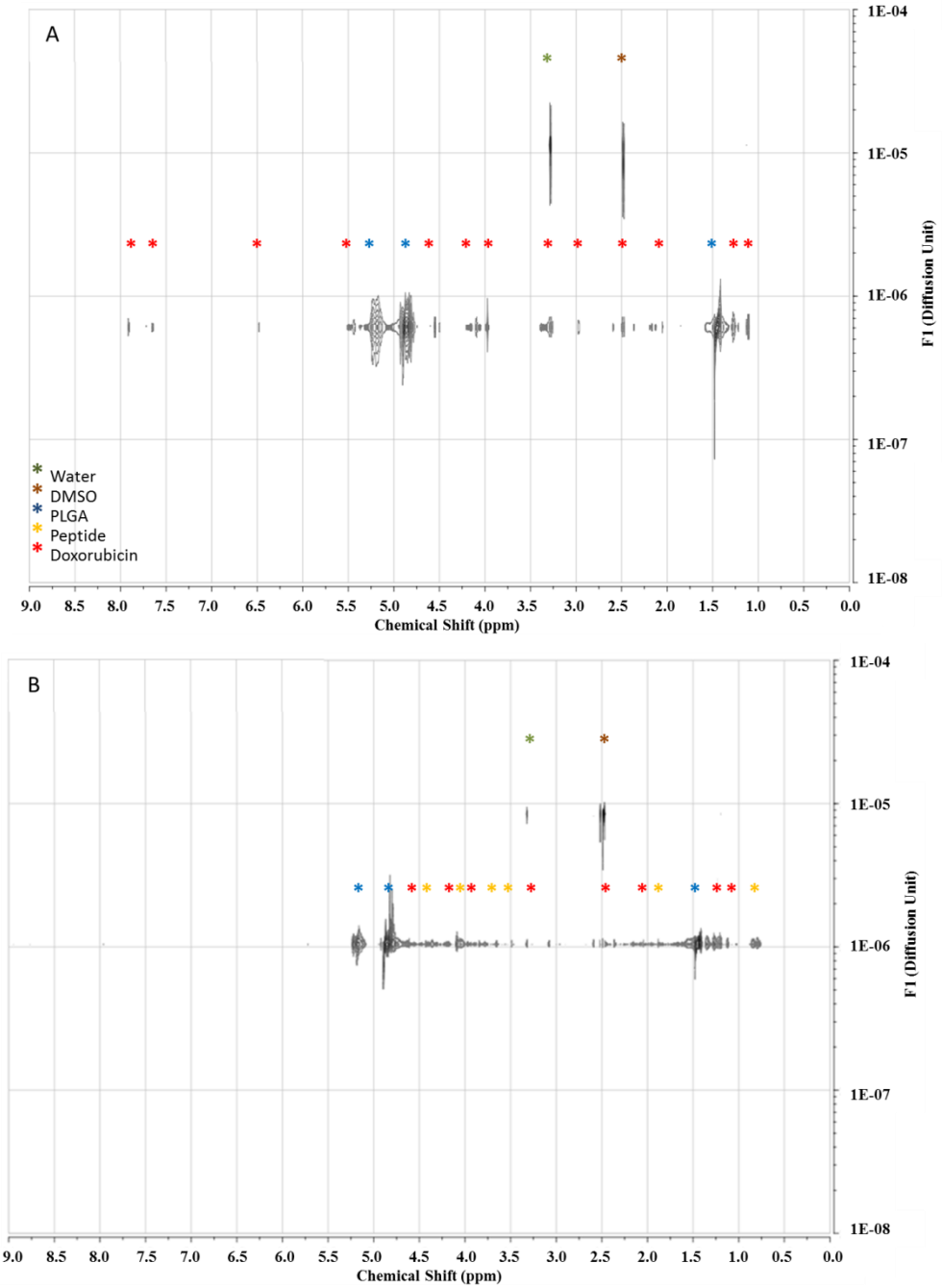

Figure 2.6: DOSY spectra of PLGA-Dox (A) and PLGA-Peptide-Dox (B) in DMSO. Diffusion axes are labeled in cm^2 s^{-1}. *Reprinted from [6].*

2.3.2 Nanoparticle characterization

PLGA-TAP and PLGA-Dox were mixed with PELGA copolymer in acetone for the production of NPs, according to the procedure described above.

Any batch of the produced NPs used in this work was characterized in terms of size, ζ-potential, stability and morphology.

As shown in Table 2.1, DLS measurements indicate that the diameter of both NP formulations was below 100 nm, with a PDI ≈ 0.2, thus validating NP preparation procedure [4].

Formulation	NP mean diameter (nm)	Polydispersity Index (PDI)
PELGA-TAP	95.16 ± 6.53	0.23 ± 0.03
PELGA-Dox	78.93 ± 6.76	0.17 ± 0.03

Table 2.1: Formulation, mean size and PDI of PELGA-TAP and PELGA-Dox NP. Data are reported as mean ± SD. ***Reprinted from [6].***

Cryo-TEM images in Figure 2.7 further confirm that PELGA-TAP NP are spherical and monodispersed, with a regular shape.

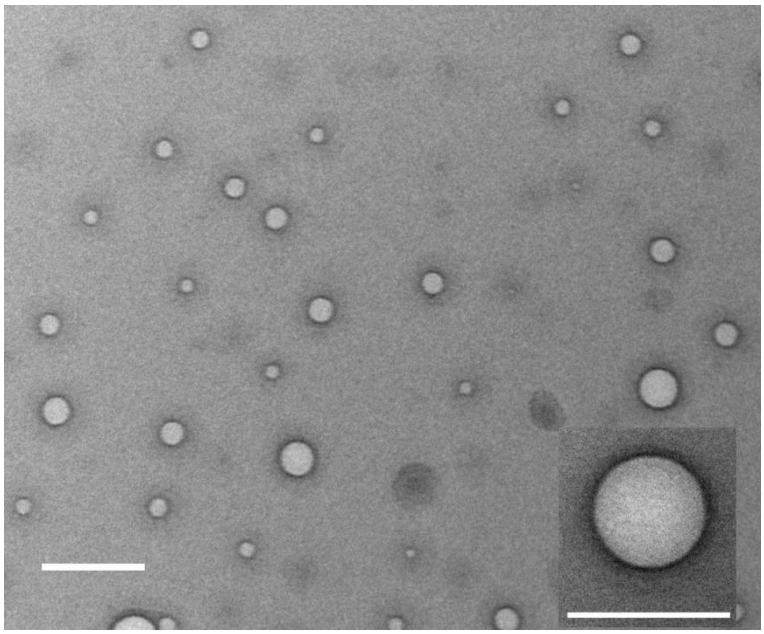

Figure 2.7: Cryo-TEM of PELGA-TAP NP. The inset shows a single NP at higher magnification, (scale bar: 100 nm). ***Reprinted from [6].***

In Chapter.1- paragraph *"Doxorubicin in vitro release kinetics from PELGA-TAP nanoparticles"*, we demonstrated that PELGA-TAP NP were able to release doxorubicin upon specific cleavage of the sensitive peptide linker by free MMP-2 enzyme *in vitro* [4]. Results showed that almost 60 % of Dox was released within 48 h incubation with 20 nM MMP-2 enzyme at 37 °C, compared to about 20 % in absence of the enzyme. Conversely, control PELGA-Dox NP, that lack of the MMP-2-sensitive peptide linker, did not show any difference in Dox release profiles in presence or absence of the enzyme. In particular, the percentage of released Dox in these conditions was comparable to the percentage of drug released from untreated PELGA-TAP NP.

2.3.3 3D human breast μTP characterization

In this work, 3D tumour models composed of epithelial and stromal cells embedded in their own ECM were produced, characterized and then used as drug screening platform for MMP-2-responsive NPs. Figure 2.8 A and B illustrate CAF/MCF7-μTP evolution during 12 days of culture in terms of cell number per μTP unit. At the same time, a 3D healthy tissues (NF/MCF10-μTPs) were used as a control (Figure 2.8 B). Results show that NF and CAF, starting from the same number of 36 ± 5.57 cells for μTP, reached after 12 days of culture the number of 870 ± 129 and 1635 ± 136 cells for μTP, respectively. Regarding the epithelial cells, at day 7 the number of MCF10 was 113 ± 45 cells for μTP while the number of MCF7 was 248 ± 20 cells for μTP. At the end of the culture, we found 561 ± 113 MCF10 for μTP and 2200 ± 306 MCF7 for μTP. The ability of stromal cells in μTP configuration to produce a dense matrix structure was demonstrated by immunostaining and SHG analysis (Figure 2.8 C-H). Moreover, Figure 2.8 C and D reported the histological sections stained by Masson's trichrome of 3D normal and tumour μTP, respectively. From histological images it was possible to distinguish the purple signal due to cell staining and the blue signal of the endogenous ECM. Figure 2.8 E and F show confocal and multiphoton images of the CAF/MCF7- and the NF/MCF10-μTP, respectively. In particular, the fluorescence signal of cell nuclei (both epithelial and stromal cells, in blue), the fluorescence of CAF and NF cells due to viral transfection (in red) and the SHG signal (in grey scale) were detected. As shown in Figure 2.8 G, the correlation curve of the NF/MCF10-μTP decayed faster than the CAF/MCF7 one. This

phenomenon is clearer when considering the correlation length (λ) values (Figure 2.8 H). In particular, the λ was greater for the CAF/MCF7-µTP than the NF/MCF10-µTP, validating the finer structure of the latter compared to the tumour µTP.

Further details concerning this section can be found in ref. [6].

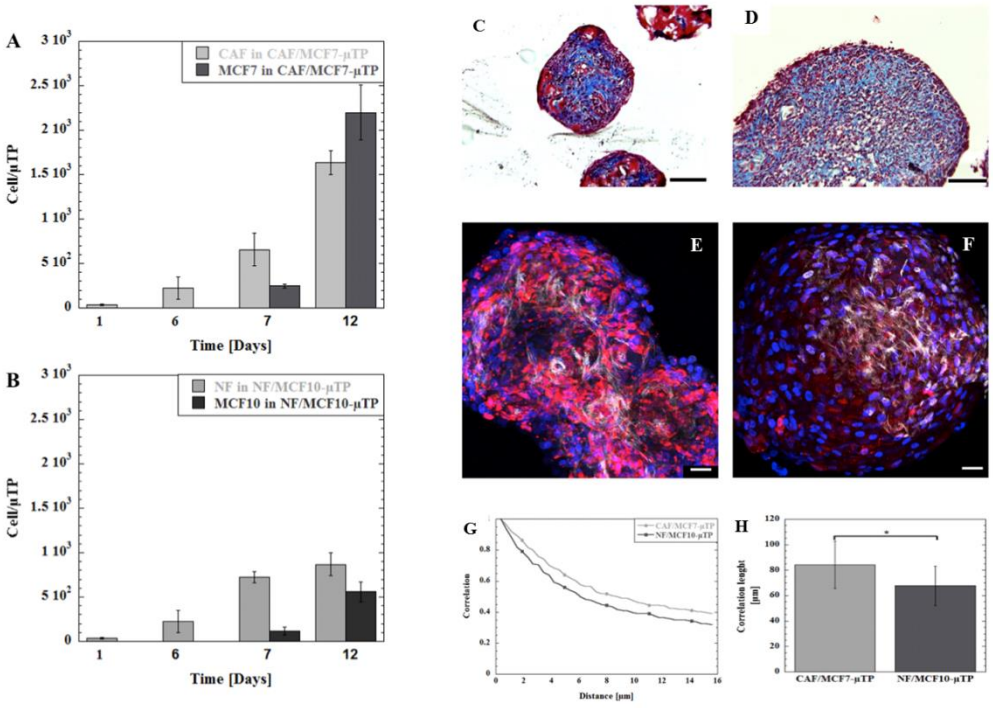

Figure 2.8: Proliferation of CAF and MCF7 cells in tumour µTP (A) and NF and MCF10 cells in healthy µTP (B) Masson's Trichrome staining in CAF/MCF7- (C) and NF/MCF10-µTP (D) (scale bar: 100 µm); SHG images of CAF/MCF7- (E) and NF/MCF10-µTP (F) (cell nuclei in blue, CAF and NF in red and SHG signal in gray; scale bar: 100 µm); Correlation curve (G) as a function of distance in µm in CAF/MCF7-µTP (light gray) and NF/MCF10-µTP (dark gray); Correlation length obtained by fitting parameters from normalized correlation curves. Whiskers and asterisks indicate the statistical difference with $p < 0.05$ (H). ***Reprinted from [6].***

2.3.4 MMP-2 overexpression in 3D tumour µTP

The expression and enzymatic activity of endogenous MMP-2 secreted by cells in the CAF/MCF7- and the NF/MCF10-µTP was verified by RT-PCR (Figure 2.9A), immunostaining (Figure 2.9 B-D) and zymography (Figure 2.9 E). As reported in Figure 2.9 A, a slight difference in the gene expression of MMP-2 in the two µTP models was detected. MMP-2 was synthesized and secreted in a zymogen form and later it was activated by means of a cleavage before the secretion in the extracellular milieu. Indeed, as shown in Figure 2.9 B and C, the 3D tumour tissue expressed greater levels of the MMP-2 protein than the normal one (Figure 2.9 C). Furthermore, zymography results demonstrated

that, although the inactive form of MMP-2 was greater in the 3D normal tissue ($p < 0.05$), a higher amount of MMP-2 activity was found in the CAF/MCF7-µTP compared to the NF/MCF10-µTP ($p < 0.05$, Figure 2.9 E). These findings were confirmed by quantification analysis of immunofluorescence images ($p < 0.05$, Figure 2.9 D). Here we demonstrated the extent and the localization of MMP-2 at extracellular level and its overexpression compared to the healthy tissue.

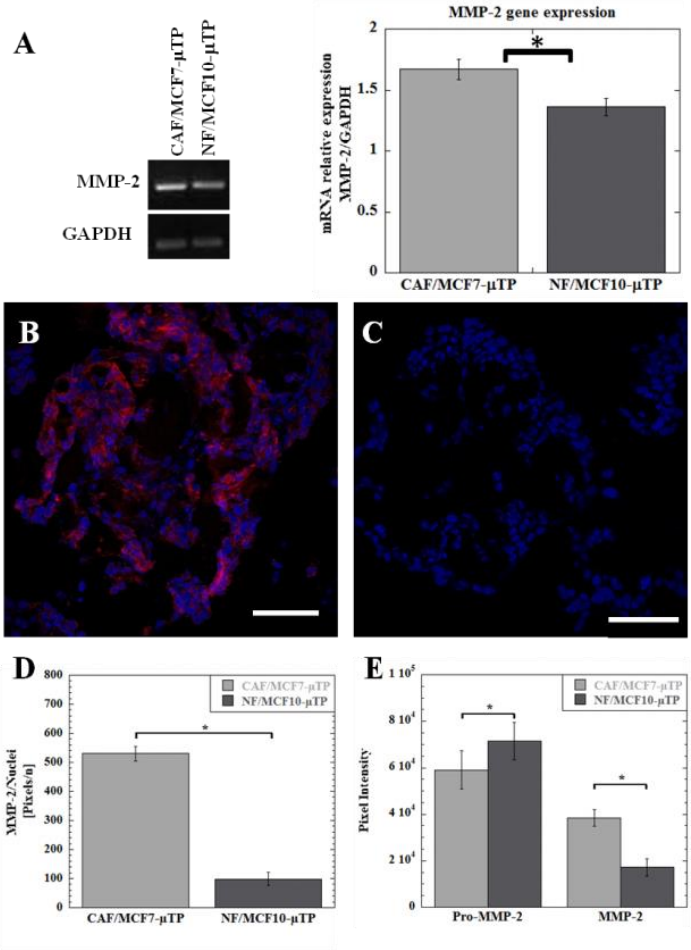

Figure 2.9: MMP-2 levels in CAF/MCF7- and NF/MCF10-µTP. (A) MMP-2 gene expression and quantitative analysis of the MMP-2 expression obtained from RT-PCR. Immunofluorescence staining of MMP-2 protein (red) in CAF/MCF7- (B) and NF/MCF10-µTP (C) (cell nuclei in blue, MMP protein in red, scale bar: 75 µm); quantification analysis of MMP-2 obtained from immunofluorescence (D). Gelatin zymography showing the MMP-2 activity of CAF/MCF7- and NF/MCF10-µTPs (E). Whiskers and asterisks indicate the statistical difference with $p < 0.05$. *Reprinted from [6].*

2.3.5 In vitro NP localization and their cytotoxic effect on μTPs

After the accurate and systematic characterization of *in vitro* growth and MMP-2 expression levels of the produced microtissues, their response to MMP-2-sensitive PELGA-TAP NPs and to their negative control (PLGA-Dox NPs) was assessed.

PELGA-TAP and the PELGA-Dox NPs cytotoxicity in CAF/MCF7- and NF/MCF10-μTPs was investigated as a function of cell viability by means of MTT assay. Figure 2.10 show cell viability percentage of the treated 3D-μTP normalized to non-treated 3D-μTP as a function of drug concentration after a contact time of 48 and 72 h. In particular, after PELGA-TAP NP treatment, an increase in NP cytotoxic effect was observed only in the 3D tumour tissue, increasing the incubation time (Figure 2.10 A and C). In order to measure cell viability, the half-maximal inhibitory concentration (IC_{50} value) indicator was employed. The IC_{50} value was reached only for the CAF/MCF7-μTP after the PELGA-TAP NP exposure for 72 h at 4 μg/ml of Dox concentration (Figure 2.10 C). On the contrary, no inhibition effect in cell proliferation was found in NF/MCF10-μTP after PELGA-TAP NP treatment for 48 and 72 h at any Dox concentration (Figure 2.10 A-C). In Figure 2.10 B and D no reduction in cell viability was detected for both 3D healthy and tumour tissue after the PELGA-Dox NP treatment. These results clearly demonstrate the selective cytotoxic effect of the MMP-2-*stimuli-responsive* PELGA-TAP NP on tumour tissues ($p < 0.05$, Figure 2.10 A and C).

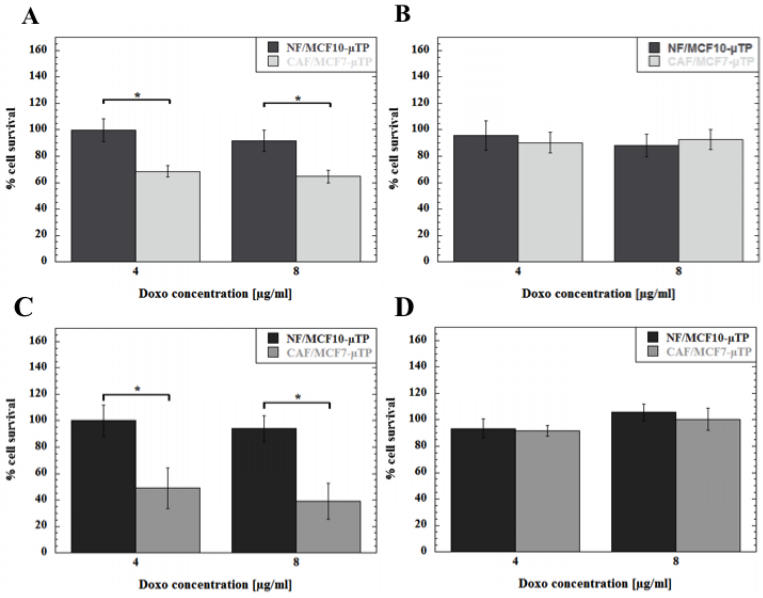

Figure 2.10: Cytotoxicity assay in tumour CAF/MCF7-µTP after treatment with PELGA-TAP (A) and PELGA-Dox (B) NP and in healthy tissue NF/MCF7-µTP after PELGA-TAP (C) and PELGA-Dox (D) NP treatment at 4 and 8 µg/ml for 48 and 72 h. Whiskers and asterisks indicate the statistical difference with $p < 0.05$. ***Reprinted from [6].***

Further, CAF/MCF7- and the NF/MCF10-µTP were exposed to PELGA-TAP and PELGA-Dox NPs at a final Dox concentration of 4 and 8 µg/ml for 48 and 72 h for confocal microscopy analysis. These analyses were performed in order to demonstrate the difference in terms of Dox internalization between healthy and tumour microtissues, due to the different amount of MMPs secreted in the two microenvironments. Figure 2.11 shows the fluorescence images of the 3D tumour and healthy microtissues after PELGA-TAP (Figure 2.11 A and C) and PELGA-Dox NPs (Figure 2.11 B and D) treatment at a concentration of 4 µg/ml for 72 h. As shown in Figure 2.11 A, a diffused fluorescence can be noticed around cells in the CAF/MCF7-µTP incubated with the PELGA-TAP NPs, indicating the release of free Dox after MMP-2 cleavage. On the other hand, a very low spotted fluorescence was observed when the 3D tumour tissues were treated with PELGA-Dox NP for 72 h (Figure 2.11 B). More interestingly, a low or no detectable fluorescence of free Dox after both NPs treatments in the 3D healthy tissue was detected (Figure 2.11 C-D). Furthermore, brightfield images (Figure 2.11 E-J) show a reduction in CAF/MCF7-µTPs diameter treated with PELGA-TAP NPs at a final Dox concentration of 4 µg/ml for 48 and 72h (Figure 2.11 F and G, respectively) when compared to with the untreated ones (Figure 2.11 E). This reduction is reasonably due to the detachment of the outer cells from the CAF/MCF7-µTP, indicated by white arrows in Figure 2.11 F and G. On the contrary, NF/MCF10-µTP treated with PELGA-TAP NPs at a final Dox concentration of 4 µg/ml

for 48 and 72 h (Figure 2.11 I and J, respectively) did not show any changes in their diameter, when compared with the untreated one (Figure 2.11 H), indicating lower Dox release from NPs in the 3D healthy tissue as a consequence of a the lower MMP-2 expression of the latter.

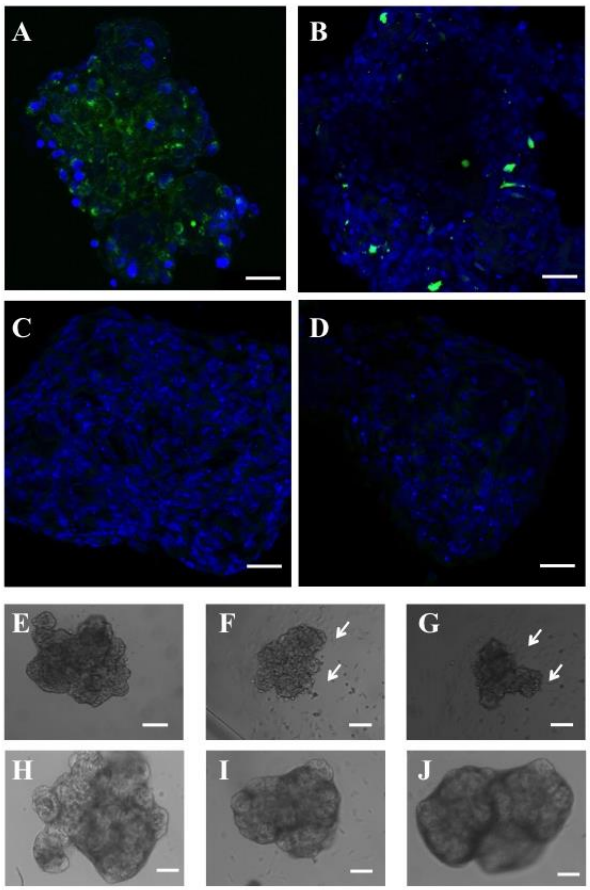

Figure 2.11: Fluorescence distribution of Dox within CAF/MCF7-µTP upon 72 h incubation with PELGA-TAP (A) and PELGA-Dox (B) NP at 4 µg/ml and within NF/MCF10-µTP treated with PELGA-TAP (C) and PELGA-Dox (D) NP (scale bar: 50 µm). The images are the maximum projection of confocal z-sectioning of the whole µTP. Brightfield images of CAF/MCF7- (F-G) and NF/MCF10-µTP (I-J) after 48 and 72 h of treatment with 4 µg/ml of PELGA-TAP NP. Controls are not treated CAF/MCF7- and NF/MCF10-µTP (E-H). White arrows (F-G) indicated the detachment of the outer cells from the CAF/MCF7-µTP, due to drug action. Scale bar: 200 µm. *Reprinted from [6].*

2.4 Discussions

The success of the nanomedicine-based therapeutic approach is mainly due to the improved accumulation of active drugs at disease sites because of the enhancement of drug solubility, bioavailability and prolonged circulation time [83]. In this scenario, it is mandatory to have an *in vitro* 3D tumour model mimicking the *in vivo* tumour features in order to more accurately predict nanocarrier response at the tumour site. Previous works of our group demonstrated that the 3D-μTP model better recapitulates the ECM dynamics seen *in vivo* compared to other 3D cell culture systems (spheroids or cells embedded in natural or synthetic gels) [76] [77] [84]. In this work, a 3D tumour model composed of tumour epithelial cells (MCF7) and cancer-associated fibroblasts cells (CAF) was proposed. The results regarding the cell growth in normal and tumour microtissues highlighted the greater proliferative capability of epithelial and stromal cells in the 3D tumour tissue compared to their healthy counterparts. It is common knowledge that the tumour ECM proteins are a source of physical resistance to drug transport [83]. Among ECM proteins, the one that mostly contributes to drug resistance is collagen [84]. Apart from activation of chemical signals promoting tumour progression, tumour stroma physically limits the penetration of molecular drugs into the tumour site [85]. An innovative and very impressive method to detect the modification of ECM in normal and tumour tissue, also used as diagnostic tool, is the two-photon microscopy, in particular the detection of the SHG signal. Thanks to this technique, we were able to identify the presence of a strong fibrillar collagen in the 3D tumour and healthy tissue, indicating a massive deposition of collagen fibers with different organization. In particular, the correlation (*Cor*) of the collagen network evaluated by GLCM texture analysis detected the transition from a fine to a wavy or coarse architecture. In our case, the collagen assembled by normal fibroblasts had a finer structure than that of CAF. These data demonstrated the ability of stromal cells to produce a dense matrix structure in the μTP configuration. Moreover, the correlation length values calculated *in vitro* in our model reflect the same trend of the values measured *in vivo* [86] [87]. Taken all together, these results show that μTP represents a more relevant *in vitro* model that better resembles the 3D architecture and functionality of the original tissues.

Based on these finding, breast malignant and healthy μTP were used as screening platform to further validate the efficacy of a recently developed nanoformulation, namely

PELGA-TAP NP in a more complex *in vitro* tissue equivalent. PELGA-TAP NPs design is based on the presence of a tumour-activated prodrug composed by a MMP-2 sensitive peptide covalently bounded to Dox. Once in the tumour site, the NPs meets the MMP-2 enzymes which cleave the peptide sequence thus allowing drug release [4]. Since drug release occurs as a consequence of the cleavage of the MMP-2 sensitive peptide, the expression levels of MMP-2 in the healthy and tumoural μTP models was verified. As expected, the tumour microtissues expressed higher levels of MMP-2 when compared to the healthy counterpart. The produced NPs were characterized in terms of size and morphology showing a regular and spherical shape and a size below 100 nm for all batches used in this work. The therapeutic effectiveness of PELGA-TAP NPs was evaluated by imaging and cytotoxicity assay. PELGA-Dox NPs, without the peptide sequence, were also tested as a negative control. In particular, PELGA-TAP NPs show a significant reduction in cell viability in the 3D tumour tissue when compared to the control NPs (PELGA-Dox). In the latter case, the reduced cytotoxic effect was due to the covalent bond of Dox to NP that do not promote drug release. These results are in accordance with the ones reported in the previous chapter, where PELGA-TAP NPs were tested on tumour homotypic spheroids, without the stromal component [4]. In this case, the disaggregation of tumour spheroids was reached after 48 h of the PELGA-TAP NP treatment. Our results show that the same significant cytotoxic effect was reached later, after 72 h of NP treatment, suggesting a role of the ECM in delaying the drug effect. As expected, PELGA-TAP NP did not affect the healthy microtissues. These results further validate NPs production protocol and reproducibility along with their effectiveness in a more realistic *in vitro* model which more faithfully replicate the physiological and pathological microenvironmental conditions occurring *in vivo*, when compared to the standard spheroidal model.

2.5 Conclusions

In this work a recently proposed formulation of endogenous *stimuli-responsive* nanoparticles was tested on a novel 3D human cancer and healthy breast tissue model. The latter, better recapitulate the *in vivo* tumour microenvironment due to the presence of high proliferative cells and a dense matrix structure, enabling a better pre-clinical evaluation of the above mentioned NPs. The cytotoxic results, obtained after PELGA-TAP NPs treatment of the μTPs, strongly validate the efficacy of the system based on the integration of the concept of pro-drug along with the possibility to have an endogenous *stimuli-responsive* drug release which, in turn, leads to the accumulation of the drug in the tumour extracellular space, thus enhancing the anticancer drug activity and reducing undesirable side effects on healthy tissues.

Acknowledgements

We thank Dr. Valentina La Tilla for graphical support, Dr. Roberta Infranca for her precious and careful proofreading and Dr. Valentina Mollo for her helpful support in Cryo-TEM observations. Moreover, we are grateful for financial support provided by the following grants: FIRB project Newton (RBAP11BYNP_004) of the Italian Ministry of Education, University and Research (MIUR).

Chapter.3 **MMP-2-cleavable crosslinked oil-core nanocapsules for spatially-controlled drug release in 3D tumour spheroids**

ABSTRACT

In the war against cancer, nanotechnology-based systems such as nanocapsules play a significant role by enhancing the efficacy of conventional therapies. Here we try to address some major limitations plaguing anticancer drugs, namely poor water-solubility and off-target toxicity. The proposed delivery systems are cross-linked polyelectrolytes nanocapsules based on an oil-core and a matrix metallo-proteases 2 (MMP-2)-sensitive shell. Indeed nanocapsules are stabilized by a MMP-2-cleavable peptide sequence, used as cross-linker. They can load hydrophobic drugs and prevent their systemic leakage. Moreover, thanks to a stability enhancement strategy, promoted by the presence of a cross linker, the system maintains its integrity in physiological conditions up to one month. Further, these nanocapsules are capable to release their payloads when they reach the tumour site, which typically up-regulates MMP-2 expression. These enzymes catalyze the disassembly of the nanocapsules' shell thus allowing drug release in tumour microenvironment. These observations were confirmed by the *in vitro* testing of the nanocapsules on 3D tumour and healthy spheroids. Therefore, these devices hold promises as smart systems capable to transport drug in a safe manner thanks to their high stability, and at the same time deliver their cargo in a spatially-controlled fashion upon an endogenous *stimulus* coming from the very nature of the tumour itself*.

KEYWORDS: Nanocapsules, layer by layer, cross-linked shell, MMP-2 responsive drug release, 3D spheroidal model.

*The work described in this Chapter is part of a paper in preparation: G. Iaccarino[§], **M. Profeta**[§], R. Vecchione, P.A. Netti, "Matrix Metalloproteinases cleavable nanocapsules for tumour activated drug release".

(§) These authors equally contributed to the work.

3.1 Introduction

Although pretty much insight has been gained into tumour biology and giant leaps have been made in diagnostic devices, cancer still remains one of the most devastating diseases in the world and its treatment an open challenge. Current anticancer strategies are based on surgery, radiation and chemotherapeutic drugs, which often also kill healthy cells causing severe toxicity to the patient. Typically, conventional chemotherapeutic approaches make use of poor water-soluble agents, which allow for very little control in terms of where they are distributed in the body and how fast they are cleared. This implies, in turn, a poor pharmacokinetics of the drug, which dramatically decreases its therapeutic index while increasing off-target toxicity. It is in this scenario that the concept of enhanced control and specificity has emerged as one of the main themes in nanomedicine [88] and a new generation of nanocarriers for the controlled and selective release of anticancer drugs has blossomed. Especially the past decade has witnessed a technological leap that deals with on-demand drug delivery systems allowing for spatio-temporal and dosage control therapeutic profiles in response to specific *stimuli* [89]. These nanocarriers may be engineered to be sensitive to either exogenous or endogenous *stimuli*. Several examples of photo- [90], thermo- [91], magnetic- [92] or ultrasound-sensitive [93] drug delivery systems have been proposed to achieve a remote control of drug release through extracorporeal physical *stimuli*. On the other hand, taking advantage of specific microenvironmental changes associated with neoplastic diseases represents an alternative smart strategy to stimulate spontaneously tailored release profiles. Lowered interstitial pH [94], altered redox potential [95] and the up-regulation of certain enzymes [96] are all potential endogenous *stimuli* associated to tumour microenvironment. In particular, MMP-2 are a family of proteolytic enzymes playing a central role in tumour angiogenesis, progression and invasion by remodeling of the extracellular matrix (ECM) [97]. These enzymes, also known as gelatinase A, (Mw: 72 kDa) hydrolyze type IV collagen, which is a major constituent of tumour ECM [98]. Therefore, the use of MMP-2 as a trigger to promote selective drug release to tumours holds great promise for the development of new therapeutic platforms [99] [96, 100]. On the other hand, to improve the pharmacokinetics of the drug and reduce its side effects, it is also crucial to prevent systemic leakage of the payload from delivery systems. To this aim enhancing the stability of nanocarriers during blood circulation can really make the difference in the accumulation of the drug at the

tumour site [101] [102]. Within the vast panorama of nanoparticle-based drug delivery, oil-core multilayer nanocapsules (NCs) are ideal systems. Based on their core/shell architecture, they may significantly increase the blood solubility of most anticancer drugs and shield them from the physiologic environment. Moreover, these systems may be implemented with several additional functions by finely tuning their multilayer structure. However, like several delivery systems, oil-core multilayer NCs often suffer from stability issues leading to an a-specific release of the drug.

Here, we designed and prepared cross-linked trilayer NCs based on an oil-core and an MMP-2-sensitive shell. In particular, the core/shell architecture of our NCs is designed to safely encapsulate hydrophobic drugs and selectively release them to tumours. The liquid core is based on a monodisperse O/W nanoemulsion (NE), pre-loading Paclitaxel as a model chemotherapeutic agent. The multilayer shell protects the payload, provides a hydrophilic interface and allows for a tunable release. The polymers composing the NC shell are nature-derived polysaccharides, namely chitosan and heparin, which we have chemically modified and subsequently assembled around the liquid core by a facile Layer-by-Layer (LbL) method [103]. To prevent premature disassembly and consequent systemic leakage of the payload, we cross-linked the polyelectrolyte layers of the NC shell *via* click chemistry [101]. In particular, we chose as cross-linker a MMP-2 cleavable peptide (Gly-Pro-Leu-Gly-Ile-Ala-Gly-Gln) [100] [48] [4] which we designed as part of an elegant supramolecular structure. The modified peptide (Lys-Gly-Pro-Leu-Gly-Ile-Ala-Gly-Gln-βAla-Asp(allyl)) is rhodamine labeled and allows for conjugation with heparin at one terminus, and for thio-lene photoreaction with chitosan at the other terminus. In this context, the peptide linker plays a dual role for the system. On one side, it enhances NC stability in physiological media, through the covalent stabilization provided to the shell, which in turn limits off-site toxicity. On the other side, it promotes NC disruption in tumour tissues via enzymatic cleavage, hence enabling a site-specific drug release.

The microenvironmentally-triggered and tumour-selective drug delivery features of the NCs were proved by testing their cytotoxic effect and drug diffusion within a three dimensional (3D) biological model. In particular, tumour and healthy spheroids of U87 and HDF cells, respectively were used since multicellular spheroids represents a robust drug screening platform which properly recapitulates the tissue architecture along with its microenvironment [21].

3.2 Materials and Methods

3.2.1 Materials

Chitosan low molecular weight (CT-LMW, 90-150 kDa), heparin sodium salt (from porcine intestinal mucosa), 1-hydroxybenzotriazole hydrate (HOBt), acetic acid, sodium acetate, sodium chloride, N-acetyl-L-cysteine (NAC), allylamine, sodium nitrite, methanol, ammonium hydroxide solution, sodium borohydride, hydrochloric acid, sodium hydroxide, deuterium oxide (D2O), dithiobis(2-nitrobenzoic acid) (DTNB), fluorescein isothiocyanate (FITC), N-(3-Dimethylaminopropyl)-N'-ethylcarbodiimide hydrochloride (EDC), O-benzo-triazole-N,N,N,N'-tetramethyluroniumhexafluorophosphate (HBTU), N,N-diisopropylethylamine (DIPEA), anhydrous N,N-dimethylformamide (DMF), piperidine, trifluoroacetic acid (TFA), Triisopropylsilane (TIS), dichloromethane (DCM), 2-(N-Morpholino) ethanesulfonic acid (MES) sodium salt, HEPES, p-aminophenylmercuric acetate (APMA), acetonitrile (ACN) HPLC grade water, 1-[bis(dimethylamino)methylene]-1H-1,2,3-triazolo[4,5-b]pyridinium 3-oxid hexafluorophosphate (HATU reagent) and buffer solutions were obtained from Sigma–Aldrich (Saint Louis, MO). Recombinant Human Matrix metalloproteinase-2 (MMP-2) was purchased from Peprotech Inc. (Rocky Hill, NJ). Soy-bean oil (density at 20 °C of 0.922 g/ml) and Lipoid E80 lecithin (egg lecithin powder 80 85% enriched with phosphatidyl choline and 7-9.5% content in phosphatidyl ethanolamine) were purchased from Lipoid. Glycol chitosan (GC) was purchased from Wako Chemicals. Dialysis membranes were purchased from Spectrum Laboratories Inc.

3.2.2 Peptide synthesis

MMP-2 sensitive peptide (NH_2-Lys-Gly-Pro-Leu-Gly-Ile-Ala-Gly-Gln-βAla-Asp(allyl)-COOH) was synthesized in a modified version, with a 4-Methyltrityl (Mtt) protected lysine at the N-terminal, a beta alanine spacer and an allylated aspartic acid at the C-terminal. It was employed the solid-phase method and standard Fmoc strategies. Rink-amide resin (substitution 0.7 mmol/g) was used as solid support. Amino acids were activated using 2-(1H-Benzotriazole-1-yl)-1,1,3,3-tetramethyluroniumhexafluorophosphate: hydroxybenzotriazole: N,N-diisopropylethylamine (HBTU/HOBt/DIEA) (1 : 1 : 2). All

couplings were performed for 15 minutes and deprotections for 10 minutes. Peptides were not removed from the resin after acetylation step to allow coupling reaction with rhodamine while still attached. Peptides purity and identity were confirmed by LC-MS (Agilent 6530 Accurate-Mass Q-TOF LC/MS spectrometer). Purified peptide was lyophilized and stored at 4 °C until use.

Reagents for peptide synthesis (Fmoc-protected amino acids, resins, activation and deprotection reagents) were from Iris Biotech GmbH.

3.2.3 Labeling reaction

Before the coupling reaction of peptides with rhodamine, the Mtt group protecting the side chain of the lysine residue was selectively removed using 1% TFA in DCM plus 1-5% TIS. Pre-swelled dry resin (100 mg) was repeatedly rinsed with the as prepared deprotection mixture of solvents for 2 minutes and flushed. Complete deprotection of amines was assessed by Kaiser test and mass spectrometry.

For labeling reaction, carboxylated rhodamine and activating agents (EDC/HOBt) were let reacting overnight with the pre-swelled dry resin in DCM. At the end of reaction the resin was washed several times with DMF. In order to check for left free amines in the side chain of the peptide, Kaiser test and LC/MS were performed at the end of reaction. Then, only before coupling reaction with heparin, the peptide was deprotected from Fmoc at the N-terminus and removed from the resin. Experimentally, Fmoc groups were removed with 20% piperidine solution in DMF. Peptides were removed from the resin by treatment with a TFA/TIS/H_2O (95 : 2.5 : 2.5, v/v/v) mixture for 90 min at room temperature, then, crude peptide was precipitated in cold diethyl-ether, dissolved in a water/acetonitrile (1:1, v/v) mixture, freeze-dried for 48h and stored at -20°C.

All the procedures described for both the synthesis and the labeling of the peptide were applied also to the control sequence peptide.

3.2.4 Heparin - peptide coupling reaction

The condensation of the carboxylic acids of heparin chains with the peptide N-terminus was carried in slightly basic conditions using a classic EDC/NHS chemistry.

In a typical procedure, heparin (10 mg, 1 equiv) was dissolved in 1 ml of carbonate buffer (pH 7.8). Then, 3.4 mg (22 equiv) of EDC*HCl were added and the solution was stirred at room temperature for 30 min. Two milligrams (22 equiv) of NHS were then added, and the solution was stirred at room temperature for 3 h. Twenty-one point nine milligrams (1 equiv) of rhodamine-labeled peptide were added, and the mixture was stirred overnight. Then, the product of reaction was dialyzed using a 6-8 kDa bag against a mixture of ACN/water 30:70 for 48 h. The purified conjugate was finally freeze-dried and stored at -20°C.

The substitution degree of heparin was assessed by measuring the fluorescence intensity of the rhodamine-peptide after calibration with a water solution of rhodamine-peptide at different concentrations using a spectrofluorimeter (EnSpire 2300 PerkinElmer).

3.2.5 Oil-in-Water nanoemulsion

The O/W nano-emulsions were prepared according to a well-established procedure [7]. First, either Paclitaxel (PXL) or FITC were pre-dissolved in the oil phase. Then, an exact amount of Lipoid E 80 to the soy-bean oil at 60 °C and then sonicated with an immersion sonicator (Ultrasonic Processor VCX500 Sonic and Materials). To obtain the pre-emulsion, the oil phase was added dropwise to a weighted amount of aqueous phase (Milli-Q water) and mixed using the immersion sonicator. The pre-emulsion was finally passed at 2000 bar through the high-pressure valve homogenizer (Microfluidics M110PS) to obtain the final nano-emulsion. The final products were named PXL-loaded and FITC-loaded nanoemulsion, respectively.

3.2.6 Modification of glycol chitosan with N-Acetylcysteine

Thiolation was performed on glycol chitosan (GC, chitosan conjugated with ethylene glycol) according to a procedure previously reported [104]. In the typical procedure, 0.5 mmol of the chitosan substrate were dissolved in 10 ml of Milli-Q water. In the first place, the pH was adjusted to a value of 4 with HCl 1 M to allow complete dissolution. Then,

amounts of NAC and coupling agents were added to the solution according to the following molar ratio HOBt : GC : NAC : EDC = 1 : 1 : 4 : 16. Then the pH was raised and maintained to a value of 6.8 throughout the reaction time (6 h). The reaction proceeded at room temperature. The product was then purified by dialysis four times against water containing 1% (w/v) NaCl and acidified with HCl at pH = 3, four times against water acidified at pH = 3. Finally, the purified product was freeze-dried for 48 h.

Total and free thiols were determined using a colorimetric assay, the Ellman's test. In particular, after reaction of thiolated chitosan with a DTNB solution at 25 °C for 2 h, absorbance was registered at 412 nm using a Varian Cary Scan 100 Spectrophotometer.

3.2.7 LbL deposition of functionalized polymers on O/W nanoemulsion

Monolayer, bilayer and trilayer were obtained by a customized LbL deposition procedure. The trilayer NCs were prepared by aid of two syringe pumps (HARVARD APPARATUS 11 PLUS) and an ultrasonic bath (FALC INSTRUMENTS) under specific flow and ultrasounds conditions. Starting from the negatively charged NEs a GC-NAC layer was first deposited. Then, a negatively charged second layer was deposited by mixing the monolayer suspension with a HEP-RHOD-PEP aqueous solution. Finally, the bilayer was mixed with a solution of GC-NAC to give the MMP-2 responsive trilayer with the following final concentrations: 0.25% wt% oil - 0.025 wt% GC-NAC - 0.0069 wt% HEP-RHOD-PEP - 0.02 wt% GC-NAC. The produced NC was named MMP-NC. The same procedure for the preparation of trilayer NCs was followed also using the control peptide modified heparin (HEP-RHOD-ctrlPEP) and the non-functionalized heparin (HEP) the trilayers were prepared following but with the same final trilayer concentrations as for the one prepared with HEP-RHOD-PEP. The latter were named SCR-NC and NF-NC, respectively.

3.2.8 Photoreaction of the multilayer

The trilayer NCs made with both kinds of the modified heparin (rhodamine-peptide heparin and rhodamine-control peptide heparin) were irradiated with UV light for 2 h using

a UV Hand Lamp Spectroline® E-Series UV lamp (output 6 W, wavelength 254 nm). The light source was at 3 cm distance. Photoreaction was conducted without a photoinitiator.

3.2.9 Particle size and ξ-potential characterization

All the suspensions were diluted to a droplet concentration of approximately 0.025 (wt%), using Milli-Q water in the case of NE and multilayers terminating with heparin. Instead the NCs terminating with a chitosan layer were diluted in acidified Milli-Q water solution (pH 4).

3.2.10 Stability tests on crosslinked and not crosslinked trilayers

The stability test of the NCs over time was performed dispersing both the crosslinked and not crosslinked trilayers in different media, *i.e.* water at pH = 4, PBS 10 mM pH = 7.4. Stability was determined monitoring by DLS particle size variations over time.

3.2.11 Confocal analysis of trilayer nanocapsules

Trilayer on O/W nano-emulsion was diluted 1:25 to a final oil concentration of 0.01 % w/v in an Eppendorf with PBS 10 mM at pH 7.2 and 200 µl were put in a FD3510 dish for 30 min to allow it to adhere to the surface of the dish. After that, several washes were performed replacing the sample twice with 120 µl of water. Samples were imaged with a Leica TCS STEDCW microscope (Leica-Microsystems, Mannheim, Germany) equipped with an oil immersion 100× objective. Images were acquired with a field of view of 25.6 × 25.6 µm for a pixel size of 25 × 25 nm. The analysis of the images was carried out using LAS AF software.

3.2.12 Cell culture

To test the biological effect of the NCs, human glioma cell line (U87-MG), and primary human dermal fibroblasts (HDF) were used as models of tumour and healthy tissues, respectively [4].

HDF cells were cultured in Eagle's minimal essential medium (EMEM) supplemented with 20 % Bovine Serum Albumine (FBS, Gibco), 1 % of glutamine, 100 U/mL penicillin, 100 mg/mL streptomycin and 2X non-essential aminoacids. U87 cells were cultured with EMEM supplemented with 10 % FBS, 1 % of glutamine and antibiotics.

Both cell lines were maintained in 100 mm diameter cell culture in a humidified controlled atmosphere with 5 % of CO_2, at 37 °C. The medium was changed every 2–3 days.

3.2.13 Spheroids formation and characterization

NCs cytotoxicity was evaluated as a function of MMP-2-mediated drug release, using spheroids of HDF and U87 cells as 3D models of healthy and tumour tissues, respectively [21].

Spheroids were prepared according to a standardized procedure reported in [4]. Briefly, a cell monolayer was trypsinized and 2500 U87 cells or 3000 HDF cells per spheroids were suspended in culture medium containing 0.25 % (w/v) of carboxymethylcellulose (MCM), then seeded onto non-adherent round-bottomed 96-well plates (Corning® Costar®), and cultured at 37 °C, with 5 % CO2, for 24 h to allow spheroids formation.

Image of each well of the 96-well plate was acquired with Zeiss Axio observer.ZU microscope, equipped with an incubation system, using a 10X objective (ZEISS Plan-NEOFLUAR), 24 h after seeding, to monitor and analyse spheroid integrity, sphericity and diameter. A motorized stage is used for this purpose. Single spheroid analysis was performed through image processing using Image-J software, in order to measure spheroids' diameter (D), projected area (A) and perimeter (P). These data were acquired and analysed in order to evaluate the mean spheroids' diameter and the shape factor (ϕ), describing spheroids' sphericity, for each cell line. The coefficient of variation (CV) of spheroids diameter was also evaluated for each cell line [105].

The above mentioned quantities were calculated as follows:

$$\phi = \frac{\pi * \frac{\sqrt{4A}}{\pi}}{P}$$

$$CV = \frac{\sigma}{|\mu|} * 100$$

Moreover, statistical analyses were performed to evaluate the diameter homogeneity of the model between the two cell lines by means of one-way analysis of variance (ANOVA test). A p-value less than 0.05 was considered statistically significant.

3.2.14 MMP-2 expression in tumour and healthy spheroids

To qualitatively evaluate MMP-2 expression in both 3D models, indirect immunofluorescence staining was performed on HDF and U87 spheroids according to the method presented by *Shaheen et. al.* [106], with some modifications. First of all, 48 h after seeding, spheroids were collected and washed twice with PBS, to remove medium and MCM traces. Then, they were fixed with 4 % paraformaldehyde (PAF) in PBS for 20 minutes at room temperature (RT). The fixed samples were washed twice in PBS for 5 min at RT. After that, spheroids were permiabilized using 0.5 % Triton x-100 in PBS for 5 min at RT. Subsequently, spheroids were washed twice with PBS and permiabilization was blocked by adding of 1 % bovine serum albumin (BSA) in PBS for 30 min at RT.

After removing the blocking solution samples were incubated with primary antibody (Abcam UK), diluted 1:200 in 1 % BSA in PBS, 1 h at 37 °C. Then, spheroids were washed twice with 1 % BSA, 0.1 % Tween-20 in PBS, for 10 min at RT and incubated with the secondary antibody (Abcam UK) diluted 1:200 in 1% BSA in PBS for 1 h at RT, avoiding light exposure. Finally, samples were washed three times with 1 % BSA in PBS for at least 5 min of incubation time for each wash.

Samples were imaged by confocal microscope (Leica Microsystems TCS SP5 II, Germany) with a 25x water immersion objective. Images were acquired with a resolution of 1024x1024 pixels.

Moreover, a semi-quantitative analysis was also performed on at least 5 images for each spheroid type to obtain the corrected total spheroid fluorescence (CTSF) using the method reported by *Mc Cloy et al.* [107], with some modifications. Briefly, using ImageJ software, spheroids' borders were delimited with the ROI selection tools and the area and the integrated density (ID) were evaluated. Then, the mean grey value of the background (MGVB) was also measured. Using the obtained parameters, the CTSF was calculated according to the equation that follows:

$$CTSF = ID - (Area\ of\ the\ selected\ spheroid * MGVB)$$

Starting from the CTSF data, statistical analyses were performed to evaluate the difference in the expression levels of MMP-2 between the two cell lines by means of ANOVA test. A p-value less of 0.05 was considered statistically significant.

3.2.15 Drug treatment and cytotoxicity assay

To evaluate NCs cytotoxic effects, 24 h after seeding spheroids were treated with free PXL, SCR-NC and MMP-NC at a final PXL concentration of 200 nM. Spheroids were also treated with cell medium alone as positive control.

Cell viability was evaluated by means of Alamar Blue Assay. *Chung Tung et al.* [108], adapted the above mentioned method for multicellular spheroids, and the experiments were performed according to their procedure with slight modifications. Briefly, after 48 or 72 h of incubation time, samples were washed twice with PBS to remove the non-internalized compounds and incubated for 4 h with a solution containing 10 % of Alamar Blue cell viability reagent (Invitrogen) in cell culture medium. After incubation, spheroids supernatants were collected and their fluorescence was measured at λ_{ex} of 570 and 610 nm, according to the manufacturer's procedure. Compounds were tested in octuplicate for both cell lines and data were reported as the cell viability percentage of treated cells normalized to non-treated cells. At least 4 complete experiments were performed to validate the data.

To qualitatively monitor spheroids shape evolution after treatment, an image of each well of the 96-well plate was acquired with Zeiss Axio observer.ZU microscope, using a 10X objective (ZEISS Plan-NEOFLUAR), as explained in the previous paragraph (see *"Spheroids formation and characterization"*).

Statistical analyses were performed to evaluate the difference in cell viability between the two cell lines and between the compounds, by means of ANOVA test. A p-value less of 0.05 was considered statistically significant.

3.2.16 Confocal imaging and colocalization

The disassembly of the NCs leading to drug diffusion in tumour microenvironment was qualitatively assessed by confocal microscopy imaging. The day after seeding, spheroids were treated with free FITC, FITC-loaded nanoemulsion (namely Nano), NF-NC, SCR-NC and MMP-NC at a final FITC concentration of 200 nM. Spheroids were also treated with

cell medium alone, as positive control. After a contact time of 72 h, spheroids were fixed according to the procedure reported in the previous paragraph (see *"MMP-2 expression in* tumour *and healthy spheroids"*). Finally, spheroids were incubated with DRAQ5 (Abcam) diluted 1:1000 in PBS for 30 min at RT, for cell nuclei staining. Samples were observed by confocal microscope (Leica Microsystems TCS SP5 II, Germany) with a 25x water immersion objective. Images were acquired with a resolution of 1024x1024 pixels.

Semi-quantitative analyses were also performed on at least 5 images for healthy and tumour spheroids treated with the FITC loaded SCR-NC and MMP-NC. Colocalization measurements were performed to evaluate rhodamine and fluoresceine colocalization in the various samples, using JACOP ImageJ plugin [109]. Moreover, the mean intensity ration between the two fluorophores was also evaluated calculating their CTSF, using the method reported in the previous paragraph (see *"MMP-2 expression in* tumour *and healthy spheroids"*).

3.3 **Results**

3.3.1 *Solid phase peptide synthesis*

In order to achieve a stabilization/destabilization mechanism for our NCs, we carefully designed a double-feature peptide linker to embed within the polymer layers of NC shell. In the first place, we identified an amino acidic sequence (Gly-Pro-Leu-Gly-Ile-Ala-Gly-Gln) that was sensitive to MMP-2 catalytic activity. Then, we modified it by adding an allylated aspartic acid to perform thiol-ene click reaction with thiolated chitosan. We also introduced in the sequence an Mtt-lysine which provided the functional moiety to attach rhodamine B to the peptide side chain. Therefore, the resulting modified sequence is Lys-Gly-Pro-Leu-Gly-Ile-Ala-Gly-Gln-βAla-Asp(allyl) (see Figure 3.1 for a schematic representation).

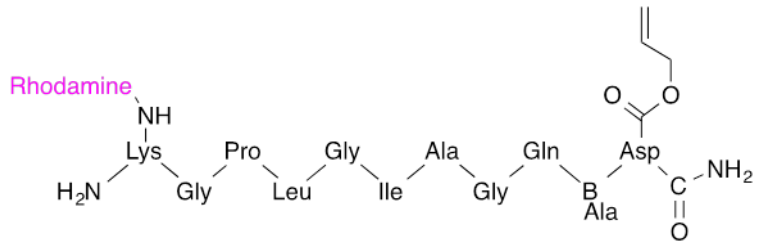

Figure 3.1: MMP-2 peptide sequence modified with rhodamine and allylated aspartic acid.

At the same time, we applied the same strategy for the preparation of a control sequence named RHOD-ctrlPEP (Lys-Leu-Gln-Gly-Ile-Gly-Pro-Gly-βAla-Asp(allyl)), which differs from RHOD-PEP only for the disposition of the amino acids of active domain. We monitored the peptide during all the steps of its modification by mass spectrometry. In Figure 3.2 we report the mass spectra of the peptide after synthesis, coupling with rhodamine B and Fmoc deprotection. First we confirmed the purity and quality of the peptide (Fmoc-PEP) that we synthesized by a solid phase approach. In Figure 3.2 a we report the molecular peak corresponding to the theoretic molecular weight of Fmoc-PEP. Then, after removing the orthogonal Mtt protecting group from lysine in mild acidic conditions, we labeled the peptide with rhodamine B. The effective conjugation is confirmed by the second and third charge mass peak of FMOC-RHOD-PEP (Figure 3.2a). Finally, we checked for complete Fmoc deprotection of the rhodamine labeled peptide (RHOD-PEP) before performing the coupling reaction with heparin. In Figure 3.2 c

RHOD-PEP exact mass and first and second charge are reported. Equivalent results were obtained also for the control scrambled peptide sequence (SCR_PEP).

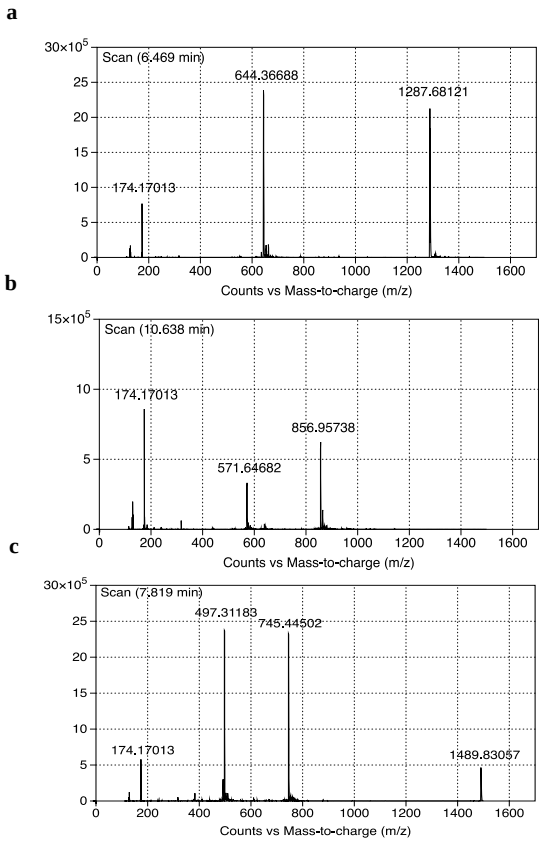

Figure 3.2: Mass spectra of Fmoc-protected peptide after synthesis (a), Fmoc-protected peptide after coupling with rhodamine B (b), rhodamine labeled peptide after Fmoc deprotection (c).

In order to embed the MMP-2 sensitive linker within the polymer layers of the NCs we conjugated the modified peptide sequence with heparin. By condensation reaction between peptide N-terminus and heparin carboxylic acids moieties we achieved around 50 % substitution of the polymer chains. We estimated such value by fluorimetric assay measuring rhodamine signal of the heparin-peptide conjugate ($\lambda_{ex}/\lambda_{em}$ = 550/570 nm). We, indeed, correlated this fluorescence intensity to a rhodamine-peptide calibration curve acquired within a range of concentrations comprised between 0 and 0.065 mM.

In Figure 3.3 we provide a schematic representation of the heparin peptide conjugate that for the sake of shortness we named HEP-RHOD-PEP.

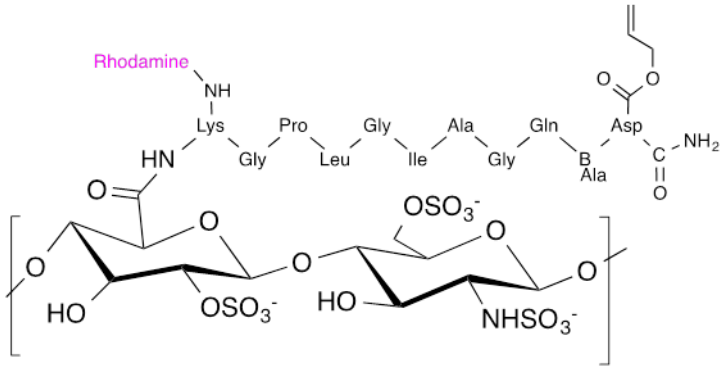

Figure 3.3: Heparin functionalized with the fluorescent MMP-2 peptide.

3.3.2 Glycolated chitosan thiolation with N-acetyl-L-cysteine

Glycolated chitosan was partially substituted at the free amine groups with N-acetyl-L-cysteine (NAC) in order to provide the chains with thiol moieties. A typical amidation reaction was carried in presence of water soluble coupling agents, namely carbodiimide (EDC, ethyl-3-(3- dimethylaminoisopropyl)-carbodiimide) and 1-hydroxy-1,2,3-benzotriazole (HOBt) (in Figure 3.4 a schematic representation of the chemical reaction is provided).

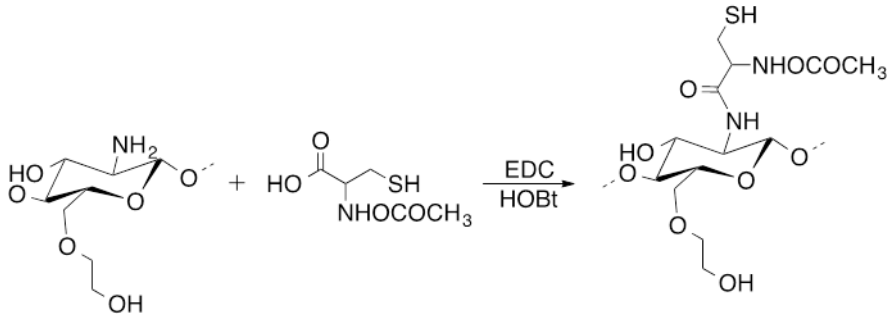

Figure 3.4: Thiolation of glycol chitosan with NAC by EDC/HOBt chemistry.

Although this chemistry is widely used, it is rarely applied to polysaccharides especially in the case of chitosan, since it is difficult to substitute amine groups because of the poor solubility and reactivity of the polymer. The solubility issue was addressed using the glycolated chitosan in place of the LMW chitosan. In fact, the ethylene glycol moieties allowed for water solubility of the polymer even at neutral pH. On the contrary, LMW chitosan requires an acidic pH to reach complete dissolution through amines protonation. This constraint strongly limits the effectiveness of the coupling reaction, which in contrast requires a slightly basic pH in order to make the amines nucleophile. The degree of thiolation that was reached based on our scheme of reaction was assessed by Ellman's test.

This colorimetric assay, indeed, may highlight the concentration of free thiols by reaction with DTNB (also known as Ellman's reagent), which absorbs at 412 nm.

The first step in the construction of the crosslinked polymer NCs was preparing an O/W NE pre-loading Paclitaxel. Following an optimized procedure [7] we obtained narrowly distributed NEs, as shown by the DLS and the cryo-TEM reported in Figure 3.5a and b, respectively. The Paclitaxel (PXL) concentration in the overall volume of the NE was 37.5 μg/ml (44 μM).

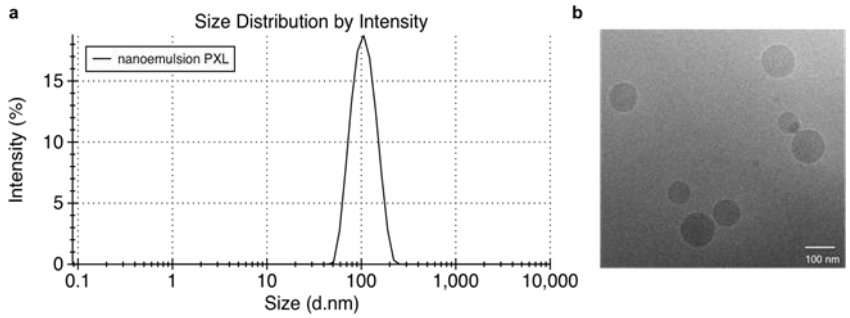

Figure 3.5: Average size of PXL loaded nanoemulsion by DLS (a) and by cryo-TEM (b).

Starting from these oily templates we built our NCs assembling the modified polymers through a customized LbL procedure. First, we deposited a thiolated glycol chitosan (GC-NAC) layer on the negatively charged NEs. The GC-NAC monolayer NCs was then coated with a second layer of functionalized heparin. Finally, a last layer of GC-NAC was deposited. This way we obtained oil-core narrowly distributed trilayer NCs coated with naturally derived polyelectrolytes embedding an MMP-2 sensitive substrate. We shortly named this trilayer as MMP NCs. We also prepared two control series of trilayers based on non-functionalized heparin (HEP) and heparin modified with the control sequence peptide (HEP-SCR_PEP), which in the following will be recall as NF NCs and SCR NCs, respectively. The average size and the Z-potential of the three types of trilayer NCs at each step of the deposition process are summarized in Figure 3.6.

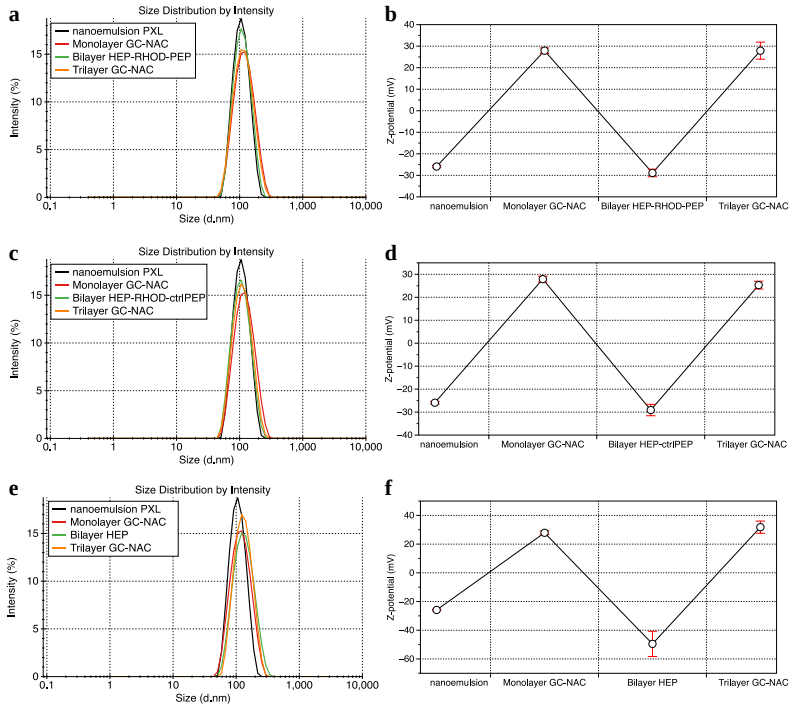

Figure 3.6: Size distribution and z-potential of the three types of trilayer NC: NC MMP (a,b); NC ctrlMMP (c,d); NC NF(e,f).

It is noteworthy, that these results were achieved following an optimized LbL deposition procedure [7], which preserved the small size and narrow size distribution (PDI ≈ 0.1) of the starting NE. In fact, dealing with naturally derived polymers modified with sterically bulky pendant molecules, may really plague the deposition process.

3.3.3 Stability enhancement of MMP-2 trilayer nanocapsules

We then exposed part of the as prepared trilayer NCs to UV light (λ = 254 nm) in order to promote the formation of a tioether bond between the thiol moieties on GC-NAC and the alkene groups on the side chain of the peptide. The click reaction effectively brought to an enhancement of the trilayer stability through the crosslinking of the polymer layers. We performed the stability test by monitoring the size and the PDI of crosslinked and not-crosslinked trilayers in media with different pH and ionic strength, namely acid water (pH 4) and phosphate buffer (PBS 10 mM; pH 7.4). As highlighted by the size and PDI measurements reported in Figure 3.7 A and B respectively, when dispersed in PBS, the crosslinked NCs show an initial swelling (≈ 100 nm), while the PDI does not seem affected by the change of medium.

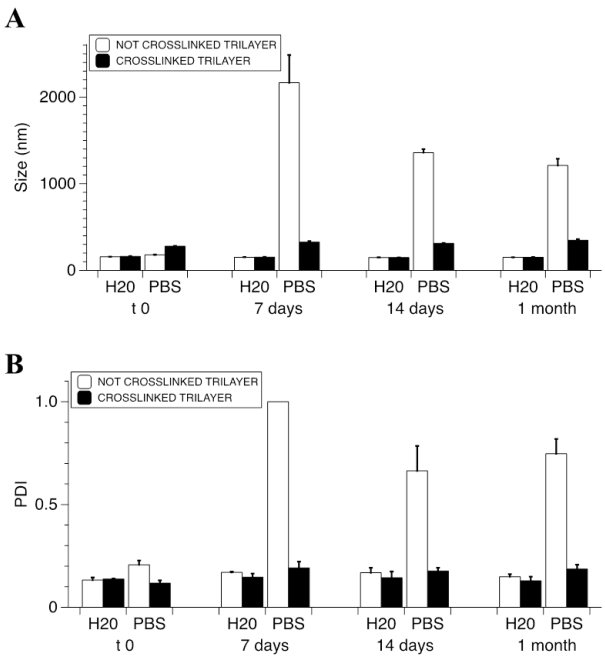

Figure 3.7: Size (A) and PDI (B) changes over time both in acid water and PBS of crosslinked and not crosslinked (HEP-PEP) NC by DLS.

Moreover, this condition keeps constant over about one month. On the other hand the not-crosslinked trilayers completely lose their dimensional characteristics after only one week increasing both their size and PDI in an uncontrolled fashion. Our explenation to this behaviour is that the change of medium causes an expected weakening of the electrostatic interactions between the layers of the NC shell. Due to the lower attraction, the oppositely charged layers get more distant form each other, thus leading to a larger NC size. However, only in the case of crosslinked NCs, the polymer layers are still hold together by some chemical linkages provided by the peptide linkers. These covalent constraints prevent the NC size to further increase, while keeping it to a costant value. This, in turn, would also justify a costant value of the PDI over time since the size increase is uniformely distributed among all the crosslinked NCs.

3.3.4 Spheroidal model characterization and evaluation of their MMP-2 expression

Tumour and healty spheroids of U87 and HDF cell lines, respectively, were chosen as drug screening platform to test the system.

Uniform spheroid dimension and geometry are some of the major characteristics this 3D model should satisfy when used as platform for drug screening. Since that, spheroids were characterized in terms of integrity and omogenity. Brightfield images of all the spheroids were acquired 24 h after seeding, for both cell lines. Figure 3.8 A and B show brightfield images of HDF and U87 spheroids, respectively, and proof that the spheroids have a good integrity and a regular and spherical shape for both cell lines. These observations are confirmed by the data reported in Figure 3.8 C, since the spheroid shape factor is pretty close to 1 and their mean diameter for each cell line is of about 500 μm with a very low CV value (see Figure 3.8 C and D). Finally, spheroid mean diameter among the two cell line may be considered the same since no statistically significant differences emerged, according to ANOVA test results.

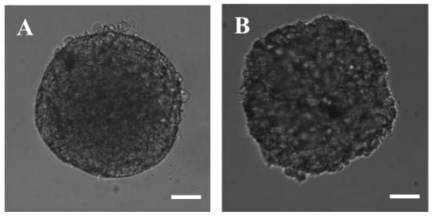

C

	Mean Diameter	CV (%)	ϕ
HDF	492.40 ±28.40	5.76	0.98
U87	499.37 ± 39.17	7.84	0.93

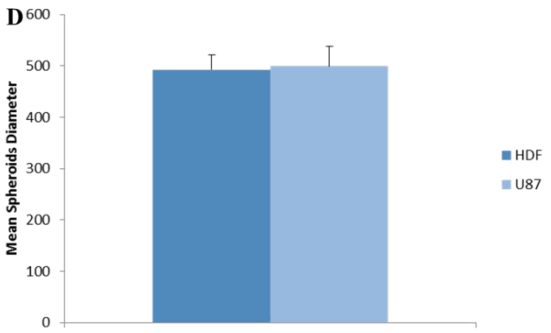

Figure 3.8: Biological model characterization. Transmission image of HDF (A) and U87 (B) spheroids (scale bar:100 μm). Mean diameter, coefficient of variation and shape factor of HDF and U87 spheroids (C); mean diameter values are reported as mean ± standard deviation. HDF and U87 spheroids' mean diameter (D).

Moreover, since the presented NCs are capable to release their cargo as a consequence of the presence of MMP-2 proteins *in situ*, the expression of endogenous MMP-2 secreted by HDF (Figure 3.9 A) and U87 (Figure 3.9 B) were qualitatively verified by indirect immufluorescence. Images show that tumour cells express greater levels of MMP-2 protein when compared to the healthy counterpart.

Semi-quantitative analyses were also perfomed on at least 5 images for each spheroid type and results show that the fluorescence intentisity of the stained protein is about 36% higher in the case of U87 spheroids when compared to HDF. Moreover, ANOVA test results further confirm that the difference between the fluorescence intensity of the stained protein in the two cell lines is statistically significant (Figure 3.9 C).

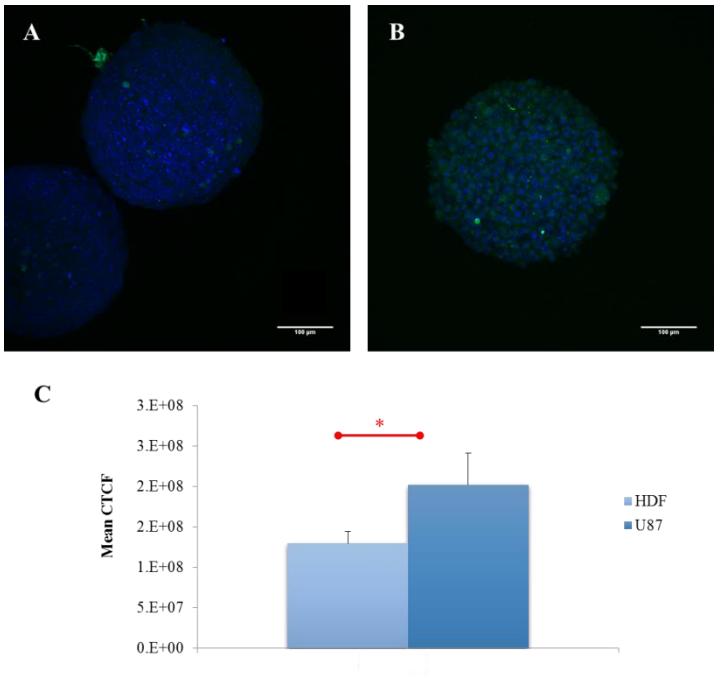

Figure 3.9: Immunofluorescence staining of MMP-2 enzymes in HDF (A) and U87 (B) spheroids. Semi-quantitative evaluation of MMP-2 expression in HDF and U87 spheroids, obtained by immunofluorescence images analysis (C). The Asterisk indicates the statistical difference with $p < 0.05$.

3.3.5 In vitro cytotoxicity assays

Based on the results of the indirect immunofluorescence analysis previously reported (see *"Spheroidal model characterization and evaluation of their MMP-2 expression"*), in order to demonstrate the ability the MMP-NC to sense the differences in the expression levels of endogenous MMP-2 enzyme and, hence, induce NC shell disassembly and cytotoxicity upon specific enzymatic cleavage, U87 and HDF spheroids were used as *in vitro* models of a tumour and a healthy tissue, respectively.

Spheroids of both cell lines were incubated with MMP-NC at a final PXL concentration of 200 nM for 48 and 72 h. To further verify the specificity of action of the MMP-NC, a SCR-NC (*i.e.*, with the presence of a scrambled peptide sequence) was used as negative control. Moreover, spheroids were treated with cell medium alone as positive control, and with free PXL as negative control.

After incubation time, a quantitative evaluation of cell viability (normalized to positive control, which is set to 100 %.) was obtained by means of Alamar Blue Assay (Figure 3.10 A and B). Data show a reduction in U87 spheroids viability after 48 h of treatment with MMP-NC which is significantly different from the viability values reported for the same

spheroids treated with the SCR-NC (p_{48}< 0.05). This difference increases, increasing the incubation time till 72 h (p_{72}< 0.02).

On the other hand, a very low or absent decrease in HDF spheroids *via*bility was observed when treated with MMP-NC or SCR-NC for both contact time and no significant difference was found among the samples.

More interestingly, data show a significant difference between HDF and U87 treated with MMP-NC for both contact time (p_{48}< 0.05; p_{72}< 0.02) but not when treated with SCR-NC.

Taken all together, these results show the specificity of action of the NC upon enzymatic cleavage, along with its safety when in healthy tissues.

Moreover, brightfield images of tumour and healthy spheroids were acquired after compounds treatment for both contact times (Figure 3.10 C and D) and the detachment of the outer cells is clearly visible only for U87 spheroids treated with MMP-NC and for the negative control of course (see red arrows), in accordance with the previously reported cytotoxicity data.

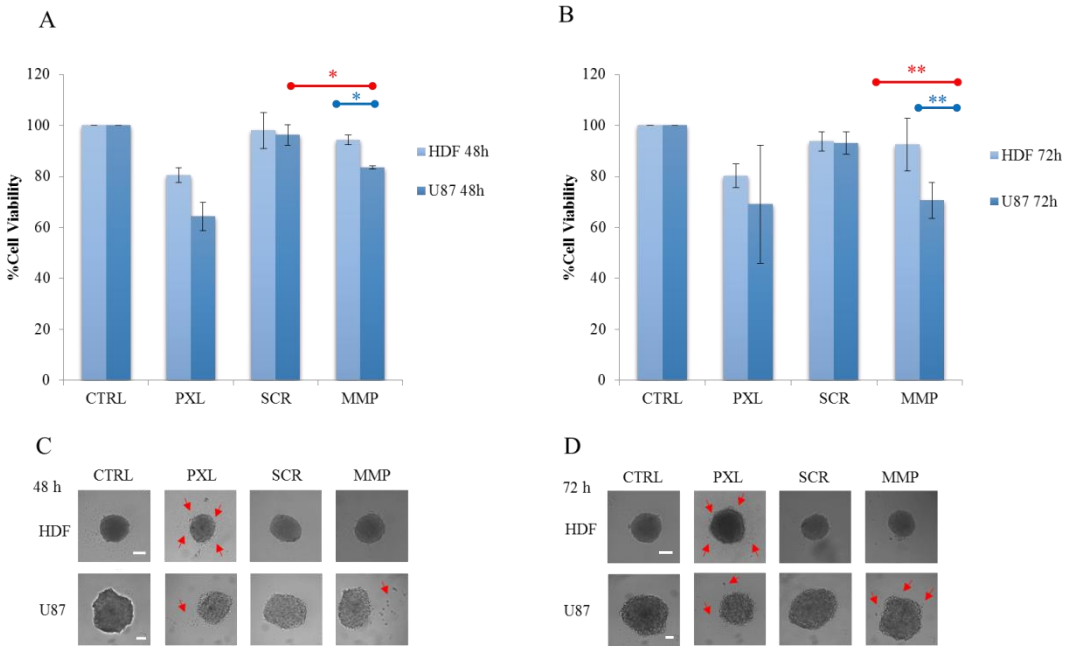

Figure 3.10: Cytotoxicity assay in healthy and tumour spheroids after 48 (A) and 72 h (B) of exposure to compounds; a single asterisks indicates the statistical difference with p<0.05; double asterisks indicates the statistical difference with p<0.02. Transimssion images of healthy and tumour spheroids after 48 (C) and 72 h (D) of exposure to compounds; red arrows show cells detachment from the spheroids, due to drug action. Scale bar: 100 µm.

3.3.6 Confocal imaging and colocalization analyses

The selective disassembly of NCs leading to drug diffusion into tumour microenvironment was assessed by confocal microscopy HDF (Figure 3.11) and U87 (Figure 3.12) spheroids treated with cell culture medium alone (A), free FITC (B) and FITC loaded- nanoemulsion (C), -NF NC (D), -SCR NC (D) and –MMP NC (E) for 72 h were acquired. For a correct interpetation of the following images it is helpful to remember that NCs' core is loaded with FITC, which is commonly represented with a green signal, while the peptides used to crosslink the NC shell are tagged with rhodamine, which is commonly visualised using a red color.

Said that, concerning HDF spheroids, Figure 3.11 B, C and D show the presence of a diffuse green signal coming from the FITC, as expected, while it is noteworthy the presence of a yellow color in Figure 3.11 E and F rising from the colocalization of the red and green channells. Since yellow hotspots proof the presence of the two molecules of interest in the same pixel, this indirectly suggests that the NCs' shell integrity was not compromised in healthy tissue both in the case of SCR and MMP crosslinked NCs. These results confirm the NC stability in an environment with a low or absent presence of MMP-2, such as the healthy tissue microenvironment and are consistent with the stability tests performed by DLS, as previously reported.

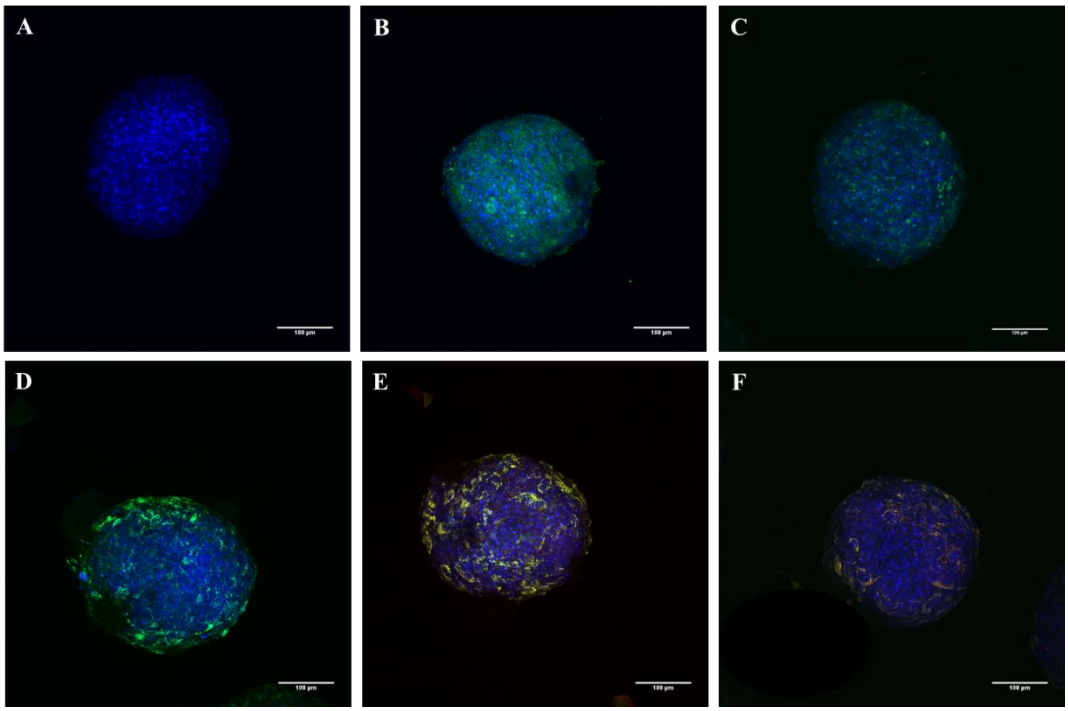

Figure 3.11: Fluorescent distribution of FITC (green) and Rhodamine (red) in HDF spheroids after 72h of treatment with cell culture medium (A), free FITC (B), FITC-loaded nanoemulsion (c), FITC-loaded NF NC (D), FITC-loaded SCR NC (E), FITC-loaded MMP NC (F).

On the other hand, concerning U87 spheroids, Figure 3.12 B, C and D show the presence of diffuse green signal coming from the FITC, as expect, while more interestingly, Figure 3.12 E show a yellow colour rising from the colocalization of the red and green channels and Figure 3.12 F show only the presence of a green signal. These results suggest that SCR-NC architecture is not compromised in a tumour microenvironment, since the MMP-2 enzymatic cleavage does not occur in presence of a scramble peptide sequence, leading to the visualization of a yellow signal coming from the overlay of the green and red channel. On the contrary, tumour spheroids treated with MMP-sensitive NC show the presence of only a green signal since MMP-2 over-expression in tumour microenvironment leads to shell disassembly and consequent drug release from the inner core of the nanocapsules.

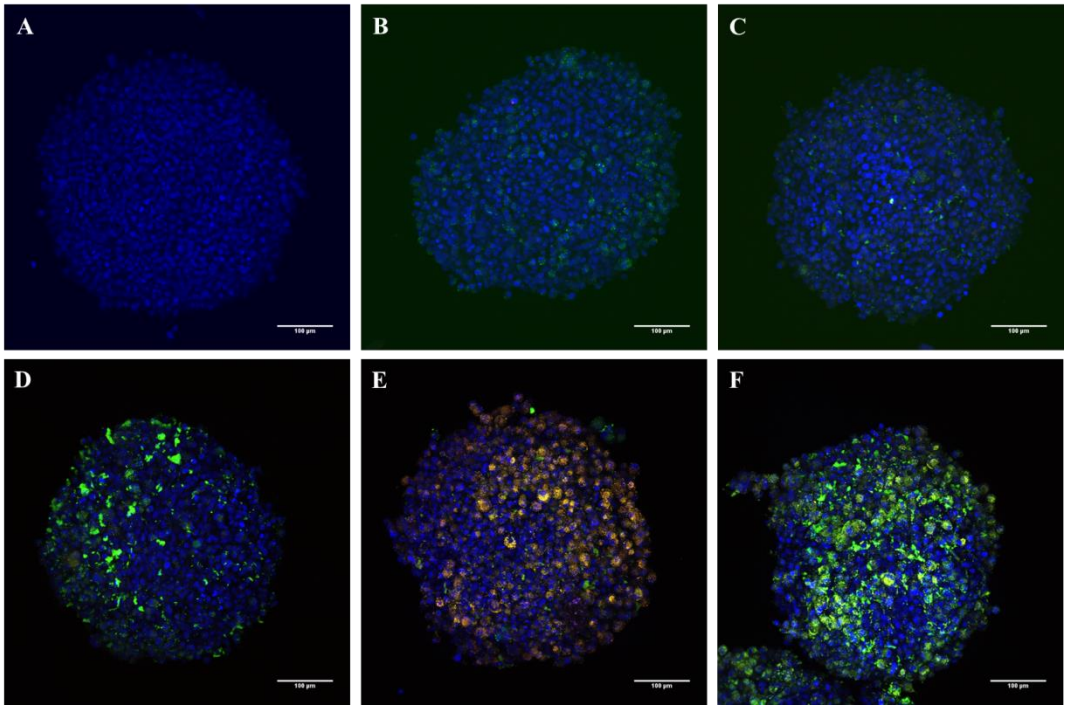

Figure 3.12: Fluorescent distribution of FITC (green) and Rhodamine (red) in U87 spheroids after 72h of treatment with cell culture medium (A), free FITC (B), FITC-loaded nanoemulsion (c), FITC-loaded NF NC (D), FITC-loaded SCR NC (E), FITC-loaded MMP NC (F).

Semi-quantitative analyses were also performed on the above mentioned images to further validate the observations done on the qualitative observation of the images. As can be seen from Figure 3.13 colocalization measurement show a Pearson's coefficient pretty close to one in the case of HDF spheroids treated with both SCR-NC and MMP-NC and in the case of U87 spheroids treated with SCR-NC. On the other hand a lower value of the Pearson's coefficient (PC) was calculated when U87 spheroids were treated with MMP-NC, we can have indirect information concerning shell integrity. Similar considerations can be done on Pearson's scatter plots reported in Figure 3.13. In case of complete colocalization the dots on the diagram appear as a cloud centred on a line and PC tend to 1, otherwise the line changes its slope and approaches the axis of the most intense channel [109]. In the light of these considerations, HDF spheroids treated with both SCR-NC and MMP-NC and U87 spheroids treated with SCR-NC fall in the first case, while U87 spheroids treated with MMP-NC fall in the second one.

Moreover, the mean intensity ratio between the two fluorophores was also evaluated calculating the ration between their CTSF. Data show that in the case of HDF spheroids treated with both SCR-NC and MMP-NC and U87 spheroids treated with SCR-NC, the ratio was roughly one. On the contrary, in the case of U87 treated with MMP-NC, the ratio

was about 0.25 indicating a 75 % higher green fluorescent intensity, when compared to the red one.

A

Cell line	Sample	Pearson's Coefficient	Mean Intensity Ratio beetween Image A and Image B
U87	NC-MMP	0.69 ± 0.06	0.25 ± 0.004
	NC-SCR	0.86 ± 0.1	0.95 ± 0.3
HDF	NC-MMP	0.86 ±0.1	1 ± 0.3
	NC-SCR	0.9678 ± 0.004	1 ± 0.4

B

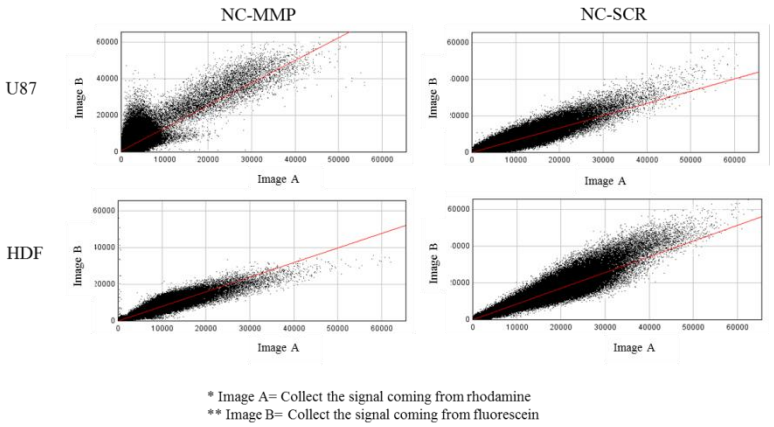

Figure 3.13: Pearson's coefficient values and Mean intensity ratio between Image A and B. Data are reported as mean ± st-dev (A). Pearson's scatter plots of image A against Image B (B).

3.4 Discussions

In order to be effective, nanoparticle based drug delivery systems must meet some major requirements such as good dimensional and morphological features, stability in physiological media and on demand drug release. Indeed, the nanocapsules have excelent dimensional characteristics such as a narrow size distribution. Moreover, the employed crosslinking strategiey may help avoiding uncontrolled drug release from nanoparticle based drug delivery systems by enhancing their stability during blood circulation and thus reducing off target toxicity. At the same time, the presence of a MMP-2-sensitive crosslinker make the nanocapsule system presented in this work an ideal candidate for an effective *stimuli-responsive* drug delivery in response to an andogenous *stimulus* that comes from the very nature of the tumour itself, since these enzyme are up-regulated in tumour tissues.

Tumour and healty spheroids of U87 and HDF cell lines, respectively, were choosen as drug screening platform to test the described compounds and were characterized in terms of spheroids' integrity and omogenity. Results concerning the spheroidal model characterization and evaluation of its MMP-2 expression show that the spheroids' production methods leads to the formation of spherical, compact and homogeneously sized spheroids among and between both cell lines and that the healty and tumour models express different levels of endogenous MMP-2, as expected. These characteristis are crucial when designing spheroid-based drug screening platforms to test *stimuli-responsive* devices [21]. Based on model reliability, cytotoxicity data obtained by means of alamar blue assay proof the specifity of action of the designed NC against tumour cells in response to an endogenus *stimulus* that comes from the very nature of the tumour itself and, more interestingly, data show NC safety when presented to healty tissues. Finally, confocal microscopy images proof that the NCs mainted their integrity in healthy tissue microenvironment and in the tumour microenvironment in the absence of a specific linker able to sense the *stimulus* choosed to induce drug release.

3.5 Conclusions

In this work we focused our attention on one of the major concern related to the administration of anticancer drugs, namely off-target toxicity. To this aim we designed and prepared stabilized oil-core polymer NCs allowing for a spatially-controlled release of their payload in response to an endogenous *stimulus* coming from the very nature of the tumour tissue. In particular, here we propose a new approach to the design of NCs for the delivery of anticancer drugs, combining an enhancement of their stability in physiological-like conditions and a *stimuli*-responsive drug release. Both strategies rely upon the same key element, namely an MMP-2 cleavable peptide that we used to cross-link the NC polymer shell. This peptide linker is thought to prevent the systemic leakage of NC payload during blood circulation, based on the covalent stabilization provided to the system. At the same time, the peptide linker promotes a selective drug release at the tumour site once the NCs explore a high level of endogenous MMP-2 within a 3D tumour model, which catalyze the linker cleavage.

This strategy holds promise as a viable route to address with a single elegant solution both the NC stability issue and the spatially controlled release requirement. These features may contribute to increase the efficacy of the current anticancer therapies thus encouraging further *in vivo* investigation of the system.

Chapter.4 **Outlining the Advantages of an Extracellular Drug Delivery**

ABSTRACT

At present, nanoparticle-based drug delivery is recognized as the most promising weapon we have in the war against cancer, since it armours and guides the drug to the tumour site without causing, or at least reducing, healthy tissues damage. But, if on one hand nanoparticles may effectively protect and transport the drug throw the vasculature, on the other hand, when in tumour interstitium, may impair drug effectiveness by reducing its penetration in the dense tumour mass. In the light of these considerations, here we highlight some of the major advantages associated with an extracellular drug delivery since this approach could bridge the gap between the need of a drug carrier with the need to have the drug in his free form at tumour interstitium. To this aim we designed a bi-compartmental device where the two chambers are separated by a porous membrane. This device is intended to mimic mass transport at tumour interstitium where the diffusive transport is dominant. One chamber is devoted to cell seeding and the other is a drug reservoir. In this way we can evaluate drug penetration and diffusion both when in his free form and when complexed to a nanoparticle and points out the differences among these instances.

KEYWORDS Extracellular Drug Delivery, Biodegradable Nanoparticles, Nanoparticle distibution in 3D models, 3D Tumour Model

4.1 Introduction

The systemic delivery of therapeutic agents to the tumour mass is a three-step process: convective transport through blood-borne vessels to different regions of the tumour, extravasation and transport across the vessel wall and finally, diffusive transport through the interstitial space to reach the tumour cells [110] [111].

Once NPs reach the tumour mass, the factors governing and, in most cases, limiting their transport at tumour interstitium are numerous.

First of all, the viscous nature of the interstitium limits the fluid flow and diffusion of NPs from the blood towards the cells. Dense extracellular matrix, poses a barrier in the transport of NPs principally due to their large size.

Moreover, Interstitial Fluid Pressure (IFP) in normal interstitium leads to a pressure gradient exerted by the exchange of oxygen, nutrients and waste products from the capillaries through the interstitial space into the lymph nodes. It creates a slightly negative pressure (-3 to 3 mm Hg) that is needed for tissue homeostasis. In tumour cells, rapid cell proliferation and metabolism requires increased levels of oxygen and nutrients. However, the rate of blood vessel formation is not as fast as the tumour growth. This result in a significant increase of the IFP, ranging from 5 up to 100 mm Hg causing hypoxic conditions in the tumour [112]. The increased IFP pressure reduces the pressure gradient between the intra and extravascular spaces, blocking the transport of large molecules across vessel walls by convection. Since the IFP is nearly uniform throughout solid tumours, convection does not contribute significantly to molecular transport in the interstitium, and molecules movements are mainly governed by diffusion [113]. Said that, the primary mode of drug transport in the tumour mass is by diffusion because there remains no opportunity for convective transport once drugs have left the vasculature [111]. Large nanoparticles (100-nm) are suitable for the Enhanced Permeability and Retention effect (EPR) but have poor diffusion in the dense collagen matrix of the interstitial space, resulting in restrictive nanoparticle accumulation around tumour blood vessels and little penetration into the tumour parenchyma [110], while small drug molecule easily penetrate and diffuse through it since, obviously, the smaller the molecule the better the transport [24]. Moreover, NPs cannot simply enter the cells *via* diffusion. Indeed, they are internalized by endocytic processes and, after internalization, are transported in vesicles

from early endosome to late endosomes and eventually to lysosomes, while small molecule drug mainly enter cell *via* diffusion [114] [112].

In the light of these considerations, transport properties governing tumour penetration by molecules give important guidelines that can be used for the design of nanoscale therapeutics [111].

In this context, nanodevices able to deliver their cargo at the extracellular level could bridge the gap between the need of a drug transporter able to carry safely the drug to the tumour site and the advantages in terms of drug diffusion and penetration beneath tumour mass of the free drug itself.

In order to verify if extracellular drug delivery may really improve drug penetration through tumour interstium, a comparison between the distribution of free Doxorubicin (Dox) molecules and Dox molecules transported by a polymeric nanocarrier, through an *in vitro* tumour interstium model was done (see Figure 4.1).

To this aim, a device mimicking the diffusion of molecules at tumour interstitium was designed and a tridimensional (3D) and highly cell-dense biological model, mimicking the tumour mass, was settled up. Moreover, polymeric-based drug transporters were prepared.

Finally, drug distribution through the biological model was evaluated by means of confocal microscopy technique.

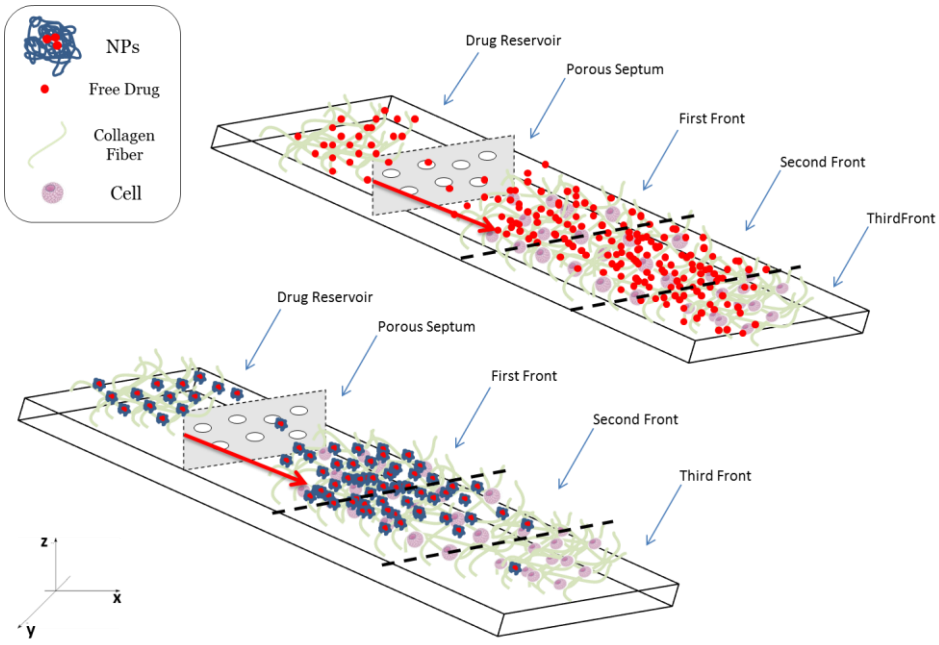

Figure 4.1: Schematic representation of the work.

4.2 Materials and Methods

4.2.1. Materials

Poly(methyl methacrylate) PMMA substrates (5 mm thickness) were purchased from Goodfellow Cambridge Ltd, (UK), Poly(dimethylsiloxane) (PDMS) prepolymer and a curing agent (Sylgard 184 elastomer kit) were purchased from Dow Corning Corporation (USA). Equimolar uncapped poly(D,L-lactide-co-glycolide) (PLGA) (Resomer RG502H, Mw 12, 000 Da) was purchased from Boehringer Ingelheim (Ingelheim, Germany). Doxorubicin hydrochloride (Dox, purity>99%) was purchased from Discovery Fine Chemicals (UK). Polyethylene glycol (PEG, Mw 1500 Da), ethylenediamine, 4-(dimethylamino) pyridine (DMAP), N,N'-Dicyclohexylcarbodiimide (DCC), dichloromethane (DCM) and Phosphate buffer saline (PBS) tablets without calcium and magnesium were purchased from Sigma-Aldrich (USA). Dialysis bags (MWCO 6000-8000 Da) were obtained from Spectrum Laboratories, Inc. (The Netherlands), while distilled and deionized water (18MΩ resistance) were from Millipore (USA).

Minimun Essential Medium (MEM), Phosphate Buffer Saline (PBS) without calcium and magnesium, L-glutamine, Trypsin, Penicillin and Streptomycin were purchased from Microgem. Collagen solution from bovine skin and Fetal Bovine Serum (FBS) were purchased from Sigma-Aldrich (USA) and Collagenase A from Roche.

4.2.2. Bi-compartmental chamber: design and implementation

A bi-compartmental device was designed to allow the simulation of drug diffusion at tumour interstitium. It is composed by two chambers separated by a porous membrane (Membrane Filters, Millipore) with a pore size of 650 nm, and by a step (2.3×8.6×0.5 mm) which avoids substance diffusion beneath the membrane itself. The larger chamber is devoted to cell seeding in collagen (6×15×5 mm), the smaller one (3×15×5 mm) acts as a drug reservoir of nanoparticles (NPs) or free drug in collagen. A 3D reconstruction of the bi-compartmental chamber is reported in Figure 4.2.

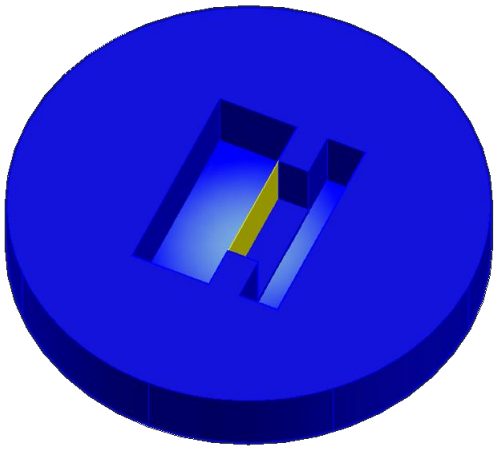

Figure 4.2: 3D reconstruction of the bi-compartmental chamber. Porous membrane is reported in yellow.

The system was implemented according to the PDMS-based soft lithography. The master was typically fabricated by sequentially micromachining PMMA layers by using micromilling machine (Minitech Machinery Corporation, USA). PDMS monomer and curing agent were mixed in a 10:1 (base: curing agent) ratio by weight for manual mixing. After that, PDMS was poured into the PMMA mould and exposed to vacuum to eliminate air bubbles for at least 30 min. Finally, to complete PDMS curing process, the replica was baked in oven at 80 °C for 45 min. Three PDMS replica were bonded to a glass coverslip with oxygen plasma to activate the surface, using a plasma chamber (Plasma prep II, SPI) and then placed in oven at 80 °C for 1 h. After membrane insertion, the system was sterilized by UV light.

4.2.3. Synthesis of copolymers and conjugates

PLGA-PEG copolymer (namely PELGA) was synthesized *via* a coupling reaction between PLGA and PEG, optimizing a previously published procedure (see *Chapter.1 Chapter.2*) [4]. Briefly, the carboxyl group of PLGA reacted with the terminal hydroxyl group of PEG. 1 eq of PLGA-NH2, 2 eq of PEG 0.4 eq DMAP and 2 eq of DCC were dissolved in 20 ml of anhydrous DCM. After the reaction (2 days, RT, inert atmosphere), the residual DCC was changed into dicyclohexylcarbodiurea (DCU) by adding 10 µL of bidistilled water. The DCM was evaporated and the mixture was dissolved in 10 ml of DMSO, filtrated and dialyzed using dialysis bags with MWCO of 6-8 kDa for 1 day against DMSO, in order to remove unreacted PEG and for 2 days against milliq water.

Pure product was recovered after lyophilization and analyzed by 1H-Nuclear Magnetic Resonance (1H-NMR) spectroscopy.

PLGA-Dox copolymer was synthesized according to a previously reported procedure [4]. Briefly, the conjugate was synthesized by a standard HBTU coupling procedure. PLGA (1 eq), HBTU (1 eq), DIEA (2 eq), and Dox (1.5 eq.) were dissolved in anhydrous DMSO. Subsequently, the copolymer was purified by removing the unreacted reagents using dialysis bags (MWCO 6000 – 8000 Da). Pure product was recovered after lyophilization and analyzed by 1H-Nuclear Magnetic Resonance (1H-NMR) spectroscopy.

Nuclear Magnetic Resonance (NMR) spectra of all products were recorded using an Agilent 600MHz (14 T) spectrometer equipped with a DD2 console and an OneNMR HX probe. PLGA-PEG and PLGA-Dox samples (1 mg) were dissolved in 600 µL of 99.9 % deuterated DMSO (Sigma Aldrich). ^{1}H 1D spectra were recorded at 300 K using 1024 scans to obtain a good signal to noise ratio. Spectra were transformed and analyzed using VNMRJ 4 software. Chemical shift scale was referenced on the solvent residual peak signal. DOSY experiments were also performed.

4.2.4. NP preparation and characterization

Blended PELGA /PLGA-Dox NPs were prepared using the nanoprecipitation method, according to a previously published procedure (see *Chapter.1*and *Chapter.2*) [4]. Briefly, 1 mg of PELGA and 1 mg of PLGA-Dox were dissolved in 500 µl of acetone and the obtained solutions mixed. Afterwards, the solution was added dropwise (6 ml/h) with a syringe pump into 12.5 ml of distilled water under magnetic stirring (600 rpm). The organic solvent was then evaporated for 3 h in continuous stirring and the obtained NPs dispersion sterilized by filtration using 0.22 µm polyethersulfone (PES) syringe filters (Millipore). Finally, NPs suspensions was ultrafiltered twice using an ultrafiltration concentrator (MWCO 10 kDa, Corning) (4°C, 5000 rpm) for 15 min. The produced nanoparticles were named PELGA-Dox.

Mean size, size distribution and ζ-potential for all types of NPs were determined by laser light scattering (ZetaSizer Nano ZS, Malvern Instruments, Malvern, UK) on a 0.1 mg/ml suspension of NPs in water (12 runs each sample). Results were averaged on at least three measurements.

NPs morphology was analysed by Cryogenic Transmission Electron Microscopy (Cryo-TEM). Cryo-TEM samples were vetrified with FEI Vitrobot Mk IV in a saturated water vapour environment. Sample volumes of 3 µL were placed on 200 mesh Quantifoil grids and the excess sample was blotted away with filter paper. Blot time and drain time were both 1 s. After blotting, the grids were plunged into liquid propane that was cooled with liquid nitrogen surrounding the propane vessel. Imaging was performed with TEM TECNAI G^2 equipment operating at 200 kV in low dose mode and acquired by Eagle 2HS camera.

4.2.5 Cell culture

The biological model was set up using, human fibrosarcoma cells (HT1080). Cells were purchased by ATCC and cultured with complete medium, composed of Eagle's minimal essential medium (EMEM) supplemented with 10 % FBS, 1 % glutamine, and 100 U/mL penicillin, 100 mg/mL streptomycin. The cells were maintained in 100 mm diameter cell culture dishes in a humidified controlled atmosphere at 37 ºC and 5 % CO_2. The medium was changed every 2-3 days.

4.2.6 Dose-response curve

To investigate cell response at different drug concentrations, 2 x 10^5 HT1080 cells were seeded on 12 well plates and incubated for 24h in a humidified atmosphere at 37 °C and 5 % CO_2 to obtain a subconfluent monolayer. Cells were then treated with cell medium alone or free Dox at a final drug concentration of 0.5, 1, 2 and 4 µg/ml. The day after treatment, cell viability was evaluated by means of Alamar Blue Assay, according to manufacturer procedure. All experiments were performed in triplicate.

4.2.7 Cell seeding in collagen

Collagen gel was prepared by diluting collagen solution with PBS 10X (8:1 volume ratio) and adjusting the pH to 7.4 adding NaOH and HCl dropwise. 40 µl of collagen solution was poured into the larger chamber and incubated at 37 °C for about 20 min, allowing the formation of a collagen basement as thick as the PDMS step that separates the

two chambers. After fibrillogenesis of the collagen basement, 2×10^5 HT1080 cells were suspended in 330 µl of 2.2 mg/ml collagen solution and poured into the chamber. The system was then incubated at 37 °C for 45 min to allow collagen fibrillogenesis and, afterwards, fresh cell culture medium was added to the gel [115] [116] [117].

For model characterization studies, cell- embedded collagen gels were stained according to the procedure reported by A*rytm et al* [118], with slightly modifications.

Briefly, cell culture medium was aspirated from the top of the collagen gel without damaging it and 4 % paraformaldehyde/5 % sucrose in PBS was added to fix the samples. 20 min after incubation at RT, the fixing solution was removed and samples were washed twice with PBS for 10 minutes at RT, while shaking. Subsequently, 0.15 M glycine in PBS was added to the gels for 10 minutes to quench the formaldehyde. After that, other two long washing steps of the gels in PBS were done and a solution of 0.5 % Triton X-100 in PBS was added to permeabilize the cells. After 10 min of incubations at RT, Triton X-100 solution was gently removed and two short washing steps of the sample were performed. At this point, actin filaments were stained using phalloidin-FITC (Merck) (λ_{ex}= 488 nm, $\Delta\lambda_{em}$= [500;530] nm) incubating the sample with a 1 % solution of Phalloidin in PBS for 30 minutes at RT. Finally cell nuclei were stained with DAPI (Merck) ($\lambda_{\mathbf{ex}}$= 700 nm, $\Delta\lambda_{em}$= [400;450] nm) incubating the sample with a 1 % solution of DAPI in PBS for 1 h at RT.

Confocal images were acquired with Leica TCS SP5 MP (Solms, Germany) equipped with a water immersion 25× objective, with a resoution of 1024x1024. Moreover, Second Harmonic Generation (SHG) signal was used to visualise unstained collagen gels (λex = 840 nm, λem = 420 ± 5 nm).

4.2.8 NPs distribution in the collagen-based tumour model

24 h after seeding, 330 µl of 2.2 mg/ml collagen solution containing PELGA-Dox NPs or free Dox at a final drug concentration of 2 µg/ml were poured into the smaller chamber at 37 °C for about 45 min for compounds distribution analyses through the 3D collagen model. Moreover, 330 µl of 2.2 mg/ml collagen solution containing cell medium alone was poured into the smaller chamber as positive control. After 3 and 24 h, all samples were imaged using a confocal and multiphoton microscope system (Leica TCS SP5 MP, Solms, Germany) with a 20x dry objective. Images were acquired using tile scan mode, with a resolution of 1024x1024 pixels. All experiments were performed in triplicate.

4.3 Results

4.3.1 Synthesis of copolymers and conjugates

^{1}H-1D NMR and DOSY spectra of PELGA and PELGA-Dox conjugates confirm the structure of all the conjugates and show that it was not found a significant amount of unreacted reagents for all the samples.

A detailed chemical characterization of the conjugates can be found in Chapter.3, paragraph "*Synthesis of copolymers and conjugates"*.

4.3.2 Nanoparticles characterization

PLGA-Dox copolymer was mixed with PELGA [53] in acetone for NPs production, according to the procedure described above. The produced NPs were characterized in terms of size, ζ-potential and morphology.

A detailed characterization of PELGA-Dox NPs can be found in Chapter.2, paragraphs *"NPs mean size, ξ-potential and stability"* and *"NPs morphological characterization"*.

4.3.3 Dose-response curve

Cell response at different Dox concentrations was investigated setting up a dose-response curve, reported in Figure 4.3. Cell viability data show a 50% decrease in cell viability 24 h after drug treatment, for a drug concentration of 2 μg/ml. At this point a plateau is reached, since increasing the drug concentration do not lead to an increase in cell death. Based on these findings, all the experiments were performed using this drug concentration.

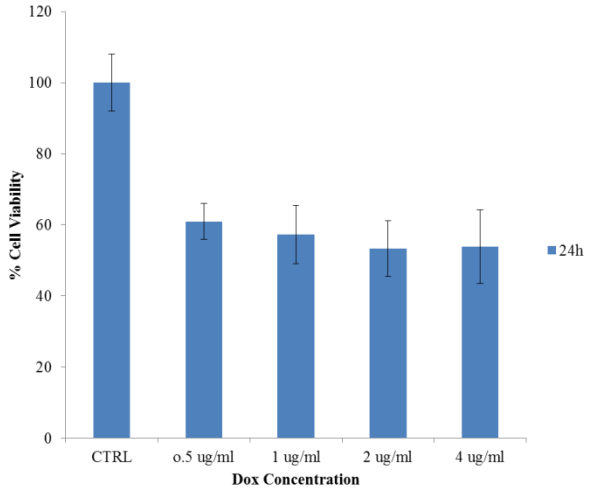

Figure 4.3: Dose response curve of HT1080 cells to free Dox.

4.3.4 3D Biological model characterization

In order to characterize the biological model and validate the homogeneity of cell seeding in collagen, cell-embedded collagen gels were stained and imaged with a confocal and multiphoton microscope. Moreover, two-photon excited fluorescence was used to induce SHG and obtain high-resolution images of unstained collagen fibrils.

Figure 4.4 A shows cell actin filaments in green and cell nuclei in blue. Cells appear in a stretched conformation which is typical when embedded in a collagen matrix. Figure 4.4 B show the SHG signal of the collagen, which proofs the presence of fibrils and confirms that collagen fibrillogenesis occurred.

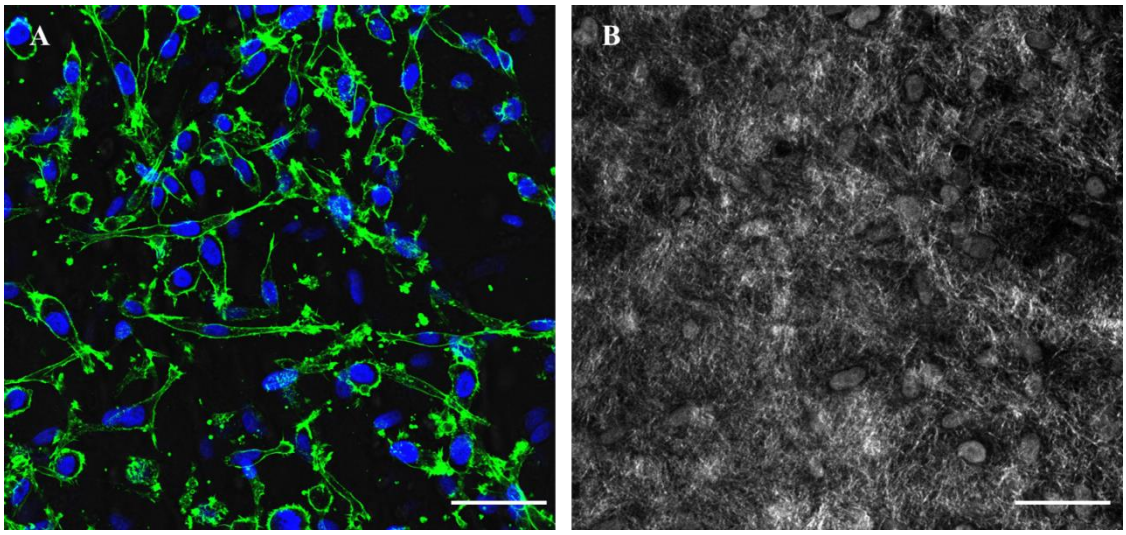

Figure 4.4: Characterization of the 3D biological model by Confocal Microscopy. Cell nuclei are stained with DAPI (blue) and actin filaments are stained with phalloidin-FITC (green) (A); SHG signal (in white) confirms the presence of collagen fibrils (B). Scale bar: 50 µm.

Finally, in Figure 4.5 is reported a 3D reconstruction of the biological model which clearly show a homogeneous distribution of the cells in the whole gel.

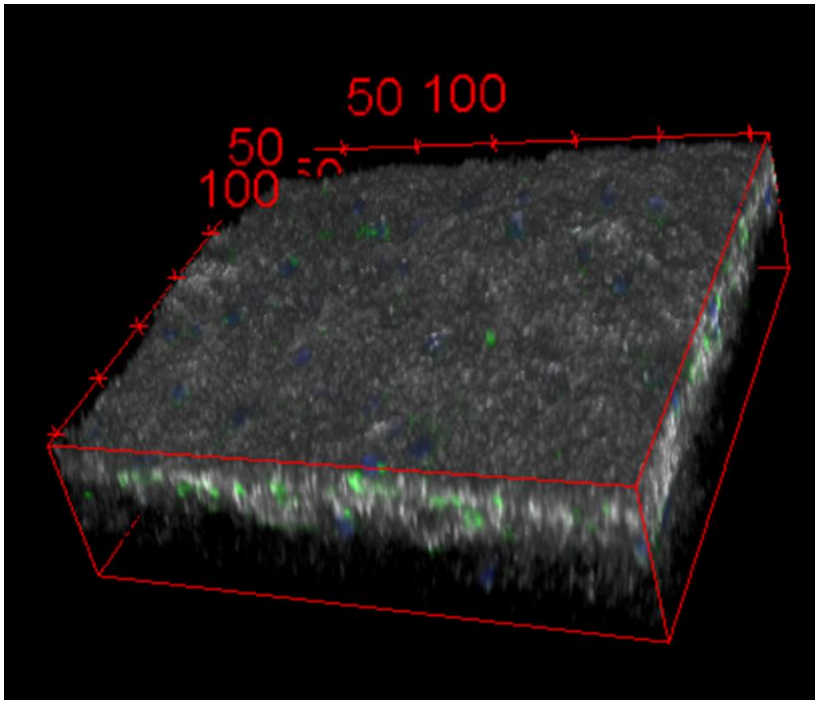

Figure 4.5: 3D reconstruction of the biological model by Confocal Microscopy. SHG signal (in white) confirms the presence of collagen fibrills. Cell nuclei are stained with DAPI (blue) and actin filaments are stained with phalloidin-FITC (green).

4.3.5 Drug distribution analyses through the 3D tumour model

In this section proof-of-principle demonstration that, when at tumour interstitium, the free drug can be easily delivered into the dense collagen matrix of a tumour if compared to a drug-nanocarrier, is given.

All samples were treated with a final Dox concentration of 2 μg/ml for 24 h, since the dose-response curve showed a relevant cytotoxic action of the drug at this concentration in this time frame.

Multiphoton microscopy images revealed a marked increase in Dox penetration into tumour model as compared with the PELGA-Dox NPs, confirming a substantial enhancement in interstitial transport associated with molecule dimension and diffusion coefficient [24]. In more detail, Figure 4.6 show Dox distribution within the 3D model after 3h of exposure to cell medium alone (A), PELGA-Dox NPs (B) and free Dox (C). We can easily notice that Dox signal in panel C is higher compared to the one reported in panel B which is, indeed, similar to the fluorescent signal coming from the control sample.

Moreover, this difference increase, increasing the incubation time till 24h, as can be seen in Figure 4.7.

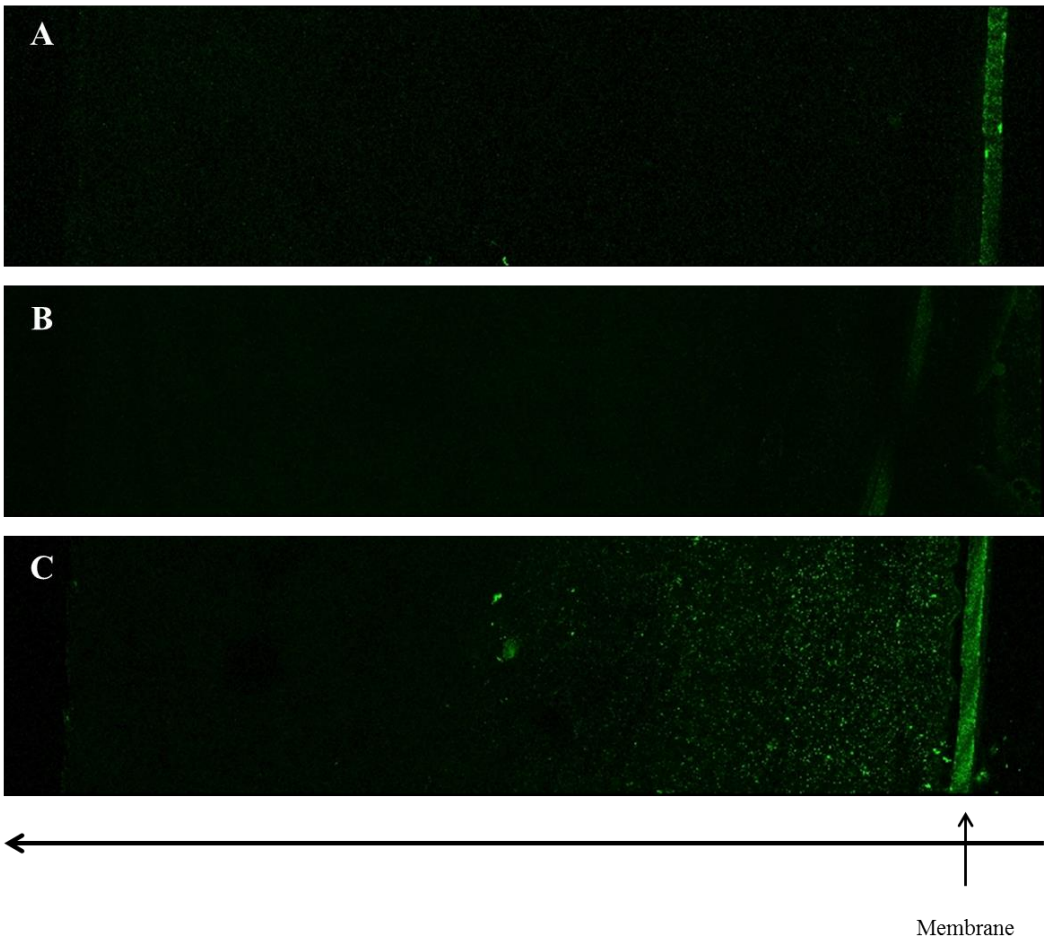

Figure 4.6: Dox distribution within the 3Dmodel after 3h of exposure to cell medium alone (A), PELGA-Dox NPs (B) and free Dox (C).

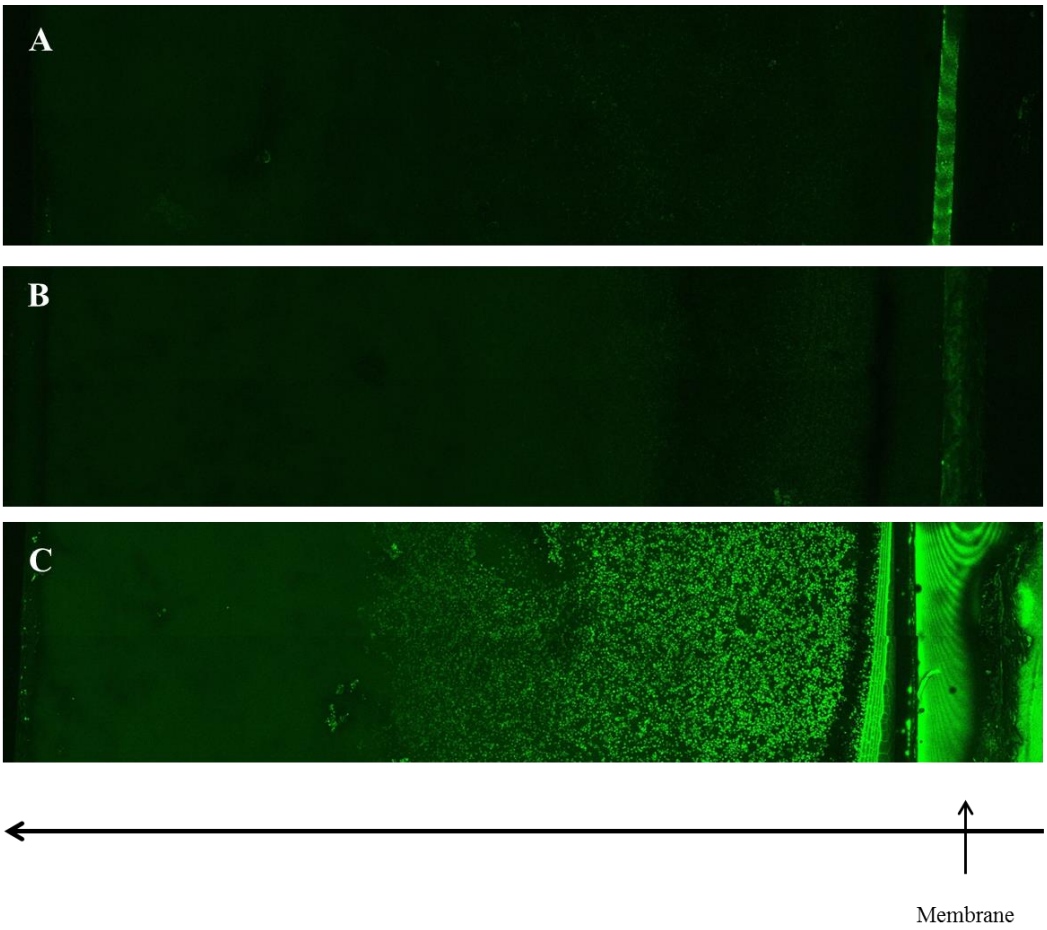

Figure 4.7: Dox distribution within the 3Dmodel after 24h of exposure to cell medium alone (A), PELGA-Dox NPs (B) and free Dox (C).

4.4 Discussions

The above presented results, even if preliminary, clearly show that a drug, in his free form can easily penetrate into tumour interstitium, where mass exchanges mainly occur *via* diffusion. This is due to the very small dimensions of the drug molecules which easily diffuse through the collagen matrix. On the other hand, NP-based drug transport is not promoted in absence of convective mass transport due to the large size of the NPs [24]. In more detail, where drug dose is equal, these consideration results in a higher tissue penetration of the free drug in the tumour mass if compared to NPs.

These data are in agreement with the work of *Wong et al.* [110]. They propose a multistage system in which 100-nm nanoparticles "shrink" to 10-nm nanoparticles after they extravasate from leaky regions of the tumour vasculature and are exposed to the tumour microenvironment. The shrunken nanoparticles can more readily diffuse throughout the tumour interstitial space thanks to this change in their size, triggered by proteases.

Indeed, *in vivo* circulation half-life and intratumoural diffusion measurements indicate that these multistage nanoparticles exhibited both the long circulation half-life necessary for the EPR effect and the deep tumour penetration required for the delivery into the tumour dense collagen matrix.

Furthermore, *Biondi et al.* [53] prepared NPs whit a size less of 100 nm and translated standard 2D cytotoxicity studies to 3D collagen systems in which an initial step gradient of the NPs was present. In their experiments, they found that these NPs elicited a cytotoxic effect which decreased increasing the distance from the drug source while free drug exerted its cytotoxic effects almost through the entire collagen volume.

4.5 Conclusions and Future Developments

The above presented preliminary results are aimed to point out that a drug, when in its free form, can easily penetrate into tumour interstitium where convective mass transport is not permitted. Otherwise, it is unquestionable the need of a carrier able to transport safely the drug at the tumour site through the vasculature (where convective transport is promoted) in a selective manner.

Since that, a point of contact between these two needs could be the extracellular drug release. Indeed, a well-designed nanocarrier, able to release its cargo in the extracellular environment, would carry safely the active agent till tumour interstitium and, only at this stage, would release its cargo, presenting the drug to the cells in his free form.

By the way, further experiments need to be performed to improve data reliability and to deeply investigate the above presented phenomena. In particular, the observation times of the drug distribution through the 3D tumour model should be increased and a quantitative evaluation of the distance covered by the drug when in its free form or when transported by the NPs, along with cytotoxicity analyses, should be performed.

Acknowledgments

The authors thank Pietro Melone for his help in synthesizing PELGA copolymer, Dr. Eliana Esposito for her support in device implementation, Dr, Fabio Formiggini for his help in confocal microscopy experimental settings and Dr. Nunzia Cummaro for helpful discussions and support.

Conclusions and Future Perspectives

The work described in this thesis intends to exploit the fascinating word of the *stimuli-responsive* drug delivery for the design of nanodevices capable to sense the endogenous micro-environmental changes in tumour tissues for cancer therapy applications.

During the last several decades, controlled drug delivery technology has advanced significantly, leading to the development of various clinical formulations improving patient compliance and convenience. Current technologies allow the delivery of drugs with desired release kinetics for extended periods of time ranging from days to years. Nevertheless, there are still areas where substantial improvements need to be done to reach the next level of clinical relevance. One such area is spatially-controlled drug delivery at tumour site in order to minimize drug-originated systemic off-site toxicity.

In the light of these considerations, in **Chapter.1** we proposed the design of MMP-2-responsive nanoparticles, based on the pro-drug approach. These systems are composed by a PLGA molecule linked to Dox through a MMP-sensitive peptide and were named PELGA-TAP NPs. As expected, *in vitro* testing of these NPs on tumour and healthy spheroids proved that Dox release only occurs upon MMP cleavage of the peptide in tumour tissues, which strongly up-regulate these enzymes. Hence, in this section the design and production of biodegradable, biocompatible and endogenous *stimuli-responsive* NPs was addressed.

Inspired by these encouraging results, in **Chapter.2** we tested PELGA-TAP NPs on a more complex *in vitro* model, *i.e.* 3D tumour and healthy microtissues, which better recapitulates tissues architecture along with its microenviroment due to the presence of a well-structured and endogenous extracellular matrix. Cytotoxicity data obtained after microtissue treatment with NPs further validate the tissue- and site-specific action of NPs and the accumulation of the drug in the extracellular space, which are crucial requirements to enhance anticancer drug activity at tumour site. Therefore, in this section a validation of NP behaviour in a more realistic tissue equivalent was addressed.

In **Chapter.3** we developed an upgrade of the *stimuli-responsive* NPs based on the layer-by-layer polymer deposition technique. The delivery system we propose are ultra-stable cross-linked polyelectrolyte nanocapsules (MMP-NCs) with an oil-core, a high drug loading capacity and a MMP-sensitive shell. *In vitro* testing of MMP-NCs, on healthy and tumour spheroids proofed that this design allows for NC shell disassembly and consequent

release of lipophilic drugs only in presence of MMP over-expression. So, also in this case, drug release only occurs in a spatially-controlled fashion upon an endogenous *stimulus* coming from the very nature of the tumour itself. In this section a viable route to address with a single elegant solution both the NC stability issue and the spatially-controlled release requirements was thus proposed.

Finally, in **Chapter.4** some of the major advantages associated with an extracellular drug delivery are highlighted. In particular, we presented preliminary results showing that if a drug reaches the tumour interstitium in its free form, then an enhancement in its diffusion and penetration through the tumour mass can be achieved. Thereby, nanocarriers capable to deliver their cargo at the extracellular level could bridge the gap between two fundamental needs: a safe delivery of the drug to the tumour site and its diffusion and penetration beneath tumour mass. Although this study paves the way for a new approach to drug delivery, it is still at its early stage and more experiments needs to be performed to validate the data.

All the approaches to the design of NPs for microenvironmentally-triggered extracellular drug release illustrated in this work of thesis fulfil both these needs. Indeed, they allow to safely carry the drug at the tumour site without harmful effects to healthy tissues, and to release the cargo in the extracellular space only in presence of a site-specific trigger signal, such as MMP-2.

Taken all together the studies we present show promising results for the possible application of microenvironmentally-triggered nanocarriers in the field of nanomedicine, thus encouraging for further *in vivo* investigation. Their translation into clinics could lead, indeed, to great benefits to patients by reducing the amount of administrated drug and its side effects.

Reference List

[1] E. Fleige, M. A. Quadir, and R. Haag, "Stimuli-responsive polymeric nanocarriers for the controlled transport of active compounds: concepts and applications," *Advanced drug delivery reviews,* vol. 64, pp. 866-884, **2012**.

[2] S. Mura, J. Nicolas, and P. Couvreur, "Stimuli-responsive nanocarriers for drug delivery," *Nature materials,* vol. 12, p. 991, **2013**.

[3] M. Duffy, "The role of proteolytic enzymes in cancer invasion and metastasis," *Clinical & experimental metastasis,* vol. 10, pp. 145-155, **1992**.

[4] M. Cantisani, D. Guarnieri, M. Biondi, V. Belli, M. Profeta, L. Raiola, *et al.*, "Biocompatible nanoparticles sensing the matrix metallo-proteinase 2 for the on-demand release of anticancer drugs in 3D tumor spheroids," *Colloids and Surfaces B: Biointerfaces,* vol. 135, pp. 707-716, **2015**.

[5] V. Brancato, A. Garziano, F. Gioiella, F. Urciuolo, G. Imparato, V. Panzetta, *et al.*, "3D is not enough: building up a cell instructive microenvironment for tumoral stroma microtissues," *Acta biomaterialia,* vol. 47, pp. 1-13, **2017**.

[6] V. Brancato, F. Gioiella, M. Profeta, G. Imparato, D. Guarnieri, F. Urciuolo, *et al.*, "3D tumor microtissues as an in vitro testing platform for microenvironmentally-triggered drug delivery systems," *Acta Biomaterialia,* **2017**.

[7] R. Vecchione, G. Iaccarino, P. Bianchini, R. Marotta, F. D'autilia, V. Quagliariello, *et al.*, "Ultrastable liquid–liquid interface as viable route for controlled deposition of biodegradable polymer nanocapsules," *Small,* vol. 12, pp. 3005-3013, **2016**.

[8] S. A. Brooks, H. J. Lomax-Browne, T. M. Carter, C. E. Kinch, and D. M. Hall, "Molecular interactions in cancer cell metastasis," *Acta histochemica,* vol. 112, pp. 3-25, **2010**.

[9] H. J. L.-B. Susan A. Brooks, Tracey M. Carter, Chole E. Kinch, Debbie M.S. Hall, "Molecular interactions in cancer cell metastasis," *Acta histochemics, Elsevier,* **2008**.

[10] Y. H. Bae, R. J. Mrsny, and K. Park, *Cancer targeted drug delivery*: Springer, **2013**.

[11] W. F. Michael Kohler, *Nanotechnology. An introduction to nanostructuring tecniques*: WILEY-VCH, **2004**.

[12] M. A. Q. Emanule Fleige, Rainer Haag, "Stimuli- responsive polymeric nanocarriers for the controlled transport of active compounds: concepts and applications," *Advanced Drug Delivery Reviews, Elsevier,* **2012**.

[13] R. P. Feynman, "There's plenty of room at the bottom," *Engineering and science,* vol. 23, pp. 22-36, **1960**.

[14] H. Hillaireau and P. Couvreur, "Nanocarriers' entry into the cell: relevance to drug delivery," *Cellular and Molecular Life Sciences,* vol. 66, pp. 2873-2896, **2009**.

[15] K. P. You Han Bae, "Targeted drug delivery to tumors: Myths, reality and possibility," *Journal of Controlled Release, Elsevier,* **2011**.

[16] G. P. Francesco M. Veronese, "PEGylation, successful approach to drug delivery," *Drug Discovery Today,* **2005**.

[17] J. M. H. Francesco M. Veronese, "Introduction and overview of peptide and protein pegylation," *Advanced Drug Delivery Reviews, Elsevier,* **2002**.

[18] H. Schellekens, W. E. Hennink, and V. Brinks, "The immunogenicity of polyethylene glycol: facts and fiction," *Pharmaceutical research,* vol. 30, pp. 1729-1734, **2013**.

[19] L. Zhu and V. P. Torchilin, "Stimulus-responsive nanopreparations for tumor targeting," *Integrative Biology*, vol. 5, pp. 96-107, **2013**.

[20] J. Lee, M. J. Cuddihy, and N. A. Kotov, "Three-dimensional cell culture matrices: state of the art," *Tissue Engineering Part B: Reviews*, vol. 14, pp. 61-86, **2008**.

[21] J. Friedrich, C. Seidel, R. Ebner, and L. A. Kunz-Schughart, "Spheroid-based drug screen: considerations and practical approach," *Nature protocols*, vol. 4, pp. 309-324, **2009**.

[22] G. Imparato, F. Urciuolo, and P. Netti, "In vitro three-dimensional models in cancer research: a review," *International Materials Reviews*, vol. 60, pp. 297-311, **2015**.

[23] S. Balivada, R. S. Rachakatla, H. Wang, T. N. Samarakoon, R. K. Dani, M. Pyle, *et al.*, "A/C magnetic hyperthermia of melanoma mediated by iron (0)/iron oxide core/shell magnetic nanoparticles: a mouse study," *BMC cancer*, vol. 10, p. 119, **2010**.

[24] R. K. Jain and T. Stylianopoulos, "Delivering nanomedicine to solid tumors," *Nature reviews Clinical oncology*, vol. 7, pp. 653-664, **2010**.

[25] C. Lee and I. Tannock, "Inhibition of endosomal sequestration of basic anticancer drugs: influence on cytotoxicity and tissue penetration," *British journal of cancer*, vol. 94, p. 863, **2006**.

[26] D. Peer, J. M. Karp, S. Hong, O. C. Farokhzad, R. Margalit, and R. Langer, "Nanocarriers as an emerging platform for cancer therapy," *Nature nanotechnology*, vol. 2, pp. 751-760, **2007**.

[27] R. Injac and B. Strukelj, "Recent advances in protection against doxorubicin-induced toxicity," *Technology in cancer research & treatment*, vol. 7, pp. 497-516, **2008**.

[28] R. Injac, M. Boskovic, M. Perse, E. Koprivec-Furlan, A. Cerar, A. Djordjevic, *et al.*, "Acute doxorubicin nephrotoxicity in rats with malignant neoplasm can be successfully treated with fullerenol C60 (OH) 24 via suppression of oxidative stress," *Pharmacological Reports*, vol. 60, p. 742, **2008**.

[29] R. Injac, M. Perse, M. Cerne, N. Potocnik, N. Radic, B. Govedarica, *et al.*, "Protective effects of fullerenol C 60 (OH) 24 against doxorubicin-induced cardiotoxicity and hepatotoxicity in rats with colorectal cancer," *Biomaterials*, vol. 30, pp. 1184-1196, **2009**.

[30] M. M. Gottesman, T. Fojo, and S. E. Bates, "Multidrug resistance in cancer: role of ATP-dependent transporters," *Nature reviews. Cancer*, vol. 2, p. 48, **2002**.

[31] K. S. Smalley, N. K. Haass, P. A. Brafford, M. Lioni, K. T. Flaherty, and M. Herlyn, "Multiple signaling pathways must be targeted to overcome drug resistance in cell lines derived from melanoma metastases," *Molecular cancer therapeutics*, vol. 5, pp. 1136-1144, **2006**.

[32] M. M. Gottesman, "Mechanisms of cancer drug resistance," *Annual review of medicine*, vol. 53, pp. 615-627, **2002**.

[33] M. Ferrari, "Cancer nanotechnology: opportunities and challenges," *Nature reviews. Cancer*, vol. 5, p. 161, **2005**.

[34] H. Maeda, J. Wu, T. Sawa, Y. Matsumura, and K. Hori, "Tumor vascular permeability and the EPR effect in macromolecular therapeutics: a review," *Journal of controlled release*, vol. 65, pp. 271-284, **2000**.

[35] V. P. Chauhan, T. Stylianopoulos, Y. Boucher, and R. K. Jain, "Delivery of molecular and nanoscale medicine to tumors: transport barriers and strategies," *Annual review of chemical and biomolecular engineering*, vol. 2, pp. 281-298, **2011**.

[36] Y. H. Bae and K. Park, "Targeted drug delivery to tumors: myths, reality and possibility," *Journal of Controlled Release,* vol. 153, p. 198, **2011**.

[37] H. Wang, J. D. Owens, J. H. Shih, M.-C. Li, R. F. Bonner, and J. F. Mushinski, "Histological staining methods preparatory to laser capture microdissection significantly affect the integrity of the cellular RNA," *BMC genomics,* vol. 7, p. 97, **2006**.

[38] A. N. Gordon, J. T. Fleagle, D. Guthrie, D. E. Parkin, M. E. Gore, and A. J. Lacave, "Recurrent epithelial ovarian carcinoma: a randomized phase III study of pegylated liposomal doxorubicin versus topotecan," *Journal of clinical oncology,* vol. 19, pp. 3312-3322, **2001**.

[39] M. O'brien, N. Wigler, M. Inbar, R. Rosso, E. Grischke, A. Santoro, *et al.*, "Reduced cardiotoxicity and comparable efficacy in a phase III trial of pegylated liposomal doxorubicin HCl (CAELYX™/Doxil®) versus conventional doxorubicin for first-line treatment of metastatic breast cancer," *Annals of oncology,* vol. 15, pp. 440-449, **2004**.

[40] D. W. Northfelt, B. J. Dezube, J. A. Thommes, B. J. Miller, M. A. Fischl, A. Friedman-Kien, *et al.*, "Pegylated-liposomal doxorubicin versus doxorubicin, bleomycin, and vincristine in the treatment of AIDS-related Kaposi's sarcoma: results of a randomized phase III clinical trial," *Journal of clinical oncology,* vol. 16, pp. 2445-2451, **1998**.

[41] F. Meng, Y. Zhong, R. Cheng, C. Deng, and Z. Zhong, "pH-sensitive polymeric nanoparticles for tumor-targeting doxorubicin delivery: concept and recent advances," *Nanomedicine,* vol. 9, pp. 487-499, **2014**.

[42] L. Zhu and R. I. Mahato, "Targeted delivery of siRNA to hepatocytes and hepatic stellate cells by bioconjugation," *Bioconjugate chemistry,* vol. 21, pp. 2119-2127, **2010**.

[43] L. Zhu, P. Kate, and V. P. Torchilin, "Matrix metalloprotease 2-responsive multifunctional liposomal nanocarrier for enhanced tumor targeting," *ACS nano,* vol. 6, pp. 3491-3498, **2012**.

[44] S. Matsumura, I. Aoki, T. Saga, and K. Shiba, "A tumor-environment-responsive nanocarrier that evolves its surface properties upon sensing matrix metalloproteinase-2 and initiates agglomeration to enhance T 2 relaxivity for magnetic resonance imaging," *Molecular pharmaceutics,* vol. 8, pp. 1970-1974, **2011**.

[45] M. Egeblad and Z. Werb, "New functions for the matrix metalloproteinases in cancer progression," *Nature reviews. Cancer,* vol. 2, p. 161, **2002**.

[46] G. Klein, E. Vellenga, M. Fraaije, W. Kamps, and E. De Bont, "The possible role of matrix metalloproteinase (MMP)-2 and MMP-9 in cancer, eg acute leukemia," *Critical reviews in oncology/hematology,* vol. 50, pp. 87-100, **2004**.

[47] L. Holle, W. Song, E. Holle, Y. Wei, T. Wagner, and X. Yu, "A matrix metalloproteinase 2 cleavable melittin/avidin conjugate specifically targets tumor cells in vitro and in vivo," *International journal of oncology,* vol. 22, pp. 93-98, **2003**.

[48] D. Guarnieri, M. Biondi, H. Yu, V. Belli, A. P. Falanga, M. Cantisani, *et al.*, "Tumor-activated prodrug (TAP)-conjugated nanoparticles with cleavable domains for safe doxorubicin delivery," *Biotechnology and bioengineering,* vol. 112, pp. 601-611, **2015**.

[49] S. J. Lee, B. R. Han, S. Y. Park, D. K. Han, and S. C. Kim, "Sol–gel transition behavior of biodegradable three-arm and four-arm star-shaped PLGA–PEG block

copolymer aqueous solution," *Journal of Polymer Science Part A: Polymer Chemistry,* vol. 44, pp. 888-899, **2006**.

[50] E. Lengyel, R. Gum, J. Juarez, G. Clayman, M. Seiki, H. Sato, *et al.*, "Induction of Mr 92,000 type IV collagenase expression in a squamous cell carcinoma cell line by fibroblasts," *Cancer research,* vol. 55, pp. 963-967, **1995**.

[51] B. Schmalfeldt, D. Prechtel, K. Härting, K. Späthe, S. Rutke, E. Konik, *et al.*, "Increased expression of matrix metalloproteinases (MMP)-2, MMP-9, and the urokinase-type plasminogen activator is associated with progression from benign to advanced ovarian cancer," *Clinical Cancer Research,* vol. 7, pp. 2396-2404, **2001**.

[52] D. Guarnieri, M. A. Malvindi, V. Belli, P. P. Pompa, and P. Netti, "Effect of silica nanoparticles with variable size and surface functionalization on human endothelial cell viability and angiogenic activity," *Journal of nanoparticle research,* vol. 16, p. 2229, **2014**.

[53] M. Biondi, D. Guarnieri, H. Yu, V. Belli, and P. A. Netti, "Sub-100 nm biodegradable nanoparticles: in vitro release features and toxicity testing in 2D and 3D cell cultures," *Nanotechnology,* vol. 24, p. 045101, **2013**.

[54] F. Danhier, B. Vroman, N. Lecouturier, N. Crokart, V. Pourcelle, H. Freichels, *et al.*, "Targeting of tumor endothelium by RGD-grafted PLGA-nanoparticles loaded with paclitaxel," *Journal of Controlled Release,* vol. 140, pp. 166-173, **2009**.

[55] J. Li, L. Feng, L. Fan, Y. Zha, L. Guo, Q. Zhang, *et al.*, "Targeting the brain with PEG–PLGA nanoparticles modified with phage-displayed peptides," *Biomaterials,* vol. 32, pp. 4943-4950, **2011**.

[56] K. Kupai, G. Szucs, S. Cseh, I. Hajdu, C. Csonka, T. Csont, *et al.*, "Matrix metalloproteinase activity assays: Importance of zymography," *J Pharmacol Toxicol Methods,* vol. 61, pp. 205-9, Mar-Apr **2010**.

[57] J. M. Santos, S. P. Camoes, E. Filipe, M. Cipriano, R. N. Barcia, M. Filipe, *et al.*, "Three-dimensional spheroid cell culture of umbilical cord tissue-derived mesenchymal stromal cells leads to enhanced paracrine induction of wound healing," *Stem Cell Res Ther,* vol. 6, p. 90, May 09 **2015**.

[58] M. Toth, A. Sohail, and R. Fridman, "Assessment of gelatinases (MMP-2 and MMP-9) by gelatin zymography," *Metastasis Research Protocols,* pp. 121-135, **2012**.

[59] L. Mayol, A. Borzacchiello, V. Guarino, C. Serri, M. Biondi, and L. Ambrosio, "Design of electrospayed non-spherical poly (L-lactide-co-glicolide) microdevices for sustained drug delivery," *Journal of Materials Science: Materials in Medicine,* vol. 25, pp. 383-390, **2014**.

[60] R. Z. Lin and H. Y. Chang, "Recent advances in three-dimensional multicellular spheroid culture for biomedical research," *Biotechnology journal,* vol. 3, pp. 1172-1184, **2008**.

[61] R. Li, W. Wu, Q. Liu, P. Wu, L. Xie, Z. Zhu, *et al.*, "Intelligently targeted drug delivery and enhanced antitumor effect by gelatinase-responsive nanoparticles," *PLoS One,* vol. 8, p. e69643, **2013**.

[62] Y. Mi, J. Wolfram, C. Mu, X. Liu, E. Blanco, H. Shen, *et al.*, "Enzyme-responsive multistage vector for drug delivery to tumor tissue," *Pharmacological research,* vol. 113, pp. 92-99, **2016**.

[63] P. Cirri and P. Chiarugi, "Cancer-associated-fibroblasts and tumour cells: a diabolic liaison driving cancer progression," *Cancer and Metastasis Reviews,* vol. 31, pp. 195-208, **2012**.

[64] Y. Mao, E. T. Keller, D. H. Garfield, K. Shen, and J. Wang, "Stromal cells in tumor microenvironment and breast cancer," *Cancer and Metastasis Reviews,* vol. 32, pp. 303-315, **2013**.

[65] R. M. Bremnes, T. Dønnem, S. Al-Saad, K. Al-Shibli, S. Andersen, R. Sirera, *et al.*, "The role of tumor stroma in cancer progression and prognosis: emphasis on carcinoma-associated fibroblasts and non-small cell lung cancer," *Journal of thoracic oncology,* vol. 6, pp. 209-217, **2011**.

[66] I. M. Adjei and S. Blanka, "Modulation of the tumor microenvironment for cancer treatment: a biomaterials approach," *Journal of functional biomaterials,* vol. 6, pp. 81-103, **2015**.

[67] R. K. Jain, "Normalizing tumor microenvironment to treat cancer: bench to bedside to biomarkers," *Journal of Clinical Oncology,* vol. 31, pp. 2205-2218, **2013**.

[68] O. Trédan, C. M. Galmarini, K. Patel, and I. F. Tannock, "Drug resistance and the solid tumor microenvironment," *Journal of the National Cancer Institute,* vol. 99, pp. 1441-1454, **2007**.

[69] P. Longati, X. Jia, J. Eimer, A. Wagman, M.-R. Witt, S. Rehnmark, *et al.*, "3D pancreatic carcinoma spheroids induce a matrix-rich, chemoresistant phenotype offering a better model for drug testing," *BMC cancer,* vol. 13, p. 95, **2013**.

[70] M. F. Estrada, S. P. Rebelo, E. J. Davies, M. T. Pinto, H. Pereira, V. E. Santo, *et al.*, "Modelling the tumour microenvironment in long-term microencapsulated 3D co-cultures recapitulates phenotypic features of disease progression," *Biomaterials,* vol. 78, pp. 50-61, **2016**.

[71] A. Nyga, M. Loizidou, M. Emberton, and U. Cheema, "A novel tissue engineered three-dimensional in vitro colorectal cancer model," *Acta biomaterialia,* vol. 9, pp. 7917-7926, **2013**.

[72] C.-T. Tsao, F. M. Kievit, K. Wang, A. E. Erickson, R. G. Ellenbogen, and M. Zhang, "Chitosan-based thermoreversible hydrogel as an in vitro tumor microenvironment for testing breast cancer therapies," *Molecular pharmaceutics,* vol. 11, pp. 2134-2142, **2014**.

[73] E. Burdett, F. K. Kasper, A. G. Mikos, and J. A. Ludwig, "Engineering tumors: a tissue engineering perspective in cancer biology," *Tissue Engineering Part B: Reviews,* vol. 16, pp. 351-359, **2010**.

[74] G. Imparato, C. Casale, S. Scamardella, F. Urciuolo, M. Bimonte, F. Apone, *et al.*, "A novel engineered dermis for in vitro photodamage research," *Journal of tissue engineering and regenerative medicine,* vol. 11, pp. 2276-2285, **2017**.

[75] F. Gioiella, F. Urciuolo, G. Imparato, V. Brancato, and P. A. Netti, "An Engineered Breast Cancer Model on a Chip to Replicate ECM-Activation In Vitro during Tumor Progression," *Advanced healthcare materials,* vol. 5, pp. 3074-3084, **2016**.

[76] C. Palmiero, G. Imparato, F. Urciuolo, and P. Netti, "Engineered dermal equivalent tissue in vitro by assembly of microtissue precursors," *Acta biomaterialia,* vol. 6, pp. 2548-2553, **2010**.

[77] G. Imparato, F. Urciuolo, C. Casale, and P. A. Netti, "The role of microscaffold properties in controlling the collagen assembly in 3D dermis equivalent using modular tissue engineering," *Biomaterials,* vol. 34, pp. 7851-7861, **2013**.

[78] W. Hu, H. Li, L. Fu, C. Wang, and S. Gou, "Characterization of collagen fibers by means of texture analysis of second harmonic generation images using orientation-dependent gray level co-occurrence matrix method," *Journal of biomedical optics,* vol. 17, p. 026007, **2012**.

[79] X. Guo, A. E. Hutcheon, S. A. Melotti, J. D. Zieske, V. Trinkaus-Randall, and J. W. Ruberti, "Morphologic characterization of organized extracellular matrix

deposition by ascorbic acid–stimulated human corneal fibroblasts," *Investigative ophthalmology & visual science,* vol. 48, pp. 4050-4060, **2007**.

[80] F. Danhier, O. Feron, and V. Préat, "To exploit the tumor microenvironment: passive and active tumor targeting of nanocarriers for anti-cancer drug delivery," *Journal of Controlled Release,* vol. 148, pp. 135-146, **2010**.

[81] K.-D. Wehrstedt, P.-A. Wandrey, and D. Heitkamp, "Explosive properties of 1-hydroxybenzotriazoles," *Journal of hazardous materials,* vol. 126, pp. 1-7, **2005**.

[82] R. Subirós-Funosas, R. Prohens, R. Barbas, A. El-Faham, and F. Albericio, "Oxyma: An Efficient Additive for Peptide Synthesis to Replace the Benzotriazole-Based HOBt and HOAt with a Lower Risk of Explosion [1]," *Chemistry-a European Journal,* vol. 15, pp. 9394-9403, **2009**.

[83] S. H. Jang, M. G. Wientjes, D. Lu, and J. L.-S. Au, "Drug delivery and transport to solid tumors," *Pharmaceutical research,* vol. 20, pp. 1337-1350, **2003**.

[84] T. T. Goodman, C. P. Ng, and S. H. Pun, "3-D tissue culture systems for the evaluation and optimization of nanoparticle-based drug carriers," *Bioconjugate chemistry,* vol. 19, pp. 1951-1959, **2008**.

[85] M. Kanapathipillai, A. Brock, and D. E. Ingber, "Nanoparticle targeting of anti-cancer drugs that alter intracellular signaling or influence the tumor microenvironment," *Advanced drug delivery reviews,* vol. 79, pp. 107-118, **2014**.

[86] J. Adur, H. F. Carvalho, C. L. Cesar, and V. H. Casco, "Nonlinear optical microscopy signal processing strategies in cancer," *Cancer informatics,* vol. 13, p. 67, **2014**.

[87] J. Adur, V. B. Pelegati, A. A. de Thomaz, M. O. Baratti, L. A. Andrade, H. F. Carvalho, *et al.*, "Second harmonic generation microscopy as a powerful diagnostic imaging modality for human ovarian cancer," *Journal of biophotonics,* vol. 7, pp. 37-48, **2014**.

[88] V. P. Torchilin, "Targeted pharmaceutical nanocarriers for cancer therapy and imaging," *Aaps j,* vol. 9, pp. E128-47, May 11 **2007**.

[89] S. Mura, J. Nicolas, and P. Couvreur, "Stimuli-responsive nanocarriers for drug delivery," *Nat Mater,* vol. 12, pp. 991-1003, Nov **2013**.

[90] J. You, R. Zhang, C. Xiong, M. Zhong, M. Melancon, S. Gupta, *et al.*, "Effective photothermal chemotherapy using doxorubicin-loaded gold nanospheres that target EphB4 receptors in tumors," *Cancer Res,* vol. 72, pp. 4777-86, Sep 15 **2012**.

[91] K. J. Chen, H. F. Liang, H. L. Chen, Y. Wang, P. Y. Cheng, H. L. Liu, *et al.*, "A thermoresponsive bubble-generating liposomal system for triggering localized extracellular drug delivery," *ACS Nano,* vol. 7, pp. 438-46, Jan 22 **2013**.

[92] L. Zhang, T. Wang, L. Yang, C. Liu, C. Wang, H. Liu, *et al.*, "General route to multifunctional uniform yolk/mesoporous silica shell nanocapsules: a platform for simultaneous cancer-targeted imaging and magnetically guided drug delivery," *Chemistry,* vol. 18, pp. 12512-21, Sep 24 **2012**.

[93] A. Schroeder, R. Honen, K. Turjeman, A. Gabizon, J. Kost, and Y. Barenholz, "Ultrasound triggered release of cisplatin from liposomes in murine tumors," *J Control Release,* vol. 137, pp. 63-8, Jul 01 **2009**.

[94] Z. Deng, Z. Zhen, X. Hu, S. Wu, Z. Xu, and P. K. Chu, "Hollow chitosan-silica nanospheres as pH-sensitive targeted delivery carriers in breast cancer therapy," *Biomaterials,* vol. 32, pp. 4976-86, Jul **2011**.

[95] A. N. Koo, H. J. Lee, S. E. Kim, J. H. Chang, C. Park, C. Kim, *et al.*, "Disulfide-cross-linked PEG-poly(amino acid)s copolymer micelles for glutathione-mediated intracellular drug delivery," *Chem Commun (Camb),* pp. 6570-2, Dec 28 **2008**.

[96] E. Gullotti, J. Park, and Y. Yeo, "Polydopamine-based surface modification for the development of peritumorally activatable nanoparticles," *Pharm Res,* vol. 30, pp. 1956-67, Aug **2013**.

[97] M. Egeblad and Z. Werb, "New functions for the matrix metalloproteinases in cancer progression," *Nat Rev Cancer,* vol. 2, pp. 161-174, 03//print **2002**.

[98] G. Klein, E. Vellenga, M. W. Fraaije, W. A. Kamps, and E. S. de Bont, "The possible role of matrix metalloproteinase (MMP)-2 and MMP-9 in cancer, e.g. acute leukemia," *Crit Rev Oncol Hematol,* vol. 50, pp. 87-100, May **2004**.

[99] L. Zhu, P. Kate, and V. P. Torchilin, "Matrix metalloprotease 2-responsive multifunctional liposomal nanocarrier for enhanced tumor targeting," *ACS Nano,* vol. 6, pp. 3491-8, Apr 24 **2012**.

[100] T. Terada, M. Iwai, S. Kawakami, F. Yamashita, and M. Hashida, "Novel PEG-matrix metalloproteinase-2 cleavable peptide-lipid containing galactosylated liposomes for hepatocellular carcinoma-selective targeting," *J Control Release,* vol. 111, pp. 333-42, Apr 10 **2006**.

[101] V. Calcagno, R. Vecchione, A. Sagliano, A. Carella, D. Guarnieri, V. Belli, *et al.*, "Biostability enhancement of oil core - polysaccharide multilayer shell via photoinitiator free thiol-ene 'click' reaction," *Colloids Surf B Biointerfaces,* vol. 142, pp. 281-9, Jun 01 **2016**.

[102] M. T. Basel, T. B. Shrestha, D. L. Troyer, and S. H. Bossmann, "Protease-sensitive, polymer-caged liposomes: a method for making highly targeted liposomes using triggered release," *ACS Nano,* vol. 5, pp. 2162-75, Mar 22 **2011**.

[103] G. Decher, "Fuzzy Nanoassemblies: Toward Layered Polymeric Multicomposites," *Science,* vol. 277, pp. 1232-1237, **1997**.

[104] V. Calcagno, R. Vecchione, A. Sagliano, A. Carella, D. Guarnieri, V. Belli, *et al.*, "Biostability enhancement of oil core—polysaccharide multilayer shell via photoinitiator free thiol-ene 'click'reaction," *Colloids and Surfaces B: Biointerfaces,* vol. 142, pp. 281-289, **2016**.

[105] J. M. Kelm, N. E. Timmins, C. J. Brown, M. Fussenegger, and L. K. Nielsen, "Method for generation of homogeneous multicellular tumor spheroids applicable to a wide variety of cell types," *Biotechnology and bioengineering,* vol. 83, pp. 173-180, **2003**.

[106] S. Shaheen, M. Ahmed, F. Lorenzi, and A. S. Nateri, "Spheroid-formation (Colonosphere) assay for in vitro assessment and expansion of stem cells in colon cancer," *Stem Cell Reviews and Reports,* vol. 12, pp. 492-499, **2016**.

[107] R. A. McCloy, S. Rogers, C. E. Caldon, T. Lorca, A. Castro, and A. Burgess, "Partial inhibition of Cdk1 in G2 phase overrides the SAC and decouples mitotic events," *Cell Cycle,* vol. 13, pp. 1400-1412, **2014**.

[108] Y.-C. Tung, A. Y. Hsiao, S. G. Allen, Y.-s. Torisawa, M. Ho, and S. Takayama, "High-throughput 3D spheroid culture and drug testing using a 384 hanging drop array," *Analyst,* vol. 136, pp. 473-478, **2011**.

[109] S. Bolte and F. Cordelieres, "A guided tour into subcellular colocalization analysis in light microscopy," *Journal of microscopy,* vol. 224, pp. 213-232, **2006**.

[110] C. Wong, T. Stylianopoulos, J. Cui, J. Martin, V. P. Chauhan, W. Jiang, *et al.*, "Multistage nanoparticle delivery system for deep penetration into tumor tissue," *Proceedings of the National Academy of Sciences,* vol. 108, pp. 2426-2431, **2011**.

[111] C. L. Waite and C. M. Roth, "Nanoscale drug delivery systems for enhanced drug penetration into solid tumors: current progress and opportunities," *Critical Reviews™ in Biomedical Engineering,* vol. 40, **2012**.

[112] S. Barua and S. Mitragotri, "Challenges associated with penetration of nanoparticles across cell and tissue barriers: a review of current status and future prospects," *Nano today*, vol. 9, pp. 223-243, **2014**.

[113] B. S. Kuszyk, F. M. Corl, F. N. Franano, D. A. Bluemke, L. V. Hofmann, B. J. Fortman, *et al.*, "Tumor transport physiology: implications for imaging and imaging-guided therapy," *American Journal of Roentgenology*, vol. 177, pp. 747-753, **2001**.

[114] X. Dai, Z. Yue, M. E. Eccleston, J. Swartling, N. K. Slater, and C. F. Kaminski, "Fluorescence intensity and lifetime imaging of free and micellar-encapsulated doxorubicin in living cells," *Nanomedicine: Nanotechnology, Biology and Medicine*, vol. 4, pp. 49-56, **2008**.

[115] M. A. Wozniak and P. J. Keely, "Use of three-dimensional collagen gels to study mechanotransduction in T47D breast epithelial cells," *Biological procedures online*, vol. 7, pp. 144-161, **2005**.

[116] H. Asaga, S. Kikuchi, and K. Yoshizato, "Collagen gel contraction by fibroblasts requires cellular fibronectin but not plasma fibronectin," *Experimental cell research*, vol. 193, pp. 167-174, **1991**.

[117] T. Nishiyama, N. Tominaga, K. Nakajima, and T. Hayashi, "Quantitative evaluation of the factors affecting the process of fibroblast-mediated collagen gel contraction by separating the process into three phases," *Collagen and related research*, vol. 8, pp. 259-273, **1988**.

[118] V. V. Artym and K. Matsumoto, "Imaging cells in three-dimensional collagen matrix," *Current protocols in cell biology*, pp. 10.18. 1-10.18. 20, **2010**.

Ringraziamenti

Ringrazio il Professor Paolo A. Netti per avermi dato la possibilità di lavorare ad un progetto scientifico molto interessante e stimolante. Vorrei inoltre ringraziare il Dott. Raffele Vecchione e la Dott. Giulia Iaccarino per aver creduto in me e per tutta la fiducia che mi hanno dato.

Il ringraziamento più grande va sicuramente ai miei genitori senza i quali di certo non sarei qui a scrivere queste pagine. Grazie per tutti i sacrifici quotidiani, piccoli e grandi, che avete fatto e che continuate a fare per me. Ringrazio poi mio fratello Stefano per la spensieratezza e l' allegria con cui riesce sempre contagiarmi.

Mille grazie ai mie nonni per aver sempre creduto in me e perché non c'è niente di più bello che vedermi attraverso i loro occhi.

Un ringraziamento davvero speciale deve andare a tutti i ragazzi del laboratorio IIT-CRIB con i quali ho condiviso questa esperienza affascinante ma non sempre facile. Grazie per aver alleggerito le mie giornate di laboratorio e per avermi sempre strappato un sorriso.

Grazie mille a Raffaella e Pasquale per la loro infinita disponibilità, a Valentina B. per il suo sostegno e supporto e un grazie speciale a Fabio e Valentina per essere stati il mio punto di riferimento scientifico e umano in questi anni, per tutto il conforto e l'affetto che hanno saputo darmi e per tutto quello che mi hanno insegnato.

Ringrazio Martina per esserci ancora dopo tutti questi anni. Sei una amica preziosa.

Grazie a Francesca e Chiara per il loro contagioso ottimismo e per tutto l'affetto che sanno dimostrarmi.

Grazie a Vito e Rosamaria per tutta la pazienza che hanno con me, e grazie a Carmine perché non smette mai di ricordarmi chi sono e dove voglio andare quando mi perdo e ho bisogno di ritrovare la strada.

Infine ringrazio chi aveva il dovere morale e scientifico di sostenermi in questo percorso e non lo ha fatto, perchè mi ha fatto capire che potevo farcela anche da sola.

Grazie di cuore.